INVESTIGATION OF THE SPACE-DEPENDENT ZERO-POWER REACTOR SOURCE TRANSFER FUNCTION

A THESIS

Presented to

The Faculty of the Graduate Division

by

Robert Joe Johnson

In Partial Fulfillment

of the Requirements for the Degree

Doctor of Philosophy

in the School of Nuclear Engineering

Georgia Institute of Technology

September, 1966

In presenting the dissertation as a partial fulfillment of the requirements for an advanced degree from the Georgia Institute of Technology, I agree that the Library of the Institute shall make it available for inspection and circulation in accordance with its regulations governing materials of this type. I agree that permission to copy from, or to publish from, this dissertation may be granted by the professor under whose direction it was written, or, in his absence, by the Dean of the Graduate Division when such copying or publication is solely for scholarly purposes and does not involve potential financial gain. It is understood that any copying from, or publication of, this dissertation which involves potential financial gain will not be allowed without written permission.

3/17/65
b

INVESTIGATION OF THE SPACE-DEPENDENT ZERO-POWER REACTOR SOURCE TRANSFER FUNCTION

Approved:

Date approved by Chairman: 9-9-66

ACKNOWLEDGMENTS

Many individuals have contributed their special talents and encouragement toward the completion of this research. In particular, I wish to thank Dr. Charles E. Cohn of the Argonne National Laboratory, my thesis consultant, who provided the basic analytical idea and many hours of technical assistance. Dr. David W. Martin, my thesis advisor, has been a continuous source of support over an extended period of time. Dr. J. D. Clement and Dr. Marvin B. Sledd served on my reading committee and contributed many helpful suggestions during the drafting of the manuscript. Dr. C. J. Roberts has unselfishly given his time as well as the support of the School of Nuclear Engineering. The use of EXTERMINATOR was suggested by Dr. W. B. Harrison, whose interest and assistance have been greatly appreciated.

I am especially indebted to my good friends, Dr. W. W. Graham, III and Mr. T. T. Robin, whose spontaneous interest and expressions of confidence have been invaluable. Dr. R. N. Macdonald worked closely with me and contributed to many stimulating technical discussions. Dr. J. L. Carmon and his staff of the University of Georgia Computing Center were generous in providing computer time. Special thanks are extended to Mr. Ben Segal and Mr. Gene Volk of Atomic Power Development Associates, Inc., who helped expedite the acquisition of CRAM and whose personal efforts made it operational in a minimum length of time. Mr. Tom Fowler of the Oak Ridge National Laboratory offered invaluable assistance by

modifying EXTERMINATOR for specific application to this thesis. The persistence of Mr. Robert E. Meek was responsible for getting the experimental electronics to function properly under adverse conditions, and Mr. J. W. Biddy willingly cooperated on the many machining modifications necessary in the design of the pile oscillator. The author gratefully acknowledges the assistance given by Mr. R. S. Kirkland, Mr. F. C. Apple, and the GTRR operators, Mr. G. G. Crowder, Mr. D. R. Harrell, Mr. L. D. McDowell, and Mr. J. T. Moon. They were most understanding when my demands were many and confusing. Appreciation is extended to the Health Physics Staff for their helpful cooperation during the experimental phase of the work. Dr. Don H. Roy of the Babcock and Wilcox Company, Atomic Energy Division, generously gave his time to personally study the problem which resulted in his recommendation of CRAM. He also provided services to generate the two-group coefficients necessary for the numerical analysis. I also wish to thank Miss Martha Shoemaker and Mr. Pete Matrangos of the Georgia Tech Photo Lab, whose excellent work on the figures was vital to the thesis. Sincere appreciation is extended to Mrs. Lydia Fisher for the difficult task involved in typing this manuscript.

Financial support for this research was provided by a Ford Foundation Fellowship, a National Aeronautics and Space Administration Fellowship and a National Science Foundation Graduate Traineeship.

To my parents, I express my deep appreciation for their unfaltering confidence and encouragement during several years of graduate study. Finally, I wish to thank my wife, Peg, and our son, David, whose love and inspiration have made this work meaningful.

TABLE OF CONTENTS

TABLE OF CONTENTS (Concluded)

LIST OF TABLES

LIST OF ILLUSTRATIONS

LIST OF ILLUSTRATIONS (Continued)

LIST OF ILLUSTRATIONS (Continued)

LIST OF ILLUSTRATIONS (Continued)

LIST OF ILLUSTRATIONS (Concluded)

SUMMARY

A numerical method was developed by which statics techniques could be used to compute the space-dependent zero-power reactor source transfer function in the multigroup, multidimensional, diffusion theory approximation. Considering only small periodic disturbances, the flux was resolved into a steady and a fluctuating component. The steady component of the flux satisfied the static neutron balance equations. The time-dependent neutron balance equations, including an external source, were satisfied by the fluctuating parts alone. With the assumption that the external source (driving function) was sinusoidal, it was represented as the product of a complex amplitude dependent upon position only and an exponential term with argument $i\omega t$ Since the equations were linear, the flux response could also be represented in like manner. With these representations for the external source and flux response, the original time-dependent equations transformed into a set of complex equations dependent upon space and frequency but independent of time. Equating the real and imaginary parts of the equations yielded coupled, inhomogeneous, differential equations (two for each energy group). With the proper identifications, these equations were then solved by well-known statics techniques for the real and imaginary components, ϕ^R and ϕ^I, of the complex amplitudes of the fluxes. The space-dependent gain and phase angle as a function of frequency were computed for each energy group j from the following expressions:

$$G_j(\bar{x}, \omega) = \left(\phi_j^R(\bar{x}, \omega)^2 + \phi_j^I(\bar{x}, \omega)^2 \right)^{\frac{1}{2}}$$

$$\theta_j(\bar{x}, \omega) = \arctan \frac{\phi_j^I(\bar{x}, \omega)}{\phi_j^R(\bar{x}, \omega)}$$

Since small changes in the configuration of a reactor (i.e., varying absorption) can be treated as external sources, pile oscillator experiments are ideal for furnishing experimental results to be compared with the results of an analysis of this type. A pile oscillator experiment performed on the NORA reactor, with the oscillator located on the core center line, provided experimental results which were compared with the values from one-dimensional calculations. Results of the calculations closely reproduced the reported experimental results for gain and phase shift.

A similar experiment was performed on the Georgia Tech Research Reactor. The pile oscillator was located off the core center line. A fission detector measured the response of the reactor at selected locations, thereby providing the experimental data showing the space-dependent response of the neutron flux. In order to simulate this experimental situation, a two-dimensional mathematical model describing the core midplane was used. The results of the numerical analysis (assuming two energy groups) were compared with the experimental values. Qualitative agreement existed between the experimental values and the computed values for the gain and phase shift.

CHAPTER I

INTRODUCTION

Background

As the demand for larger power reactors increases, there is also greater emphasis on techniques of solving problems associated with the stability analysis both in the design phase and in the exploratory or experimental operation.[1] It is essential to be able to predict whether or not the various thermal, hydrodynamic, and nuclear processes will combine to form a stable system. In addition, subsequent to construction of a reactor, the instrumentation and controls should provide at all foreseeable operating conditions the information and interpretation that would permit the detection of an approach to an unstable condition prior to its actual occurrence.

The summarizing remarks of a recent article on "Space-Dependent Reactor Kinetics" by Kasten[2] are quoted below.

> Results of recent space-time reactor kinetics calculations indicate that, in general, spatial effects are significant and cannot be neglected in studying reactor behavior or in determining reactor parameters. Under certain circumstances the space-independent kinetics may give useful information, but these conditions are at present poorly defined. It is not clear what influence spatial effects have on the general safety and stability criteria developed using the space-independent model; much work still remains to be done in this area.

The success to be achieved in predicting the stability properties

of a system rests in recognizing the significant mechanisms involved and in construction of a mathematical model which accounts for those characteristics of the physical system which are decisive in describing its behavior to the degree of completeness necessary for the purpose in mind.[3] Consideration of the reactor kinetics poses considerable problems. Classically, the zero-power "point" reactor kinetics model is used as the basis for many investigations. Extensions of this model have dealt with linear feedback effects, nonlinear feedback effects, and spatial effects. Attempts to describe power-reactor feedback which is inherently nonlinear have received considerable attention in the past.[4] At present, the development of nonlinear methods suitable for practical use in power-reactor analysis has been prevented due to the mathematical difficulty of handling nonlinear feedback.[5] For many applications, linearization of the feedback equations has provided an adequate solution.[6] Emphasis on nonlinear dynamics analysis is currently being replaced by a greater emphasis on space-time analysis. A partial explanation for this is the increased awareness of space-time problems present in the large, modern power reactors.

Kerlin's review[5] of the status of space-time analysis includes a discussion of the adiabatic method,[7] or the instantaneous-tilt method,[8] the nodal analysis method,[8,9,10] the modal analysis method,[8,11,12,13,14] and the flux synthesis approach,[15,16] all of which have been used to solve reactor kinetics problems in which space and time response of the neutron flux are not separable. His conclusion is that the relative merits of the various methods cannot be assessed at present due to insufficient experience in dealing with practical problems. This is partly because most

space-time work has considered only one space dimension and no feedback. Recently, however, Poncelet[17] has developed a method for calculating the space-dependent reactor transfer function applicable to multienergy, multidimensional, multiregion problems which includes arbitrary feedback mechanisms. At present his capability for solving the derived equations is restricted to one dimension. Thus, regardless of the approach to be taken, the necessary direction for further work in this field is to develop models along with techniques of solution for two- and three-dimensional cases with the inclusion of feedback terms.

Purpose of This Research

The purpose of the research to be described in this thesis was to investigate space-dependent effects present in the zero-power reactor source transfer function. The experimental aspect of this investigation entailed the design and construction of a pile oscillator using the cadmium shading principle so that a known disturbance could be imposed upon the reactor at a given location. A fission detector was used to measure the response of the neutron flux within the reactor at selected locations to provide experimental evidence of the space effects. Analytically, the investigation established a numerical method by which the space-dependent effects in the zero-power reactor source transfer function could be predicted using either a one- or two-dimensional model.

Application

In 1966, large power reactors, 1100 megawatts electric, are being investigated. Increased awareness of their space-time problems requires new methods suitable for practical engineering use in the design and

analysis of such complex systems. It is hoped that the results of this investigation may be used in the development of future analytical models which incorporate the necessary feedback terms required for realistic simulation of the space-time behavior of large power reactors.

CHAPTER II

INSTRUMENTATION AND EQUIPMENT

The Georgia Tech Research Reactor

The experimental phase of the research reported here was performed on the Georgia Tech Research Reactor (hereafter referred to as GTRR). The fuel used in this heterogeneous, heavy-water moderated and cooled reactor consists of highly enriched (greater than 93 percent U-235) plates of an aluminum-uranium alloy which are aluminum clad.[18] Figure 1 is a cutaway view of a typical fuel element. Each plate is approximately 2.8 inches wide and 0.06 inch thick and has an active fuel region 23.5 inches long.

The reactor core configuration consists of fuel elements standing vertically in the plenum of the core tank and arranged on a six-inch triangular pitch. Thus, a typical ten element core (minimum loading for criticality) has an approximate radius of ten inches and a fully loaded core with 19 elements has an approximate radius of 13.5 inches, with a core height of 23.5 inches in each case. The fuel is centrally located in a six-foot diameter aluminum reactor vessel which contains the heavy water. This provides a radial D_2O reflector approximately two feet thick. A nominal water height of 76.5 inches within the core tank provides a bottom D_2O reflector thickness of 24 inches and a top reflector thickness of 29 inches.[19]

The interior of the actual aluminum reactor vessel prior to fuel element loading is shown in Figure 2. This photograph provides a view of

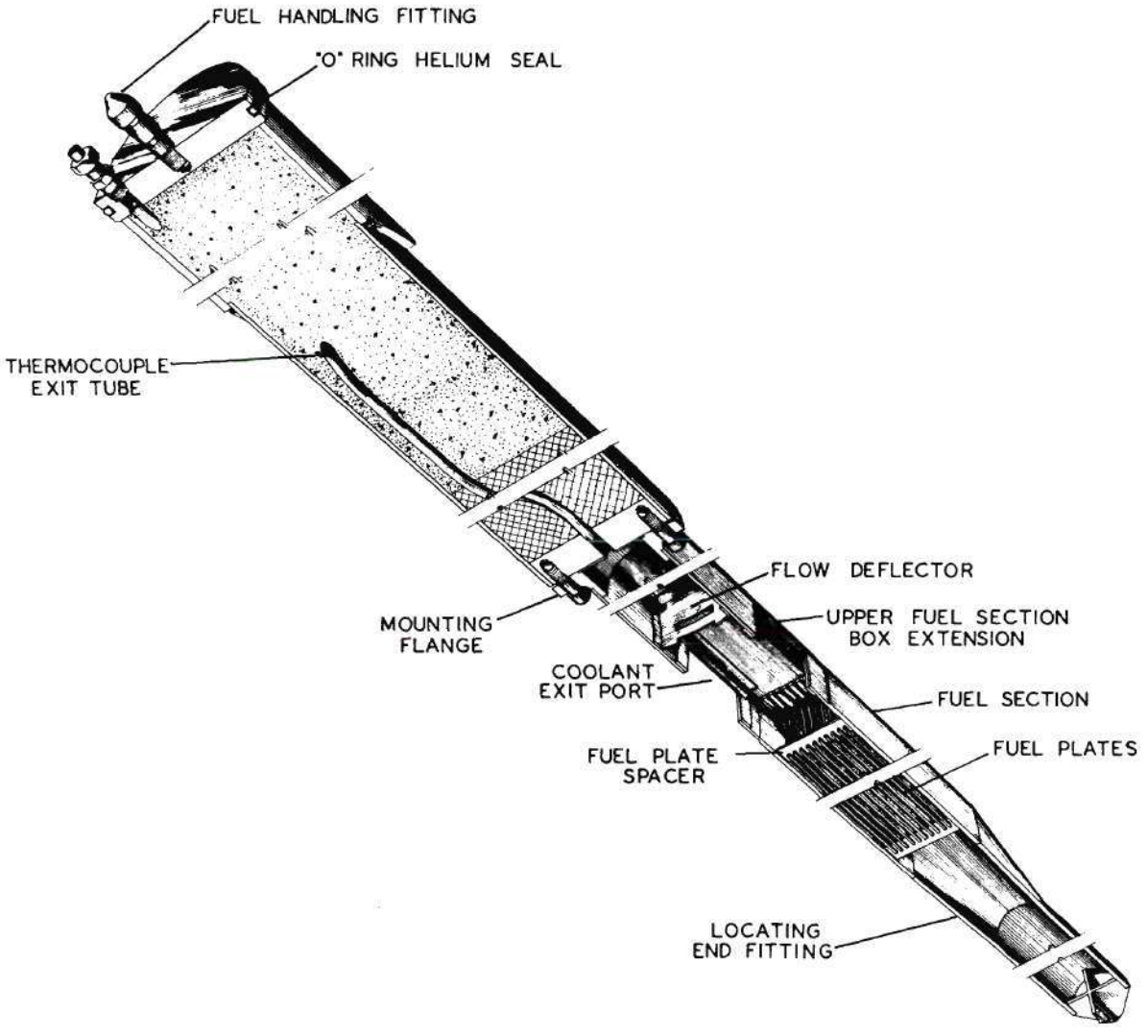

Figure 1. Georgia Tech Research Reactor -- Fuel Element Cutaway View

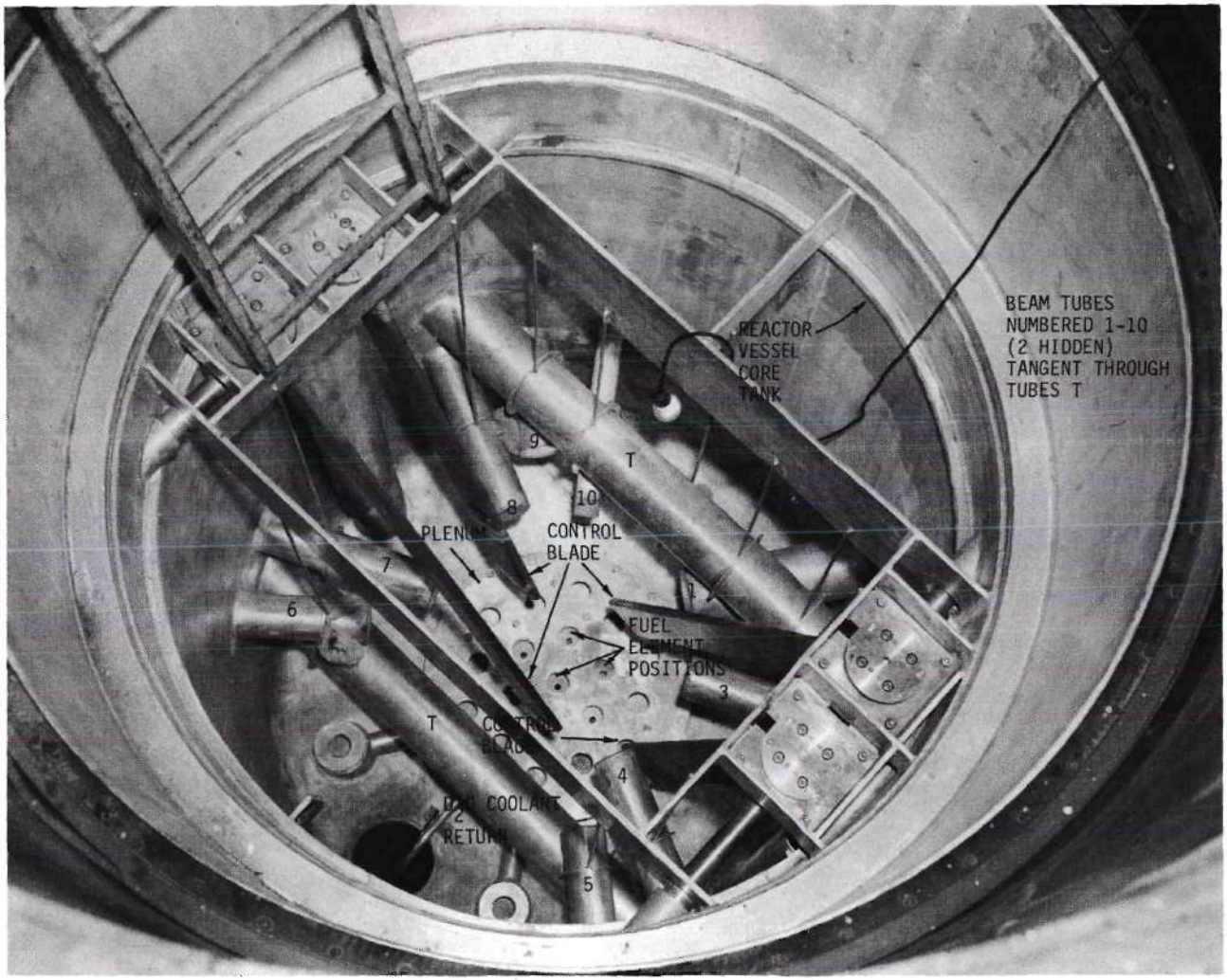

Figure 2. Interior of Georgia Tech Research Reactor Vessel Before Fuel Element Loading

the beam-tube arrangement around the fuel element positions. These positions are indicated by the holes located in the plenum. The four semaphore control blades are also visible. Figure 3, a horizontal section of the GTRR, illustrates the fuel element positions within the D_2O reflector. A two-foot thick graphite reflector cup surrounds the core tank. A concrete biological shield completely encloses the reflector system. The configuration of the horizontal beam tubes, H-1 through H-10, which are all centered on the core mid-plane, is also shown in Figure 3. Within the beam tubes, the placements of the pile oscillator, designated P, and of the detector locations for this experiment, designated 1-6, are also illustrated. To indicate the interrelationship of the radial beam ports, reflector regions, fuel elements and control blades, a cutaway perspective view of the reactor is provided in Figure 4.

Pile Oscillator

To compare the results of the theoretical calculations with experimental values, it was necessary to provide for a periodically varying source within the reactor. Under the assumption that small changes in the configuration of the reactor, e.g., varying absorption, produce the same kinetic behavior in the reactor as a varying external source, a pile oscillator was selected. Initial consideration was given to placing the oscillator within the active core region. Due to inherent design difficulties and safety problems, this approach was discarded. Final design specifications were based primarily upon the experimental objectives and also upon future use of the pile oscillator; i.e., flexibility and convenience to the user were paramount considerations. Flexibility of the

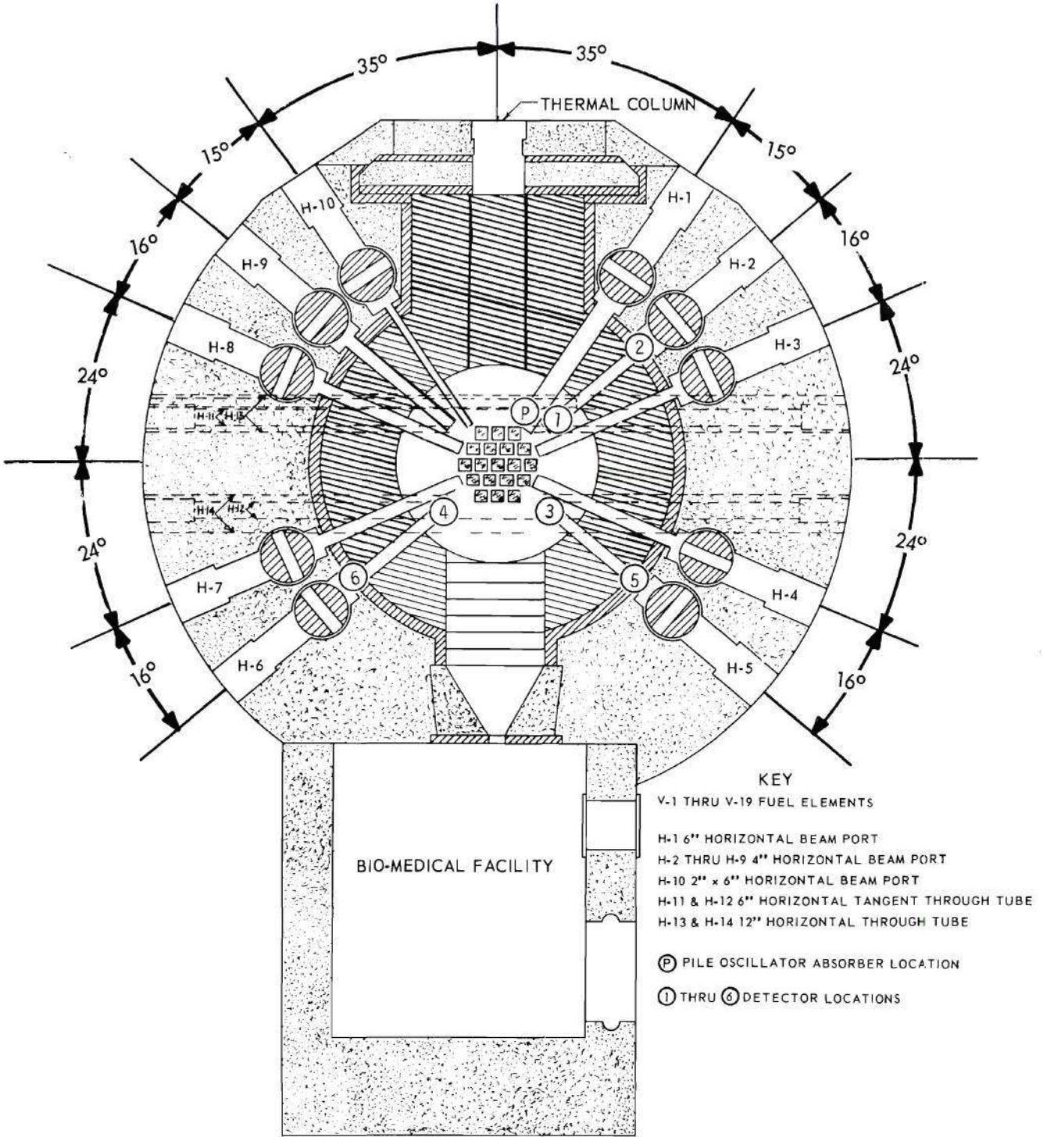

Figure 3. Horizontal Section of GTRR at Core-Midplane.

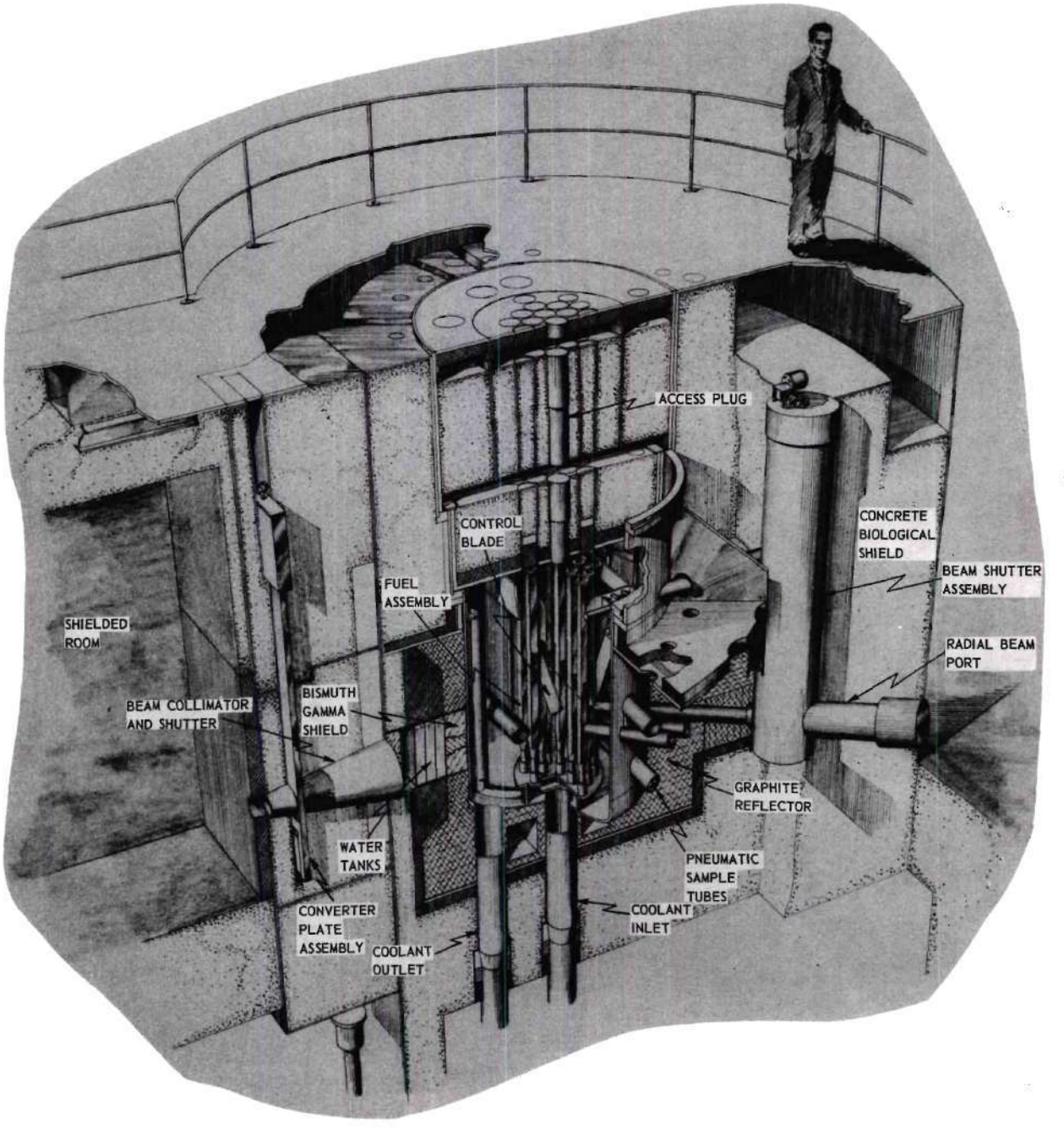

Figure 4. Cutaway View of Georgia Tech Research Reactor

design implied the ability to vary the size, shape, and location of the cadmium leaves. In addition, the design to be described permits the future use of a higher speed motor to increase the frequency range.

The basic design of the pile oscillator used the cadmium shading principle. Cadmium sheets (leaves), which are at least 20 mils thick, absorb practically all thermal neutrons impinging on the sheet. Thus, if two cadmium sheets were juxtaposed (one shadowing the other and vice versa) in the reactor, the same amount of absorption would occur as if only one sheet had been present. In other words, the amount of absorption is proportional to the exposed surface area and not to the volume. Therefore, to approximate an oscillating source in the neutron population, it is only necessary to vary the amount of surface area of cadmium exposed to thermal neutrons, thus varying the number of neutron absorptions. To implement this technique, two rectangular leaves of 20-mil cadmium sheet, 10-1/2 inches long and of such width as to subtend an angle of 90° around the circumference, were mounted on a hollow cylindrical stator (Figure 5). Likewise, two leaves of cadmium ten inches long, each also subtending an angle of 90°, were mounted on a hollow cylindrical rotor. In the rotor position where its leaves coincide with the stator leaves, the "shadowed" leaves absorb almost no additional neutrons and, therefore, the cadmium area of the stator determines the amount of absorption; as the rotor turns and its leaves are exposed, the absorption increases by a differential amount determined by the area of the rotor leaves. The leaves on the rotor provided two source cycles for each revolution of the drive shaft. This design facilitated dynamic balance of the rotor and provided a maximum source frequency that was twice the maximum

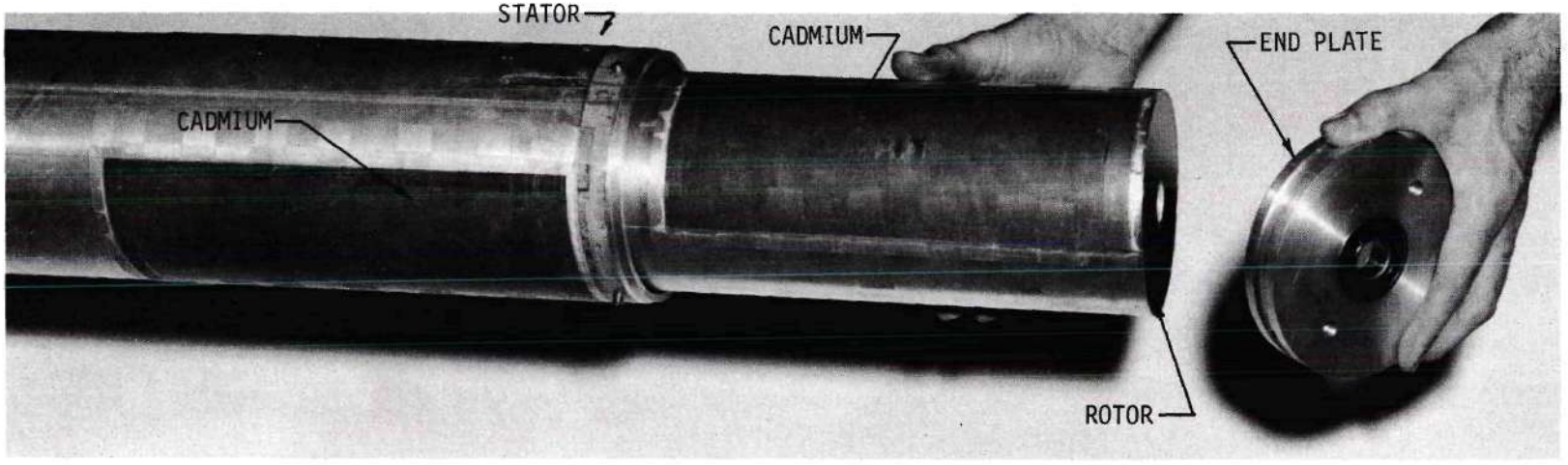

Figure 5. Large Rotor Inside Large Stator Showing Ball Bearings Mounted in the End Plate

shaft frequency. At the maximum shaft speed of 20.6 revolutions per second, the vibration in the assembly produced displacements of 1/4 inch at the tip of the stator. Allowance for this phenomenon was made in the selection of the final stator sizes (3-1/2 inch and 5-1/2 inch diameter); all the available beam tubes have an inside diameter of either four or six inches.

The oscillator, as shown in Figure 6, was housed in a three-inch diameter aluminum pipe, 47 inches long, welded to a 3/8-inch aluminum plate. The plate was fastened to the hollow beam-tube shield plug by four 1/2-inch Allen head screws. For higher reactor power experiments in the future, the plug can be filled with a shielding material. A threaded joint in the pipe permitted use of either of the two rotor and stator sets shown in Figure 7. For this research, it was necessary to use the larger stator (5-1/2 inch diameter) and its corresponding rotor so that a reasonable response could be obtained on the opposite side of the core from the pile oscillator. This restricted the location of the oscillator to beam tube H-1. For future experimentation, a 3-1/2 inch diameter stator was also fabricated, allowing use of beam tubes H-2 through H-9.

A one-inch diameter hollow aluminum shaft passes through the beam-tube shield plug down the entire length of the aluminum pipe and is secured in a set of ball bearings mounted at the tip of the stator section (Figure 5). The rotor section, which is a special spool-like design secured to the shaft, turns inside the stator section. The rotors are 4-3/4 inches O.D. and 2-29/32 inches O.D., to be used with the 5-1/2 inch O.D. and 3-1/2 inch O.D. stators, respectively. Additional ball bearing supports for the shaft are located in the small end of the beam-tube

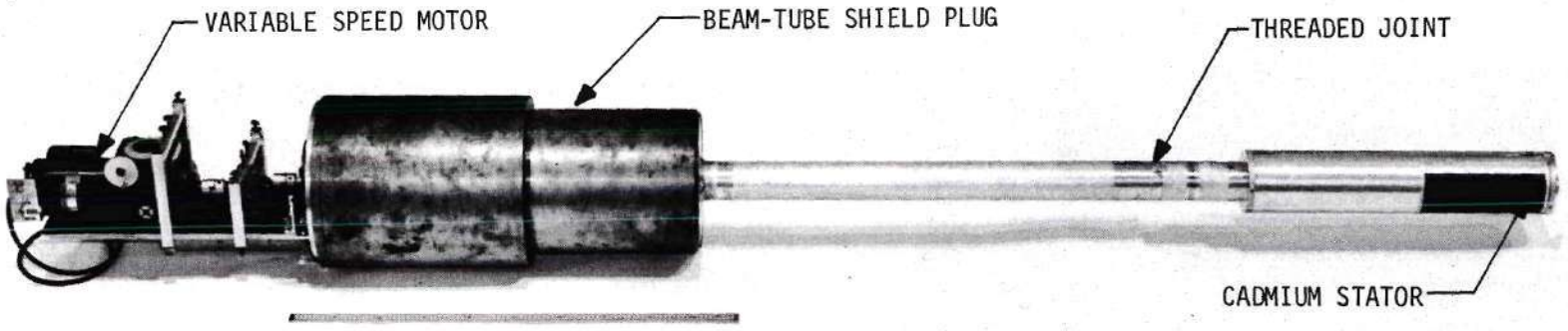

Figure 6. GTRR Pile Oscillator

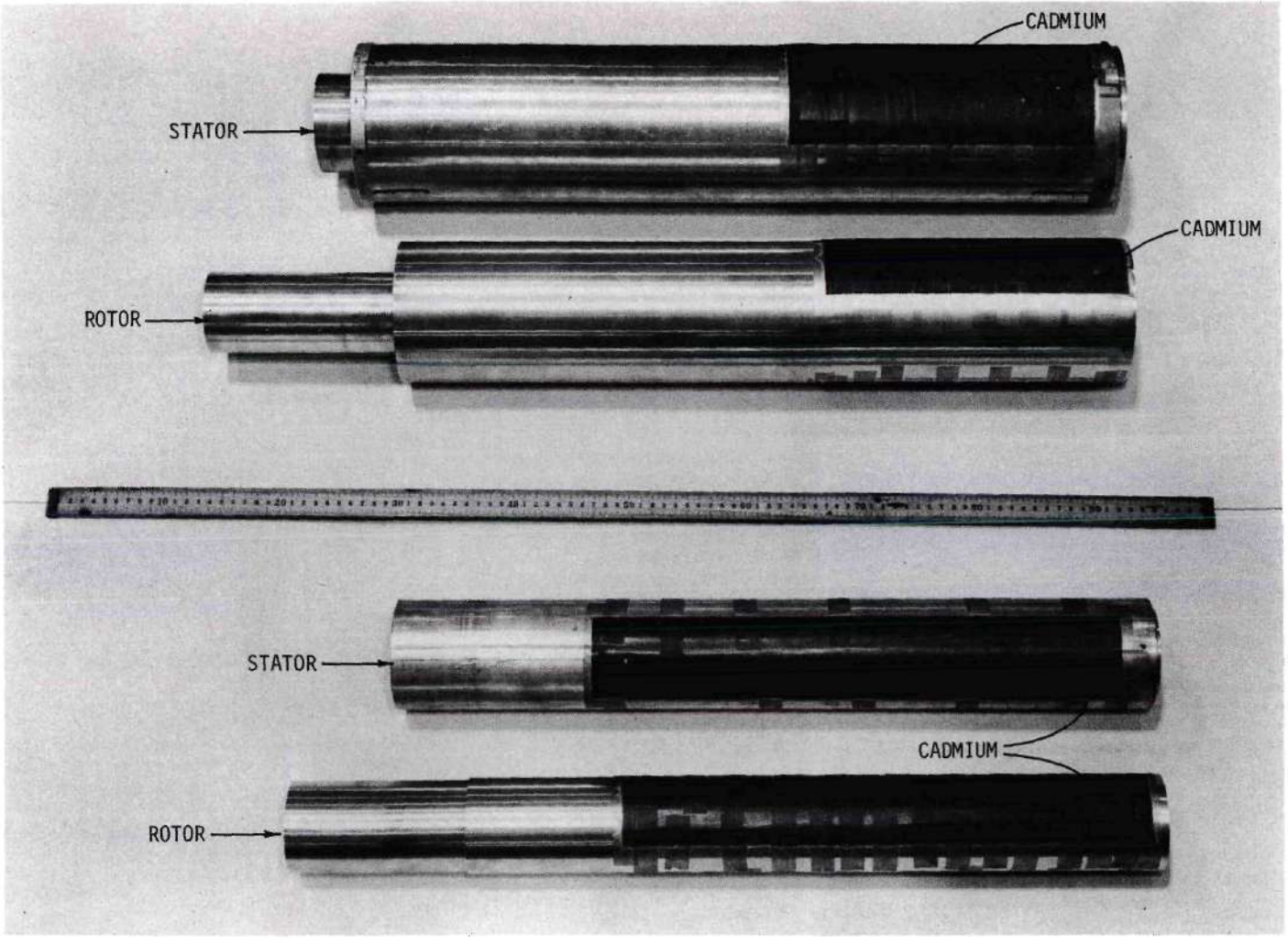

Figure 7. Alternate Rotor and Stator Sets for the Pile Oscillator

shield plug and in the 3-1/2 inch pipe before the threaded joint.

A Graham No. N-29-M Variable Speed Motor was connected to the aluminum drive shaft through flexible couplings. Intermediate gear reduction boxes were used to permit a range of shaft speeds from less than 0.05 revolution per second to 20.6 revolutions per second. The motor and gear reduction boxes were mounted on a 1/2-inch aluminum plate which was bolted to the front of the beam-tube shield plug, as shown in Figure 8. The aluminum frames with wing screws, used to fasten the assembly to the plate, facilitated interchange of the gear reduction boxes.

A flywheel was mounted on the drive shaft to reduce speed variations and to minimize effects of the shaft imbalance caused by the cadmium leaves. A cam (shown in Figure 8) was mounted on the circumference of the flywheel. A set of automotive breaker points was separated by the cam once for each revolution of the drive shaft, producing a reference pulse to synchronize the data collection and storage circuitry with the rotor.

Detection and Data Recording System

Fission Chamber System

The fission chamber used as the neutron flux detector, designated as Reactor Controls, Inc. Series RC-26-2451A-1T, and its associated electronics, have been described in detail by Graham.[20] Figure 9 shows a cross section diagram of the fission chamber. Using the detector in a high neutron flux made it necessary to shield the preamplifier as much as possible. Figure 10 shows the preamplifier and a 19-1/2 inch long, 3-3/4 inch diameter aluminum shield plug through which the fission chamber extends.

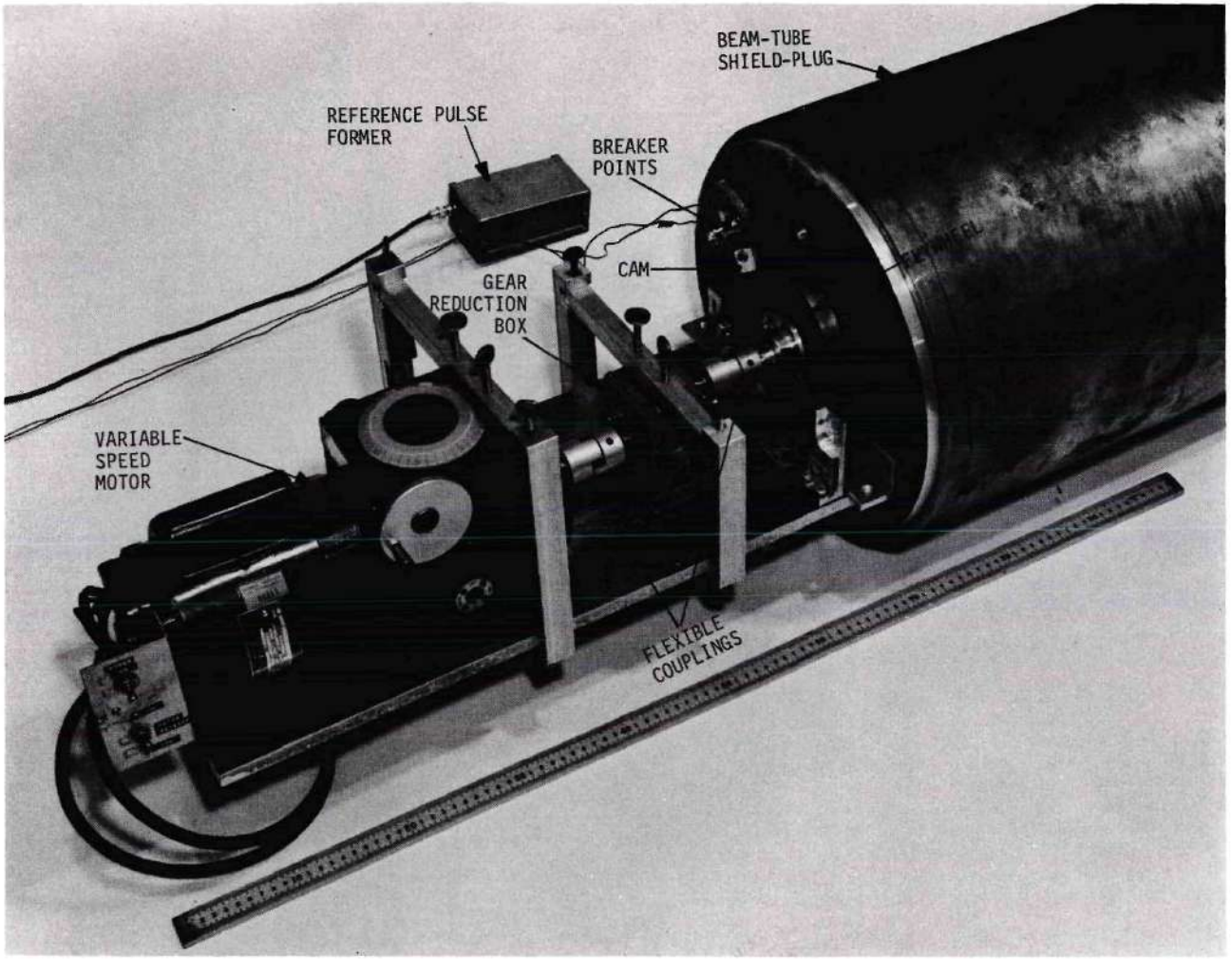

Figure 8. Pile Oscillator Drive Mechanism

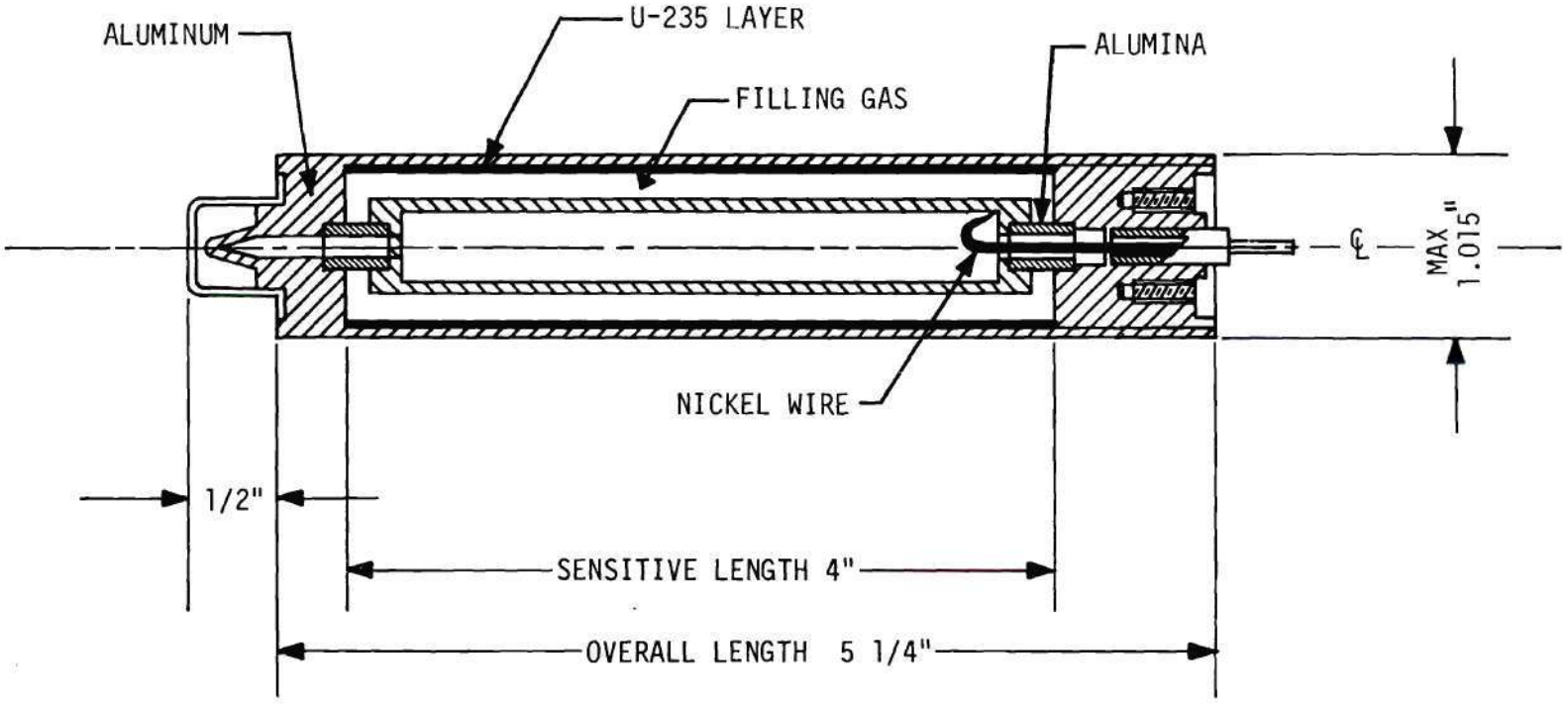

Figure 9. Cross Section Diagram of Fission Chamber

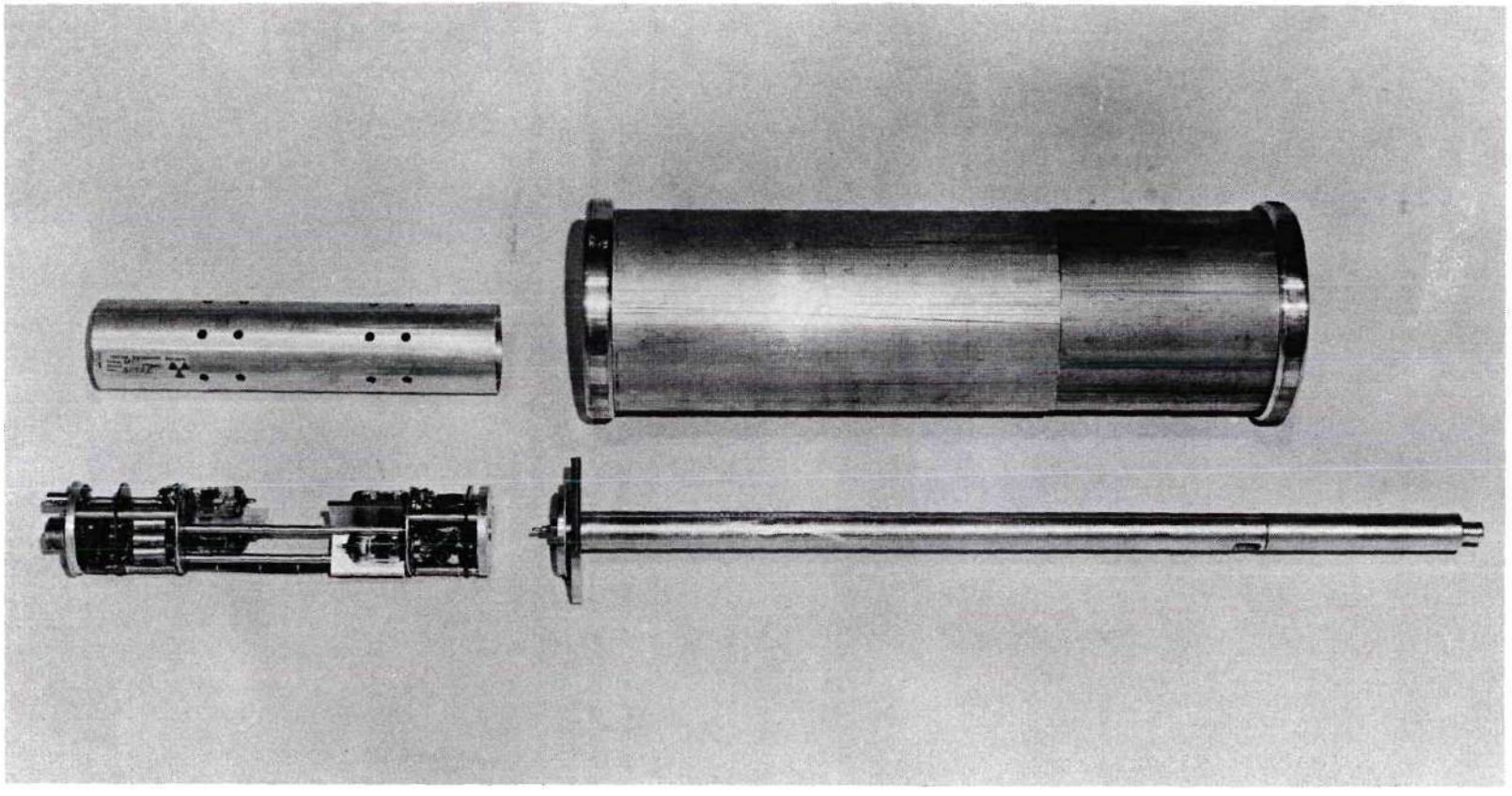

Figure 10. Fission Chamber, Radiation Shield, and Preamplifier

With sufficient amplification, the fission chamber system may be made sensitive to the alpha rays which are emitted by the fissile uranium coating of the chamber. However, without appreciable loss of neutron sensitivity, the system is capable of discriminating against these alpha rays. Figure 11, curve A, shows the response of the detector in a neutron field and curve B shows the response outside the neutron field, i.e., to the built-in alpha source. From Figure 11 it may be concluded that a region of relatively flat neutron flux response exists below 65 db gain and that, in this region, no background correction for alpha-produced pulses needs to be applied.

Data Recording System

To obtain gain and phase angle information, the sorting and storage of fission chamber pulses were synchronized with the pile oscillator. A Technical Measurement Corporation (TMC), Model 404, 400-channel analyzer operated in its "multiscaler" mode provided the means for data collection. (Hereafter, the 400-channel analyzer will be referred to as the multiscaler.) The procedure was to sort and store the counts from the fission chamber in the 400 time channels during one revolution of the drive shaft (two source cycles). Upon completion of one shaft revolution, the sequence was reinitiated and more counts accumulated in each channel to add to those already present. This technique was continued until an adequate number of counts per channel was obtained or until a preset time limit was reached.

To collect the data in the multiscaler, it was necessary to provide a channel advance signal at preset time intervals which would determine the individual channel time widths during one data collection cycle. Each

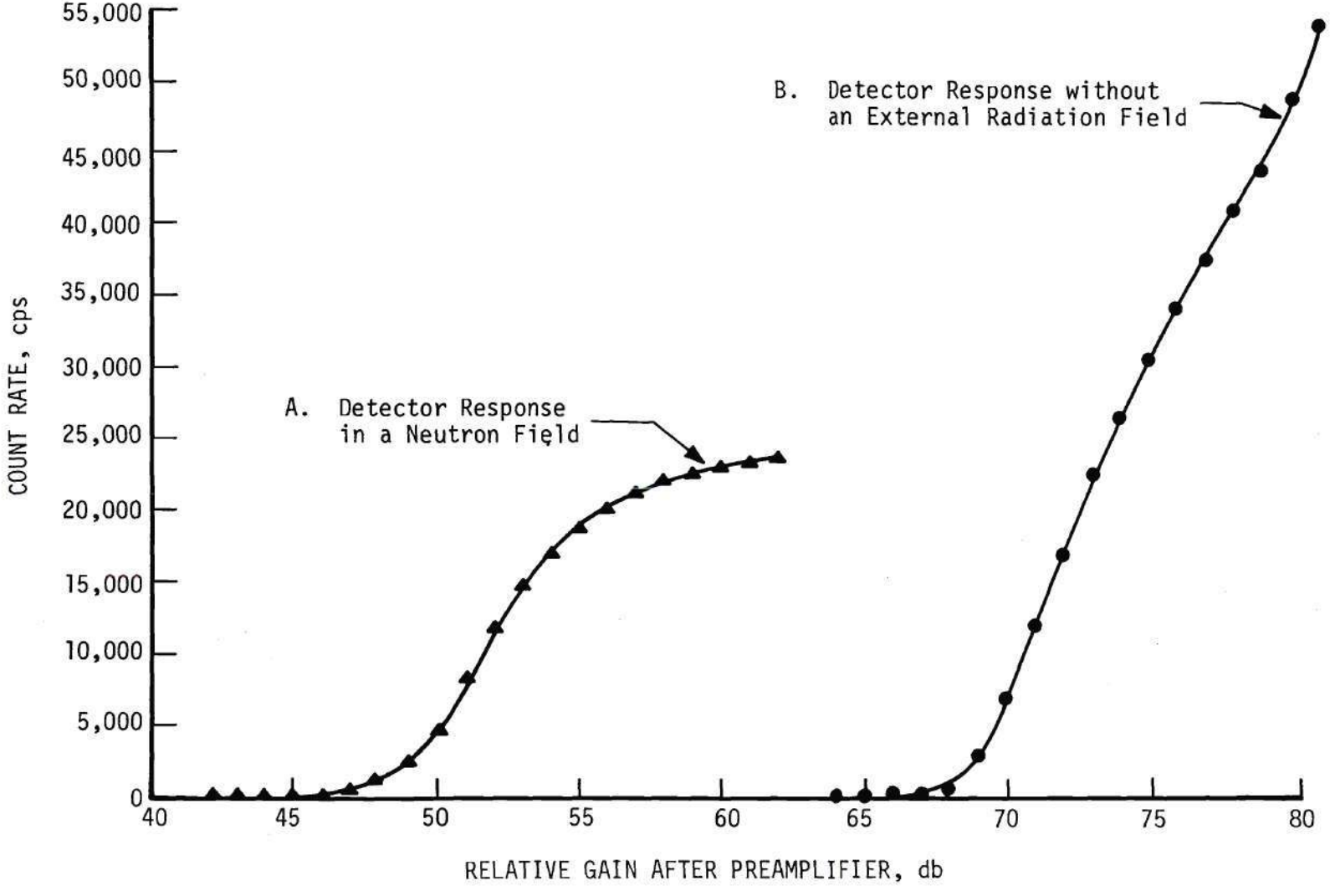

Figure 11. Performance Characteristics of Fission Chamber Both In and Out of the Reactor as a Function of Gain

data collection cycle corresponded to a sweep of the 400 channels which corresponded to one shaft revolution of the pile oscillator (giving 200 channels per source cycle). The required time intervals ranged from 0.05 second to 120 microseconds per channel, corresponding to the range of pile oscillator shaft speeds from 0.05 revolution per second to 20.6 revolutions per second. A free-running timing oscillator could not satisfy this requirement because of the variations in the motor speed. In other words, "exact" synchronization could not be accomplished between the pile oscillator shaft frequency and the multiscaler sweep frequency.

Initially, a Baldwin position encoder was used to synchronize the proper data collection channel with the shaft position of the pile oscillator. The encoder employed a photoelectric cell to emit a signal when struck by light transmitted through a disc which had slits cut at equal intervals. In order to account for two source cycles per shaft revolution, gears in the ratio of 1:2 served to connect the Baldwin encoder to the shaft. In an attempt to verify the performance of the system, a one-megacycle signal was fed into the multiscaler in place of the detector signal. The result should have been an equal accumulation of pulses in all channels within least count errors, i.e., if the speed of the shaft were uniform, then equal position increments would produce equal time increments. However, the test showed systematic variations of about ten percent among the 400 channels in the number of pulses stored. Several attempts to correct the performance resulted in little improvement. The primary cause of the difficulty was due to the drive shaft mounting and the lack of tolerances close enough to insure sufficiently small shaft vibrations. Additionally, due to the inherent design

of the Baldwin encoder, the time of each output signal relative to the shaft position varied slightly depending upon the speed of rotation of the encoder. Since the experiment covered a wide range of frequencies, this feature was undesirable.

An alternate scheme was implemented to ensure the proper data collection sequence, consisting of a timing (relaxation) oscillator having the provision for a reset synchronous signal (derived from the breaker points on the pile oscillator). The schematic diagram of the timing oscillator used is included in Appendix D. The output pulse from this oscillator was passed through a pulse shaping network (schematic diagram in Appendix D) and connected directly to the "dwell advance" jack, J-105, of the multiscaler to sequence the 400 channels successively. Hence, once a data collection cycle was initiated, the output from the timing oscillator provided the channel advance commands necessary to complete a sweep of all 400 channels. However, this process did not repeat until a new data collection cycle was initiated. The advance command signal received from the timing oscillator marking the end of channel 399 (channel zero was the first channel) caused the multiscaler to advance to the "stop" mode. Then, a special "ready accumulate" command derived from the breaker points was required on the jack, J-111, to initiate another data collection cycle. This same command pulse simultaneously reset the timing oscillator.

An approximation of the time per channel required was obtained by dividing the time per shaft revolution by 400. Variable resistors and capacitors in the timing oscillator circuit were set to provide the time per channel. Due to the design characteristics of the multiscaler, a

"ready accumulate" command on J-111 can only be processed if the multiscaler is in the "stop" mode prior to the command. With the aid of an oscilloscope, a fine adjustment of the time per channel was made so that just prior to the next breaker point impulse, the multiscaler was in the "stop" mode. Slight variations in motor speed resulted in a variable stop time. At all frequencies used, the total variation in stop time was less than half a channel width. Upon completion of one shaft revolution, the entire sequence was repeated with the counts from successive sweeps accumulated in each channel. An "on-off" switch permitted the "ready accumulate" command to energize the multiscaler. A consequence of this technique was that no partial cycle of data could be collected. Once a "ready accumulate" command had been accepted, a complete data collection cycle was processed. The next cycle was initiated or not, depending upon the position of the switch.

The signal derived from the breaker points was also directed via the switch to a Tracer Matic Utility Scaler Model Sc-90, which counted the total number of drive shaft revolutions. To measure the total time of data collection, a Preset Universal EPUT and Timer, Beckman Model 7361, was used. The time interval measured was between the first reference pulse signal received after the switch was thrown "on" and the first reference pulse signal received after the switch was thrown "off." In this manner, the terminating reference pulse was used to indicate the end of the last data collection cycle rather than the beginning of the next collection cycle.

The data collected at a given pile oscillator frequency were stored on punched paper tape. With a TMC Model 520 Punch Control unit with a

Tally Model 420 Tape Perforator, the contents of the multiscaler memory were transferred to paper tape. Prior to readout, the punch control unit was used to manually punch coded information on the paper tape to identify the particular run which had been completed. A TMC Printer, Model No. 500 P, was also available to obtain the output from the multiscaler memory in a readable form, if necessary. The detection and data recording equipment as used in the experiment are shown in Figure 12.

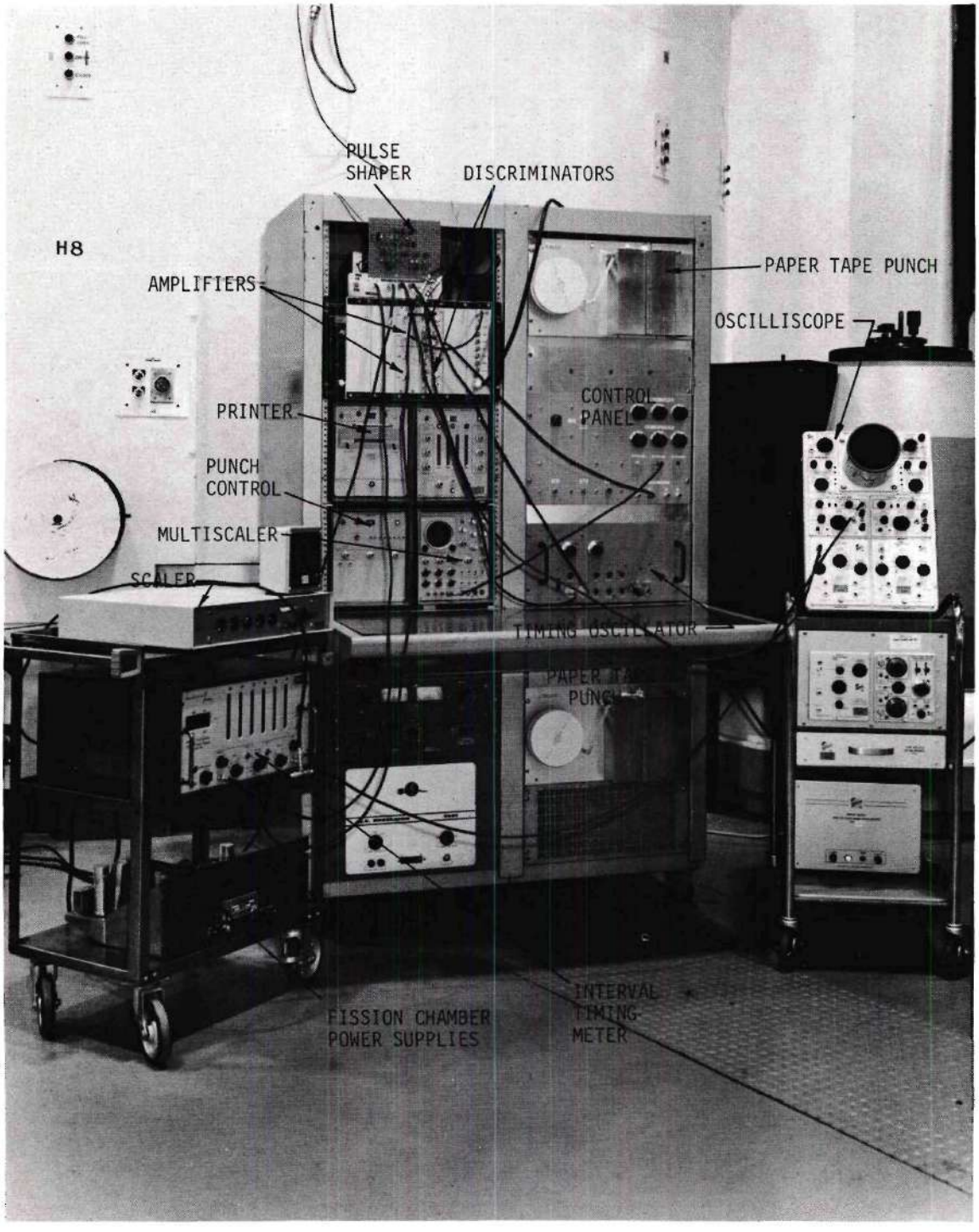

Figure 12. Detection and Data Recording Equipment for GTRR Pile Oscillator Experiment

CHAPTER III

EXPERIMENTAL PROCEDURES AND RESULTS

Core Configuration

The experimental results of this research were compared with similar quantities computed from a mathematical idealization which attempted to describe the experiment performed. The mathematical assumptions to be discussed in Chapter IV, Theory, made no allowance for local flux perturbations which were produced in the real reactor by the control blades. The semaphore type of control blade, as used in the GTRR, is particularly difficult to describe mathematically. Therefore, to diminish the effect of the blades, a minimum critical core loading was utilized so that the control blades were withdrawn a maximum amount from the core, reducing their effect on the flux profile at the core mid-plane. Originally, the reactor was critical with ten fuel elements. However, with the additional negative reactivity introduced by the pile oscillator, it was necessary to use a core loading of 10-1/2 elements. Complete elements occupied positions V 2, 4-7, 9-11, 14, and 15. The partial fuel element was located in V 18, and dummy elements filled the remaining positions, as shown in Figure 13. The partial fuel element, in this case, had five active fuel plates, whereas normally there are ten. This loading resulted in a banked-critical control blade configuration of 34 degrees. The relationship of the control blades in this position to the fuel region of the core is shown in Figure 14. The integral worth curve for a typical control blade

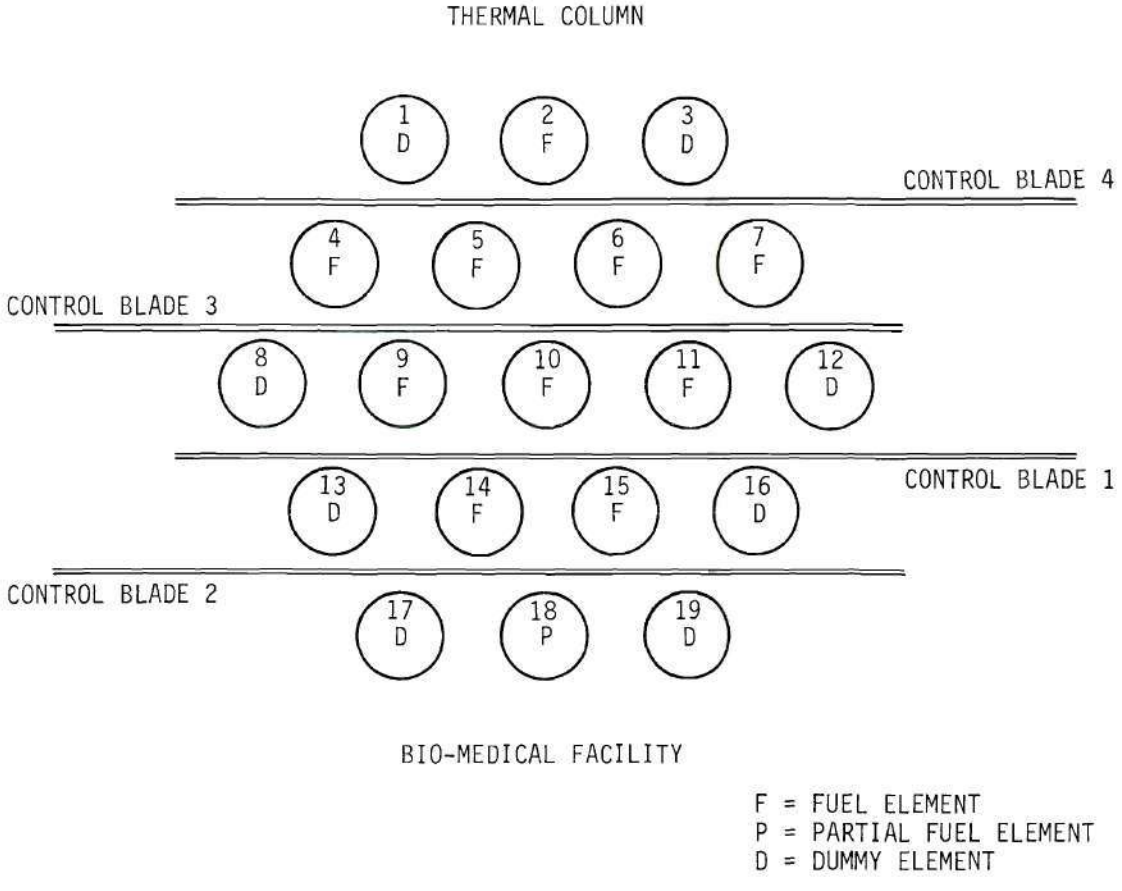

Figure 13. Actual Fuel Loading Configuration in GTRR for Pile Oscillator Experiment

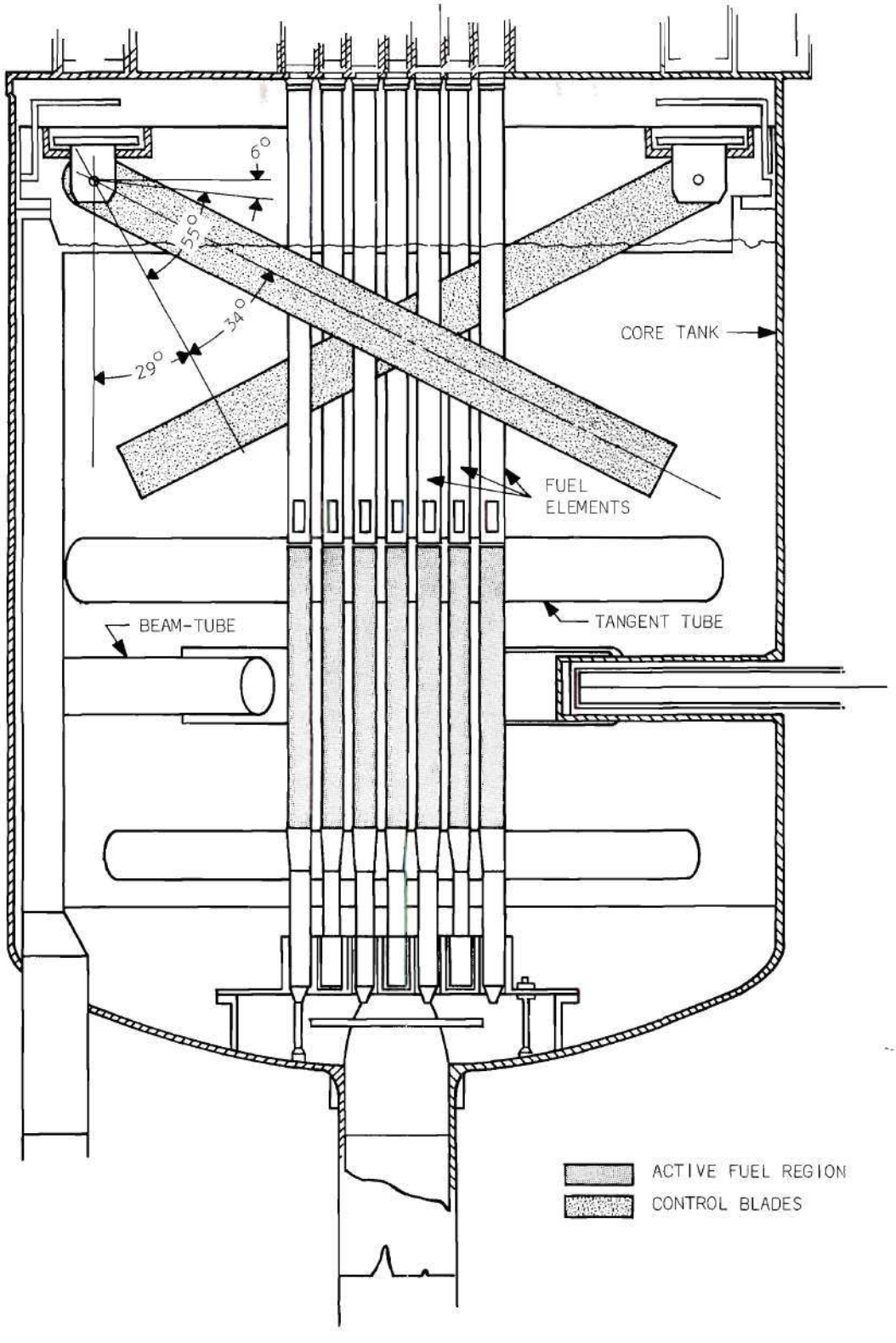

Figure 14. Vertical Section Through GTRR Core Tank Showing Banked Critical Control Blade Configuration

is shown in Figure 15. The curve shows that at 34 degrees a control blade is relatively "worthless" and thus produces a negligible perturbation on the flux distribution at the mid-plane of the core. In fact, from Figure 15, the differential worth of the control blade at 34 degrees is approximately 0.01 percent $\Delta k/k$ per degree.

With the reactor in the condition described above, the pile oscillator was situated on the core mid-plane. A fission detector was used to measure the response of the neutron flux at various locations on the core mid-plane. This experimental arrangement provided a configuration amenable to a two-dimensional mathematical description.

Pile Oscillator and Detector Positioning

The pile oscillator described in the previous chapter was initially located in beam-tube H-8 (Figure 3). This beam port has a nominal four-inch inside diameter and thus required use of the 3-1/2 inch diameter stator. With the detector in H-9 located within the graphite reflector region, the preliminary data collected were satisfactory. However, the response of the detector to the oscillations was negligible when located in H-4, opposite H-8. Using cadmium leaves as long as 16 inches produced relatively poor results. Additional cadmium length beyond the original ten inches had no significant effect on the response. This is the consequence of two conditions. The flux depression produced by the initial length of the cadmium reduced the flux seen by the added length. Also, because the additional length was further from the maximum thermal flux, its reactivity worth was reduced considerably.

The optimum beam-tube location for the pile oscillator was H-1

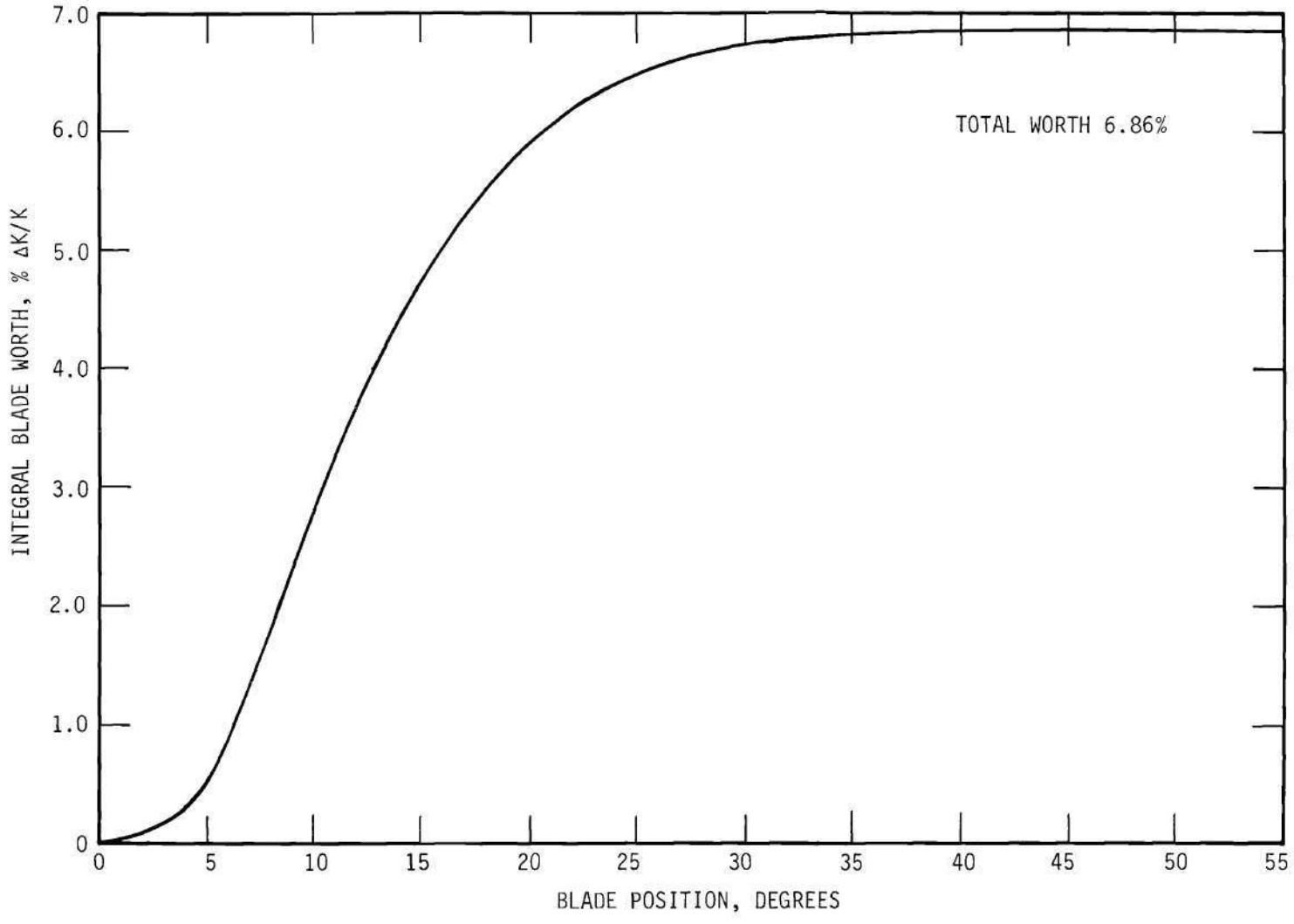

Figure 15. Integral Worth Curve for a Typical Control Blade

because this tube penetrates the heavy-water reflector as deeply as any of the other beam tubes and, in addition, it is the only one with a six-inch inside diameter. The large stator, 5-1/2 inches in diameter, was employed and the cadmium leaves were placed as close to the end of the oscillator assembly as possible (Chapter II, Figure 5). Preliminary data collection, with the detector located in position 6 (Chapter II, Figure 3), showed a reasonable response for this configuration. Thus, H-1 was used for the pile oscillator location for all the experimental results to be reported. The center of the cadmium region was 21 inches from the center of the core. The reactivity worth of the pile oscillator (maximum cadmium exposed) experiment was 0.00426 $\Delta k/k$ as determined by the regulating rod. Authorization was received from the Atomic Energy Commission to operate the pile oscillator without any limitation on frequency. The Commission stipulated that the maximum reactivity worth for any experiment which was to be introduced or withdrawn while the control blades were not fully inserted should be limited to 0.001 $\Delta k/k$. The maximum differential reactivity worth of the rotating cadmium leaves of the pile oscillator was 0.00082 $\Delta k/k$ as determined by the regulating rod.

Selection of the detector locations was based upon the desire to observe the largest space effects possible. Two locations, H-7 and H-3, were not available at the time of this research because of their involvement in neutron diffraction experiments. Use of the rectangular beam-tube H-10 was permissible, but its use would have required special modification of the detector. Selection of the six detector positions, as shown in Figure 3, was determined primarily by the experimental objectives

but was also influenced by the available reactor time. For positions 1, 3, and 4, the detector was 25.4 inches from the center of the core and for positions 2, 5, and 6, it was 66.0 inches from the center of the core. Since all data were collected with the pile oscillator in H-1 and the cadmium configuration fixed, the two variables which distinguished each run were the rotation speed of the pile oscillator and the location of the detector. The experimental results from these locations provided sufficient evidence of the phenomena being investigated.

Data Collection

The equipment used for data collection and storage has been described in Chapter II, Instrumentation and Equipment. Figure 16, a schematic diagram of the experimental equipment arrangement, shows the relationship between the various components. The techniques applied and the procedures followed for data acquisition will now be detailed.

Although the design thermal power of the GTRR is one megawatt, low-power tests were in progress at the time of this research and the power level of the reactor was maintained below 200 watts. The majority of the experimental runs was made with the reactor power level between one and six watts. With the circulating pumps running, no detectable temperature drop existed across the core and the core temperature was typically 72°F. Under these conditions, the approximation to a zero-power reactor was good.

The speed of the pile oscillator was set by routing the reference pulse to the interval timing meter and the scaler by the "on-off" switch in the "on" position (Figure 16). After a brief interval of time, the switch was turned off, stopping the interval timing meter and preventing

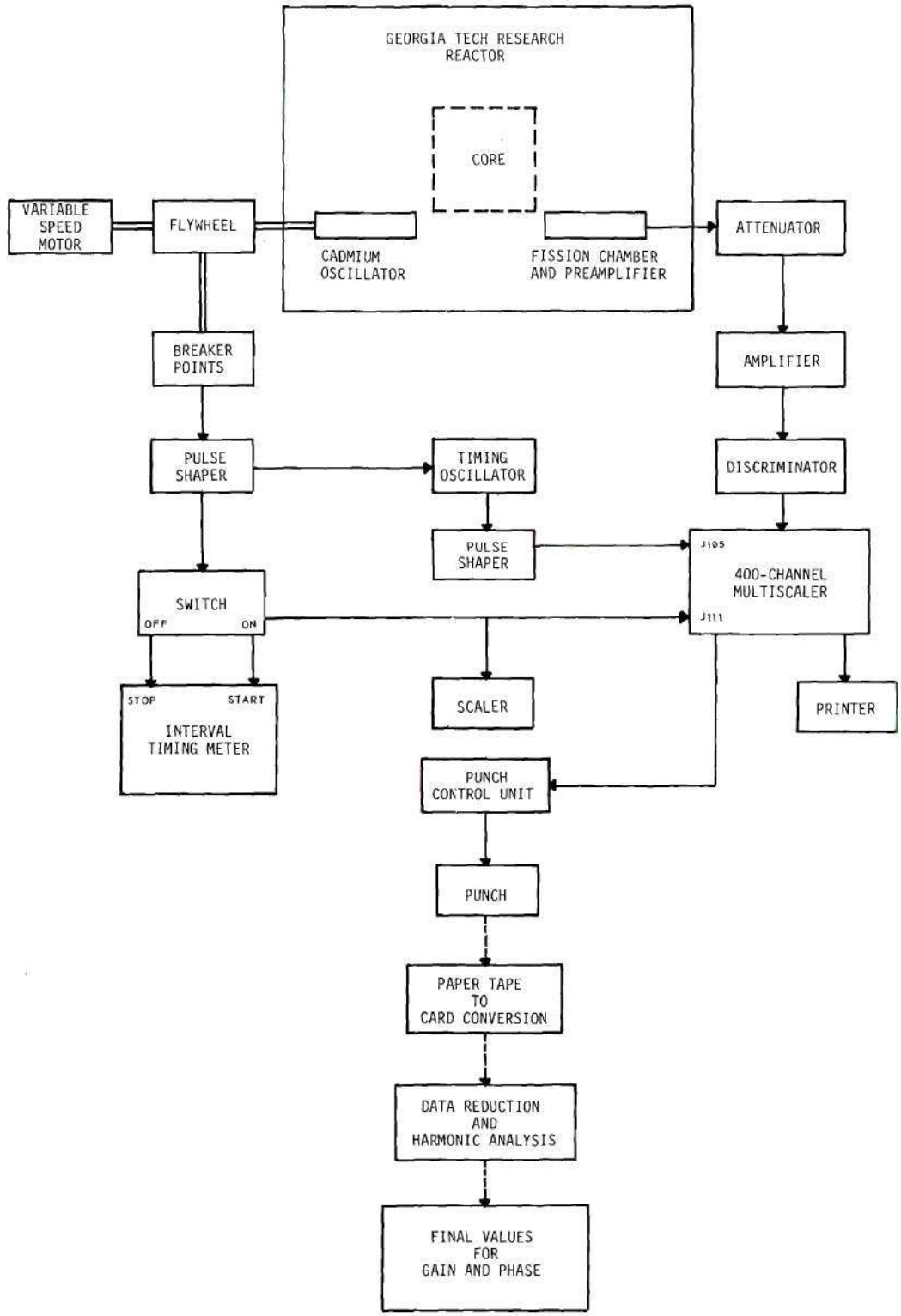

Figure 16. Schematic Diagram of Data Acquisition and Processing

any further reference pulses from being counted by the scaler. The frequency of the pile oscillator was calculated by dividing the counts recorded in the scaler by the time read on the interval timing meter. Adjustment of the hand crank on the variable speed transmission provided the means for minor speed corrections. The entire procedure was repeated until a satisfactory frequency was obtained. This is a trial and error technique, but it must be realized that there is no requirement for the attainment of a specific prearranged frequency. The objective is to collect data for speeds spaced throughout several decades of frequencies. Therefore, in adjusting the speed of the oscillator, the experimentor was attempting to arrive at a value within a range about some desired frequency.

During the initial adjustments prior to actual data collection, the pulse from the breaker points (which synchronized the electronics with the rotor, as described in Chapter II) was monitored on an oscilloscope. Observation of this pulse indicated if the breaker points were switching properly and also provided another estimate of the frequency. A pulse was initiated when the points were opened. Therefore, it was possible to obtain spurious pulses if "bouncing" of the points occurred. (Figure 59 in Appendix D shows the schematic diagram of the pulse-forming circuit.) Adjustments could be made to vary the spring pressure on the points to eliminate bouncing. The adjustment was found to be very critical and to be dependent on the frequency of the rotor. Apparently a slight looseness in the bearing nearest the flywheel permitted the cam rotation path to change with a change in frequency. Further use of this equipment would justify a significant effort to improve the reference pulse generation

procedure. Improvements were unnecessary for this research since the induction motor speed variations had a more significant effect than those attributable to breaker point settings. An improvement of the overall system might be accomplished by using a synchronous motor driven from a variable frequency source which in turn is synchronized with the dwell advance pulses.

Once a particular frequency had been selected, the timing oscillator was adjusted to provide the proper time per channel. It was necessary to monitor the output of the timing oscillator continuously because of drift during long data collection runs. The instabilities were primarily caused by thermal problems, although these were reduced to a minimum by insulation. Further details regarding this operation are contained in Appendix C.

Actual data collection was initiated by the switch previously described in Chapter II. With the switch off, the timing oscillator properly tuned, and the pile oscillator operating, the 400-channel memory of the multiscaler was cleared and the interval timer and the scaler were reset. Turning the switch on directed the next reference pulse to the scaler. This same reference pulse started the interval timer and put the TMC 400-channel multiscaler in the "ready accumulate" mode. At the same time, it reset the timing oscillator. Pulses from the fission chamber occurring during the time of one revolution of the pile oscillator shaft were then sorted and stored in the appropriate one of the 400 time channels. The entire process was repeated cyclically until terminated by the switch.

Using the TMC Model 520 Punch Control Unit, coded information, which contained the detector location and the frequency of the pile oscil-

lator, was manually punched into the leader of the paper tape. Upon command, the contents of the multiscaler memory were punched sequentially into the tape.

Data Reduction and Analysis

The information stored on the punched tape was converted to punched cards via an IBM Tape-to-Card Printing Punch. These cards contained the experimental values used by the B-5500 computer as input for the computer program DRAHA, which is reproduced and discussed in Appendix C.

The purpose of DRAHA was to correct the data for detector dead time and to adjust the results of the first datum point to account for the different collection time. In addition, it generated the necessary end points to provide data corresponding to two complete perturbation cycles. Details of these calculations are given in Appendix C. Following these adjustments, a harmonic analysis was performed on the corrected data, yielding gain and phase shift information for the particular frequency under consideration.

Experimental Results

As mentioned previously, the primary purpose of the experiment was to obtain evidence to show that the response of the neutron flux, when the reactor was subjected to a local periodic variation in the neutron absorption rate, did indeed depend upon the location of the monitoring device (detector). In other words, the experiment was performed to indicate the space-dependent response of the GTRR when subjected to a local disturbance. Tables 1 through 6 contain a summary of the experimental results and the results of the data reduction and analysis routine de-

scribed in Appendix C. In the tables, the quantity A_0 represents the DC component of the response. It is the average of the corrected counts for all 400 channels. The magnitude of A_0 is a function of the counting rate and the length of time during which data were collected. SUMTEST is computed as described in Appendix C in order to obtain a measure of the "goodness" of fit of the experimental values to the results of the harmonic analysis. It was considered a "good" fit if SUMTEST was of the order of 400, which would indicate that deviation from the fit was primarily due to the random error of the points. The number in parentheses beside the value in the column below SUMTEST indicates the number of harmonics used for the calculation. This number is equal to eight, if not shown.

Figures 17 and 18 show the space-dependence of the amplitude and phase shift as a function of frequency. The curves are visual fits to the data points. Chapter II, Figure 3 illustrates the relationship between the various detector positions and the pile oscillator.

Table 1. Experimental Results for Detector in H-2, Position 1

Frequency (cps)	Phase Shift (degrees)	Amplitude $\|W\|$	A_o	SUMTEST S(H)
0.149	-15.14	1.26	189,987	462
0.226	-14.91	1.22	178,772	400
0.343	-16.94	1.16	175,663	582
0.497	-19.70	1.12	185,343	490
0.705	-23.45	1.06	183,791	479
1.09	-29.57	0.950	203,658	499
1.66	-35.73	0.802	182,116	483
2.53	-38.92	0.636	241,119	404
3.64	-39.74	0.510	214,602	428
5.45	-36.97	0.406	266,849	397 (6)
7.20	-33.19	0.358	265,878	366 (4)
12.3	-25.38	0.304	251,177	446
18.7	-21.55	0.288	241,228	392 (6)
30.6	-20.50	0.270	278,280	417
41.3	-21.84	0.263	217,838	466

Table 2. Experimental Results for Detector in H-2, Position 2

Frequency (cps)	Phase Shift (degrees)	Amplitude |W|	A_o	SUMTEST S(H)
0.100	-15.26	1.27	314,807	620
0.145	-15.08	1.20	201,563	529
0.222	-14.77	1.15	199,102	544
0.337	-15.97	1.11	194,472	477
0.496	-18.87	1.06	196,984	490
0.703	-23.00	0.993	201,827	489
1.09	-29.42	0.888	198,466	451
1.66	-36.47	0.743	200,957	445
1.66	-36.41	0.743	177,484	459
2.51	-42.81	0.587	252,979	392 (5)
3.64	-43.78	0.464	232,911	387 (7)
5.45	-41.46	0.370	210,820	388 (3)
7.12	-38.57	0.326	210,572	420
12.26	-34.48	0.277	243,727	417
12.31	-34.13	0.273	427,859	419
18.70	-35.17	0.250	473,615	390 (5)
28.85	-37.27	0.233	487,566	464
41.4	-45.87	0.217	227,038	469
41.4	-45.69	0.217	439,475	479

Table 3. Experimental Results for Detector in H-5, Position 3

Frequency (cps)	Phase Shift (degrees)	Amplitude $\|W\|$	A_o	SUMTEST S(H)
0.149	-19.34	1.03	408, 281	424
0.416	-23.27	0.905	400, 239	397
0.416	-22.79	0.912	416, 041	455
0.699	-30.69	0.831	486, 275	455
1.66	-51.77	0.608	508, 173	420
3.62	-72.22	0.348	533, 587	437
7.84	-88.73	0.170	543, 893	396 (2)
12.30	-95.73	0.109	453, 438	399 (4)
12.38	-98.41	0.107	368, 431	436
18.7	-106.44	0.0707	944, 922	445
29.6	-117.06	0.0434	661, 767	389 (2)
41.3	-130.51	0.0301	864, 484	480

Table 4. Experimental Results for Detector in H-6, Position 4

Frequency (cps)	Phase Shift (degrees)	Amplitude |W|	A_o	SUMTEST S(H)
0.103	-21.60	1.080	407, 365	532
0.148	-20.47	1.028	466, 008	485
0.224	-20.51	0.966	463, 278	486
0.334	-22.07	0.923	419, 345	460
0.493	-25.87	0.876	320, 099	489
0.699	-30.74	0.828	318, 647	484
1.09	-40.10	0.731	394, 875	483
1.66	-52.44	0.606	428, 065	547
2.40	-62.71	0.481	628, 724	412
3.74	-74.43	0.334	442, 139	440
5.51	-84.00	0.234	429, 166	416
7.78	-91.10	0.181	631, 857	473
12.3	-100.94	0.105	783, 669	408
18.6	-112.52	0.0697	721, 289	404
30.5	-132.11	0.0379	841, 345	513
41.3	-148.20	0.0274	931, 266	590

Table 5. Experimental Results for Detector in H-5, Position 5

Frequency (cps)	Phase Shift (degrees)	Amplitude $\|W\|$	A_o	SUMTEST S(H)
0.106	-19.87	1.001	352, 348	493
0.156	-20.34	0.948	355, 469	516
0.341	-22.80	0.858	482, 386	539
0.705	-32.36	0.761	603, 444	536
1.66	-54.09	0.548	555, 788	418
3.60	-75.21	0.313	479, 265	397
7.91	-93.06	0.150	570, 302	444
12.3	-105.86	0.0957	599, 356	472
19.3	-120.05	0.0566	424, 871	400 (4)
28.8	-132.71	0.0387	619, 172	437
41.3	-153.49	0.0239	820, 250	536

Table 6. Experimental Results for Detector in H-6, Position 6

Frequency (cps)	Phase Shift (degrees)	Amplitude |W|	A_o	SUMTEST S(H)
0.096	-23.65	0.928	106,415	479
0.253	-22.74	0.808	102,286	425
0.414	-26.63	0.760	121,596	443
0.647	-31.66	0.712	276,494	440
0.998	-40.82	0.641	290,802	427
1.66	-54.97	0.521	316,171	406
2.37	-65.77	0.424	362,531	480
2.40	-66.99	0.413	551,003	455
3.41	-75.85	0.317	364,281	408
3.55	-78.54	0.307	710,133	446
5.42	-88.16	0.208	402,011	378 (2)
18.6	-130.58	0.0588	1,016,140	556
30.4	-152.37	0.0284	935,927	323 (1)

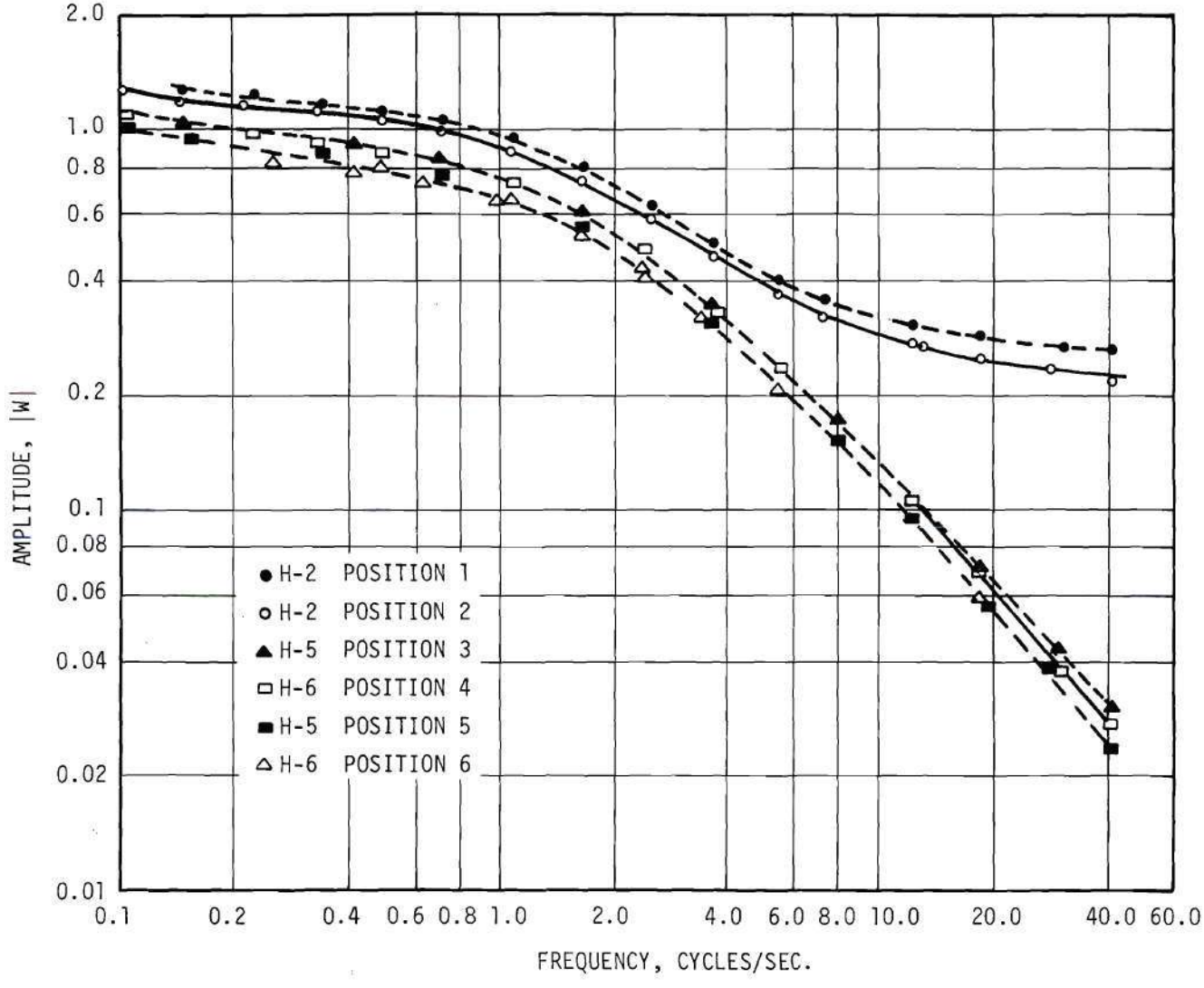

Figure 17. Amplitude of Zero-Power Reactor Source Transfer Function versus Frequency for Various Detector Positions -- Experimental Results from GTRR

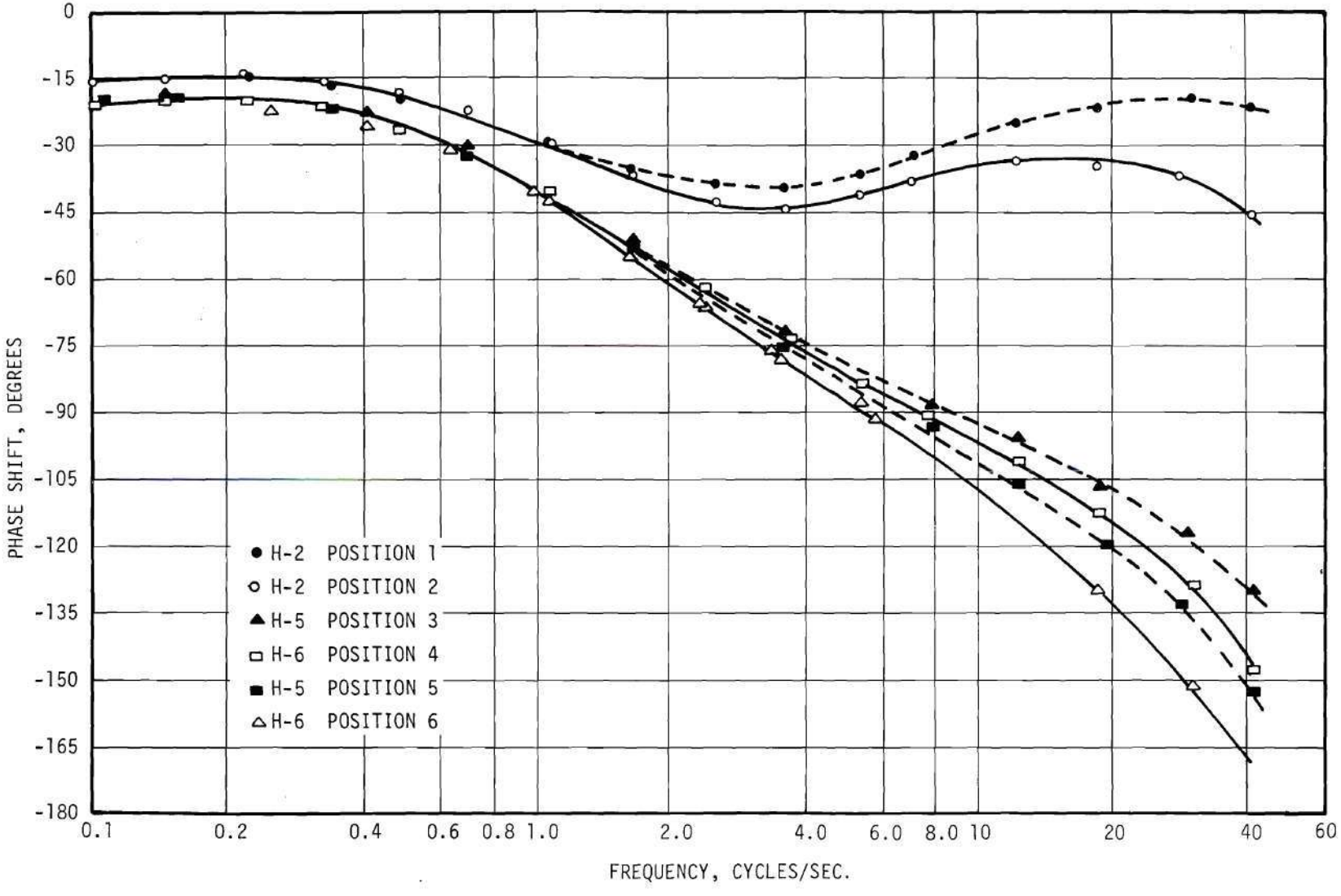

Figure 18. Phase Angle of Zero-Power Reactor Source Transfer Function versus Frequency for Various Detector Positions -- Experimental Results from GTRR

CHAPTER IV

THEORY

In general, a space-time analysis of a given system would attempt to predict, at any point in the system, the response to an arbitrary disturbance occurring anywhere within the system. As an example, consider a system to be defined as a reactor with its associated hardware (pumps, heat exchangers, etc.). A particular space-time analysis of this system could attempt to predict, at any point within the reactor, the response of the neutron flux to an arbitrary disturbance occurring anywhere within the system. The complexity of this problem is immediately evident upon realizing that an arbitrary disturbance includes large effects which would make the analysis highly nonlinear. Even with the aid of high speed digital computers, the "ideal" solution for a space-time analysis of a moderately complex system will be extremely elusive, if possible at all.

If any degree of success is to be achieved in conducting a reactor system space-time analysis, it appears necessary to define a simple system and also to place restrictions on the type of disturbance to be permitted. Although there is considerable literature on this subject involving various restrictions and assumptions on the reactor system, there is a distinct void on practical methods of formulation and solution for realistic situations. In an attempt to partially fill this void, equations will be derived in a general form to predict at any point within a stationary fueled reactor the amplitude and phase of the response in the neutron flux

when the reactor is subjected to a small, periodic disturbance. The subsequent chapter, in applying these results, will show how existing nuclear codes can be used to obtain the desired information. Therefore, this technique[21,22] provides a practical method of formulation and solution for a class of reactor space-time analysis problems subject to the stipulations to be enumerated.

The multigroup, multiregion representation of the telegrapher's equation,[23,24] including the effects of delayed neutrons, was used as the basis for the derivation.

$$D_j(\bar{x})\nabla^2 \Phi_j(\bar{x},t) - \Sigma_j^t(\bar{x})\,\Phi_j(\bar{x},t) + \frac{1}{k}\left[S_j^p(\bar{x},t) + S_j^d(\bar{x},t)\right] + S_j^s(\bar{x},t) \quad (1)$$

$$+ S_j(\bar{x},t) = \left(\frac{1 + 3\,\Sigma_j^t(\bar{x})D_j(\bar{x})}{v_j(\bar{x})}\right)\frac{\partial\Phi_j(\bar{x},t)}{\partial t} + \frac{3\,D_j(\bar{x})}{v_j(\bar{x})^2}\,\frac{\partial^2\Phi(\bar{x},t)}{\partial t^2}$$

where

$D_j(\bar{x})$ = the space-dependent diffusion coefficient for neutrons in energy group (interval) j

$v_j(\bar{x})$ = the average velocity for neutrons in energy group j at point $\bar{x}$

$\Phi_j(\bar{x},t)$ = the neutron flux in energy group j at point $\bar{x}$ and time t

$\Sigma_j^t(\bar{x})$ = the space-dependent total macroscopic removal cross section for neutrons in energy group j

$$= \Sigma_j^a(\bar{x}) + \sum_{g=1}^{n} \Sigma_{j\to g}^s(\bar{x})$$

(where

$\Sigma_j^a(\bar{x})$ = the space-dependent macroscopic absorption cross section for neutrons in energy group j

$\sum_{g=1}^{n} \Sigma_{j\to g}^s(\bar{x})$ = the summation over all energy groups (g = 1 to n) of the space-dependent macroscopic cross section for scattering of a j^{th} group neutron to group g, $\Sigma_{j\to g}^s(\bar{x})$)

$S_j^p(\bar{x}, t)$ = the fission source term for prompt neutrons produced in energy group j at point $\bar{x}$ and time t

$$= \chi_j(\bar{x})(1 - \beta(\bar{x})) \sum_{g=1}^{n} \nu_g(\bar{x})\, \Sigma_g^f(\bar{x})\, \Phi_g(\bar{x}, t) \qquad (2)$$

(where

$\nu_g(\bar{x})$ = the average number of neutrons emitted at point $\bar{x}$ per fission by a neutron within energy group g

$\Sigma_g^f(\bar{x})$ = the space-dependent macroscopic fission cross section for neutrons in energy group g

$\beta(\bar{x})$ = the fraction of neutrons from fission which is delayed at point $\bar{x}$

$\chi_j(\bar{x})$ = the fraction of the prompt neutrons from fission produced in energy group j $\left(\sum_{j=1}^{n} \chi_j(\bar{x}) = 1 \right)$ at point $\bar{x}$)

$S_j^d(\bar{x}, t)$ = the source term for delayed neutrons produced in energy interval j at point $\bar{x}$ and time t

$$= \alpha_j(\bar{x}) \sum_{i=1}^{m} \lambda_i C_i(\bar{x}, t) \qquad (3)$$

(where

$\alpha_j(\bar{x})$ = the fraction of delayed neutrons produced in energy group j $\left(\sum_{j=1}^{n} \alpha_j(\bar{x}) = 1 \right)$ at point $\bar{x}$

$C_i(\bar{x}, t)$ = the space- and time-dependent concentration of the i^{th} delayed neutron precursor

λ_i = the decay constant of the i^{th} delayed neutron precursor

m = the total number of delayed neutron precursors)

$S_j^s(\bar{x}, t)$ = the source term for neutrons scattered into energy group j at point $\bar{x}$ and time t

$$= \sum_{g=1}^{n} \Sigma^s_{g \to j}(\bar{x}) \, \Phi_g(\bar{x}, t) \qquad (4)$$

$S_j(\bar{x}, t)$ = the external source term (independent of the neutron flux)

The factor $1/k$ in equation 1 was introduced for mathematical convenience.[25] By adjusting k, the eigenvalue, the time behavior predicted from equation 1 will not be merely the result of incorrect values for any of the cross sections or of a gross assumption. That is, if a reactor known to be critical is described mathematically with $k = 1$ and equation 1 does not predict a stationary state in the absence of the external source term, then k can be adjusted until the desired stationary state is obtained. Interpretation of the reactor's time behavior predicted from equation 1 is then based upon perturbations of this "forced" stationary state.

The equation governing the precursor concentration, $C_i(\bar{x}, t)$ is

$$\frac{\partial C_i(\bar{x}, t)}{\partial t} = \beta_i(\bar{x}) \sum_{g=1}^{n} \nu_g(\bar{x}) \Sigma_g^f(\bar{x}) \Phi_g(\bar{x}, t) - \lambda_i C_i(\bar{x}, t) \tag{5}$$

where

$\beta_i(\bar{x})$ = the fraction of neutrons from a fission at point $\bar{x}$ which is attributable to the i^{th} delayed neutron precursor

$$\left(\sum_{i=1}^{m} \beta_i(\bar{x}) = \beta(\bar{x}) \right)$$

Cohn[26] has pointed out that small changes in the configuration of the reactor, i.e., reactivity changes, may be treated as external sources wherever the assumption of linearity is valid. Thus, under the restriction that only small disturbances are to be considered (i.e., the small-signal approximation[27]), the time-dependent quantities in equations 1 and 5 are represented as follows:

$$\Phi_j(\bar{x}, t) = \Phi_j(\bar{x}) + \delta\Phi_j(\bar{x}, t) \tag{6}$$

$$S_j^p(\bar{x}, t) = S_j^p(\bar{x}) + \delta S_j^p(\bar{x}, t) \tag{7}$$

$$S_j^d(\bar{x}, t) = S_j^d(\bar{x}) + \delta S_j^d(\bar{x}, t) \tag{8}$$

$$S_j^s(\bar{x}, t) = S_j^s(\bar{x}) + \delta S_j^s(\bar{x}, t) \tag{9}$$

$$S_j(\bar{x}, t) = S_j(\bar{x}) + \delta S_j(\bar{x}, t) \tag{10}$$

$$C_i(\bar{x}, t) = C_i(\bar{x}) + \delta C_i(\bar{x}, t) \tag{11}$$

This description of the various quantities provides a separate representation of the response of the reactor to the fluctuating component of the external disturbance, $\delta S_j(\bar{x}, t)$. In other words, we are assuming that the time-dependent variations of the individual quantities can be represented by a small fluctuating component superimposed upon their respective steady-state values, which are functions of the space variables only.

Substituting equations 6 through 11 into equations 1 and 5 results in two sets of equations. The first set represents the static or steady-state description of the reactor.

$$D_j(\bar{x})\nabla^2 \Phi_j(\bar{x}) - \Sigma_j^t(\bar{x})\, \Phi_j(\bar{x}) + \frac{1}{k}\left[S_j^p(\bar{x}) + S_j^d(\bar{x})\right] + S_j^s(\bar{x}) + S_j(\bar{x}) \quad (12)$$

$$= \left(\frac{1 + 3\,\Sigma_j^t(\bar{x})\, D_j(\bar{x})}{v_j(\bar{x})}\right) \frac{\partial \Phi_j(\bar{x})}{\partial t} + \frac{3\, D_j(\bar{x})}{v_j(\bar{x})^2} \frac{\partial^2 \Phi_j(\bar{x})}{\partial t^2} = 0$$

$$\frac{\partial C_i(\bar{x})}{\partial t} = 0 = \beta_i(\bar{x}) \sum_{g=1}^{n} \nu_g(\bar{x})\, \Sigma_g^f(\bar{x})\, \Phi_g(\bar{x}) - \lambda_i\, C_i(\bar{x}) \quad (13)$$

The solution to this set of equations which satisfies the appropriate boundary conditions represents the static flux shape. The difference between the required value of k and unity, for a critical configuration, is an indication of how good the set of constants and prior assumptions are.

The second set of equations represents the fluctuating component

of the neutron flux, which is superimposed upon the static flux distribution.

$$D_j(\bar{x})\nabla^2 \delta\Phi_j(\bar{x},t) - \Sigma_j^t(\bar{x})\,\delta\Phi_j(\bar{x},t) + \frac{1}{k}\left[\delta S_j^p(\bar{x},t) + \delta S_j^d(\bar{x},t)\right] \qquad (14)$$

$$+ \delta S_j^s(\bar{x},t) + \delta S_j(\bar{x},t)$$

$$= \left(\frac{1 + 3\,\Sigma_j^t(\bar{x})\,D_j(\bar{x})}{v_j(\bar{x})}\right)\frac{\partial\delta\Phi_j(\bar{x},t)}{\partial t} + \frac{3\,D_j(\bar{x})}{v_j(\bar{x})^2}\,\frac{\partial^2\delta\Phi_j(\bar{x},t)}{\partial t^2}$$

$$\frac{\partial\delta C_i(\bar{x},t)}{\partial t} = \beta_i(\bar{x}) \sum_{g=1}^{n} \nu_g(\bar{x})\,\Sigma_g^f(\bar{x})\,\delta\Phi_g(\bar{x},t) - \lambda_i\,\delta C_i(\bar{x},t) \qquad (15)$$

A solution of this set of equations with the proper spatial boundary conditions would yield the space- and time-dependent response of the neutron flux, $\delta\Phi_j(\bar{x},t)$, to the input disturbance $\delta S_j(\bar{x},t)$. In equation 14 the value of k is an input constant. If the value of k found in the solution to equations 12 and 13 is used, then the solution of equations 14 and 15 represents the response of a critical reactor. In order to study the effect of a small change in reactivity, an input value of k slightly different from that found for the static solution problem can be used (not necessarily slightly different from 1).

It will suffice to consider the case of a sinusoidal disturbance, since any reasonable periodic disturbance could be Fourier analyzed and each frequency component could be considered individually. Then, since the equations are linear, the principle of superposition can be applied

to find the response to the original disturbance. To expedite the solution,[28] the input disturbance (external source) is written as

$$\delta S_j(\bar{x}, t) = \underline{S}_j(\bar{x})\ e^{i\omega t} \tag{16}$$

where $\underline{S}_j(\bar{x})$ is a complex amplitude dependent upon position only. It is understood, as is customary, that only the real part of $\delta S_j(\bar{x}, t)$ is interpreted to have physical significance.[29] Since $\underline{S}_j(\bar{x})$ represents the input to the system, its phase is arbitrary so that it can be assumed to be real. However, an imaginary component is allowed for here in order to maintain the generality of the formulation to include the possibility of an input source whose phase is nonuniform over its extent. Because the system of equations being considered is linear, the steady-state output due to a sinusoidal input is sinusoidal and has the same frequency as the input.[30] Therefore, the neutron flux response is written as

$$\delta\Phi_j(\bar{x}, t) = \underline{\Phi}_j(\bar{x}, \omega)\ e^{i\omega t} \tag{17}$$

As a result of this approach, each of the other time-dependent quantities, $\delta S_j^p(\bar{x}, t)$, $\delta S_j^d(\bar{x}, t)$, $\delta S_j^s(\bar{x}, t)$, and $\delta C_i(\bar{x}, t)$, in equations 14 and 15 can also be represented in a like manner, as will be shown. Application of equation 2 to the fluctuating component gives

$$\delta S_j^p(\bar{x}, t) = \chi_j(\bar{x})[1 - \beta(\bar{x})] \sum_{g=1}^{n} \nu_g(\bar{x})\ \Sigma_g^f(\bar{x})\ \delta\Phi_g(\bar{x}, t) \tag{18}$$

Substituting for $\delta\Phi_g(\bar{x}, t)$ using equation 17 reduces equation 18 to the following

$$\delta S_j^p(\bar{x}, t) = \chi_j(\bar{x})[1 - \beta(\bar{x})] \sum_{g=1}^{n} \nu_g(\bar{x})\ \Sigma_g^f(\bar{x})\ \underline{\Phi}_g(\bar{x}, \omega)\ e^{i\omega t}$$

Thus

$$\delta S_j^p(\bar{x}, t) = \underline{S}_j^p(\bar{x}, \omega)\ e^{i\omega t} \tag{19}$$

where

$$\underline{S}_j^p(\bar{x}, \omega) = \chi_j(\bar{x})[1 - \beta(\bar{x})] \sum_{g=1}^{n} \nu_g(\bar{x})\ \Sigma_g^f(\bar{x})\ \underline{\Phi}_g(\bar{x}, \omega) \tag{20}$$

Assuming a particular solution of the form

$$\delta C_i(\bar{x}, t) = \underline{C}_i(\bar{x}, \omega)\ e^{i\omega t} \tag{21}$$

for equation 15 and using equation 17 to substitute for $\delta\Phi_g(\bar{x}, t)$, equation 15 becomes

$$\underline{C}_i(\bar{x}, \omega)\ e^{i\omega t}\ i\omega = \beta_i(\bar{x}) \sum_{g=1}^{n} \nu_g(\bar{x})\ \Sigma_g^f(\bar{x})\ \underline{\Phi}_g(\bar{x}, \omega)\ e^{i\omega t}$$

$$- \lambda_i \underline{C}_i(\bar{x}, \omega)\ e^{i\omega t}$$

or

$$\underline{C}_i(\bar{x}, \omega) = \frac{\beta_i(\bar{x}) \sum_{g=1}^{n} \nu_g(\bar{x})\ \Sigma_g^f(\bar{x})\ \underline{\Phi}_g(\bar{x}, \omega)}{\lambda_i(\bar{x}) + i\omega} \tag{22}$$

Using this result, the expression for $\underline{S}_j^d(\bar{x}, \omega)$ can be deduced using equation 3.

$$\delta S_j^d(\bar{x}, t) = \alpha_j(\bar{x}) \sum_{i=1}^{m} \lambda_i(\bar{x})\ \delta C_i(\bar{x}, t) \tag{23}$$

Upon substitution for $\delta C_i(\bar{x}, t)$ using equations 21 and 22, equation 23 becomes

$$\delta S_j^d(\bar{x}, t) = \alpha_j(\bar{x}) \sum_{i=1}^{m} \frac{\lambda_i(\bar{x})\ \beta_i(\bar{x})}{\lambda_i(\bar{x}) + i\omega} \times \sum_{g=1}^{n} \nu_g(\bar{x})\ \Sigma_g^f(\bar{x})\ \underline{\Phi}_g(\bar{x}, \omega)\ e^{i\omega t}$$

Thus

$$\delta S_j^d(\bar{x}, t) = \underline{S}_j^d(\bar{x}, \omega)\ e^{i\omega t} \tag{24}$$

where

$$\underline{S}_j^d(\bar{x}, \omega) = \alpha_j(\bar{x}) \sum_{i=1}^{m} \frac{\lambda_i(\bar{x})\ \beta_i(\bar{x})}{\lambda_i(\bar{x}) + i\omega} \times \sum_{g=1}^{n} \nu_g(\bar{x})\ \Sigma_g^f(\bar{x})\ \underline{\Phi}_g(\bar{x}, \omega) \tag{25}$$

From equation 4

$$\delta S_j^s(\bar{x}, t) = \sum_{g=1}^{n} \Sigma_{g\to j}^s(\bar{x})\ \delta\Phi_g(\bar{x}, t)$$

Substituting as before for $\delta\Phi_g(\bar{x}, t)$

$$\delta S_j^s(\bar{x}, t) = \sum_{g=1}^{n} \Sigma_{g\to j}^s(\bar{x})\ \underline{\Phi}_g(\bar{x}, \omega)\ e^{i\omega t}$$

or

$$\delta S_j^s(\bar{x}, t) = \underline{S}_j^s(\bar{x}, \omega)\ e^{i\omega t} \tag{26}$$

where

$$\underline{S}_j^s(\bar{x}, \omega) = \sum_{g=1}^{n} \Sigma_{g\to j}^s(\bar{x})\ \underline{\Phi}_g(\bar{x}, \omega) \tag{27}$$

Now substituting the expressions involving the complex amplitude times exp(iωt) for $\delta\Phi_j(\bar{x}, t)$, $\delta S_j^p(\bar{x}, t)$, $\delta S_j^d(\bar{x}, t)$, $\delta S_j^s(\bar{x}, t)$, and $\delta S_j(\bar{x}, t)$ (equations 17, 19, 24, 26, and 16, respectively) into equation 14 produces the following result.

$$D_j(\bar{x})\nabla^2\ \underline{\Phi}_j(\bar{x}, \omega) - \Sigma_j^t(\bar{x})\ \underline{\Phi}_j(\bar{x}, \omega) + \frac{1}{k}\left[\underline{S}_j^p(\bar{x}, \omega) + \underline{S}_j^d(\bar{x}, \omega)\right] + \underline{S}_j^s(\bar{x}, \omega) \tag{28}$$

$$+\ \underline{S}_j(\bar{x}) = \left(\frac{1 + 3\ \Sigma_j^t(\bar{x})\ D_j(\bar{x})}{v_j(\bar{x})}\right) \underline{\Phi}_j(\bar{x}, \omega)\ i\omega - \frac{3\ D_j(\bar{x})}{v_j(\bar{x})^2}\ \underline{\Phi}_j(\bar{x}, \omega)\ \omega^2$$

where the common factor exp(iωt) has been cancelled.

To summarize, the use of equation 16 to represent the external source or driving function and the application of some well-known results of linear equations reduced equation 14, which was a function of space and time, into equation 28 which is a function of space and frequency, but independent of time.

Using equations 20, 25, and 27, we rewrite equation 28 in terms of the response $\underline{\Phi}_j(\bar{x}, \omega)$ due to the disturbance $\underline{S}_j(\bar{x})$.

$$D_j(\bar{x})\nabla^2 \underline{\Phi}_j(\bar{x},\omega) - \Sigma_j^t(\bar{x},\omega)\,\underline{\Phi}_j(\bar{x},\omega) + \frac{1}{k}\left[(1-\beta(\bar{x}))\,\chi_j(\bar{x})\right. \tag{29}$$

$$\times \sum_{g=1}^{n} \nu_g(\bar{x})\,\Sigma_g^f(\bar{x})\,\underline{\Phi}_g(\bar{x},\omega) + \alpha_j(\bar{x}) \sum_{i=1}^{m} \frac{\beta_i(\bar{x})\,\lambda_i(\bar{x})}{\lambda_i(\bar{x}) + i\omega}$$

$$\left.\times \sum_{g=1}^{n} \nu_g(\bar{x})\,\Sigma_g^f(\bar{x})\,\underline{\Phi}_g(\bar{x},\omega)\right] + \sum_{g=1}^{n} \Sigma_{g\to j}^s(\bar{x})\,\underline{\Phi}_g(\bar{x},\omega) + \underline{S}_j(\bar{x})$$

$$= \left(\frac{1 + 3\,\Sigma_j^t(\bar{x})\,D_j(\bar{x})}{v_j(\bar{x})}\right)\underline{\Phi}_j(\bar{x},\omega)\,i\omega - \frac{3\,D_j(\bar{x})}{v_j(\bar{x})^2}\,\omega^2\,\underline{\Phi}_j(\bar{x},\omega)$$

Using the theory of complex linear equations, we define

$$\underline{\Phi}_j(\bar{x},\omega) = \phi_j^R(\bar{x},\omega) + i\,\phi_j^I(\bar{x},\omega) \tag{30}$$

where $\phi_j^R(\bar{x},\omega)$ and $\phi_j^I(\bar{x},\omega)$ represent the real and imaginary components of the complex quantity $\underline{\Phi}_j(\bar{x},\omega)$. Likewise, we define $\underline{S}_j(\bar{x})$ in a similar manner.

$$\underline{S}_j(\bar{x}) = S_j^R(\bar{x}) + i\,S_j^I(\bar{x}) \tag{31}$$

With the above two equations, substitution into equation 29 gives

$$D_j(\bar{x})\nabla^2 \phi_j^R(\bar{x},\omega) + i\,D_j(\bar{x})\nabla^2 \phi_j^I(\bar{x},\omega) - \Sigma_j^t(\bar{x})\,\phi_j^R(\bar{x},\omega) \tag{32}$$

$$- i\,\Sigma_j^t(\bar{x})\,\phi_j^I(\bar{x},\omega) + \frac{1}{k}\left[(1 - \beta(\bar{x}))\,\chi_j(\bar{x})\sum_{g=1}^{n}\nu_g(\bar{x})\,\Sigma_g^f(\bar{x})\,\phi_g^R(\bar{x},\omega)\right.$$

$$+ i\,(1 - \beta(\bar{x}))\,\chi_j(\bar{x})\sum_{g=1}^{n}\nu_g(\bar{x})\,\Sigma_g^f(\bar{x})\,\phi_g^I(\bar{x},\omega) + \alpha_j(\bar{x})\sum_{i=1}^{m}\frac{\beta_i(\bar{x})\,\lambda_i(\bar{x})}{\lambda_i(\bar{x}) + i\omega}$$

$$\times\sum_{g=1}^{n}\nu_g(\bar{x})\,\Sigma_g^f(\bar{x})\,\phi_g^R(\bar{x},\omega) + i\,\alpha_j(\bar{x})\sum_{i=1}^{m}\frac{\beta_i(\bar{x})\,\lambda_i(\bar{x})}{\lambda_i(\bar{x}) + i\omega}$$

$$\left.\times\sum_{g=1}^{n}\nu_g(\bar{x})\,\Sigma_g^f(\bar{x})\,\phi_g^I(\bar{x},\omega)\right] + \sum_{g=1}^{n}\Sigma_{g\to j}^s(\bar{x})\,\phi_g^R(\bar{x},\omega) + i\sum_{g=1}^{n}\Sigma_{g\to j}^s(\bar{x})\,\phi_g^I(\bar{x},\omega)$$

$$+ S_j^R(\bar{x}) + i\,S_j^I(\bar{x}) = i\omega\left(\frac{1 + 3\,\Sigma_j^t(\bar{x})\,D_j(\bar{x})}{v_j(\bar{x})}\right)\phi_j^R(\bar{x},\omega) - \omega\left(\frac{1 + 3\,\Sigma_j^t(\bar{x})\,D_j(\bar{x})}{v_j(\bar{x})}\right)$$

$$\times\,\phi_j^I(\bar{x},\omega) - \frac{3\,D_j(\bar{x})\,\omega^2}{v_j(\bar{x})^2}\,\phi_j^R(\bar{x},\omega) - \frac{i\,3\,D_j(\bar{x})\,\omega^2}{v_j(\bar{x})^2}\,\phi_j^I(\bar{x},\omega)$$

where $j = 1, 2, \ldots, n$. Equating the real and imaginary parts produces 2 n real equations.

$$D_j(\bar{x})\nabla^2\,\phi_j^R(\bar{x},\omega) - \Sigma_j^t(\bar{x})\,\phi_j^R(\bar{x},\omega) + \frac{1}{k}\left[(1 - \beta(\bar{x}))\,\chi_j(\bar{x})\right. \tag{33}$$

$$\left.\times\sum_{g=1}^{n}\nu_g(\bar{x})\,\Sigma_g^f(\bar{x})\,\phi_g^R(\bar{x},\omega) + \alpha_j(\bar{x})\sum_{i=1}^{m}\frac{\beta_i(\bar{x})\,\lambda_i(\bar{x})^2}{\lambda_i(\bar{x})^2 + \omega^2}\right.$$

$$\times \sum_{g=1}^{n} \nu_g(\bar{x})\, \Sigma_g^f(\bar{x})\, \phi_g^R(\bar{x},\omega) + \alpha_j(\bar{x}) \sum_{i=1}^{m} \frac{\beta_i(\bar{x})\, \lambda_i(\bar{x})\, \omega}{\lambda_i(\bar{x})^2 + \omega^2}$$

$$\times \sum_{g=1}^{n} \nu_g(\bar{x})\, \Sigma_g^f(\bar{x})\, \phi_g^I(\bar{x},\omega)] + \sum_{g=1}^{n} \Sigma_{g\to j}^s(\bar{x})\, \phi_g^R(\bar{x},\omega) + S_j^R(\bar{x})$$

$$= -\omega \left(\frac{1 + 3\, \Sigma_j^t(\bar{x})\, D_j(\bar{x})}{v_j(\bar{x})} \right) \phi_j^I(\bar{x},\omega) - \frac{3\, D_j(\bar{x})\, \omega^2}{v_j(\bar{x})^2}\, \phi_j^R(\bar{x},\omega)$$

$$D_j(\bar{x})\nabla^2\, \phi_j^I(\bar{x},\omega) - \Sigma_j^t(\bar{x})\, \phi_j^I(\bar{x},\omega) + \frac{1}{k}\,[(1 - \beta(\bar{x}))\, \chi_j(\bar{x}) \qquad (34)$$

$$\times \sum_{g=1}^{n} \nu_g(\bar{x})\, \Sigma_g^f(\bar{x})\, \phi_g^I(\bar{x},\omega) - \alpha_j(\bar{x}) \sum_{i=1}^{m} \frac{\beta_i(\bar{x})\, \lambda_i(\bar{x})\, \omega}{\lambda_i(\bar{x})^2 + \omega^2}$$

$$\times \sum_{g=1}^{n} \nu_g(\bar{x})\, \Sigma_g^f(\bar{x})\, \phi_g^R(\bar{x},\omega) + \alpha_j(\bar{x}) \sum_{i=1}^{m} \frac{\beta_i(\bar{x})\, \lambda_i(\bar{x})^2}{\lambda_i(\bar{x})^2 + \omega^2}$$

$$\times \sum_{g=1}^{n} \nu_g(\bar{x})\, \Sigma_g^f(\bar{x})\, \phi_g^I(\bar{x},\omega)] + \sum_{g=1}^{n} \Sigma_{g\to j}^s(\bar{x})\, \phi_g^I(\bar{x},\omega) + S_j^I(\bar{x})$$

$$= \omega \left(\frac{1 + 3\, \Sigma_j^t(\bar{x})\, D_j(\bar{x})}{v_j(\bar{x})} \right) \phi_j^R(\bar{x},\omega) - \frac{3\, D_j(\bar{x})\, \omega^2\, \phi_j^I(\bar{x})}{v_j(\bar{x})^2}$$

These are the equations to be solved, but their present form remains unwieldy for practical computation. Further simplification, without any additional loss of generality, can be realized if artificial defini-

tions are introduced for combinations of terms as follows

$$\Sigma_j^t(\bar{x},\omega) \equiv \Sigma_j^t(\bar{x}) - \frac{3\, D_j(\bar{x})\, \omega^2}{v_j(\bar{x})^2} \tag{35}$$

$$\Sigma^s_{g(R)\to j(R)}(\bar{x},\omega) \equiv \Sigma^s_{g(I)\to j(I)}(\bar{x},\omega) \equiv \frac{1}{k}\left(\chi_i(\bar{x})(1 - \beta(\bar{x})) + \alpha_j(\bar{x}) \right. \tag{36}$$

$$\left. \times \sum_{i=1}^{m} \frac{\beta_i(\bar{x})\, \lambda_i(\bar{x})^2}{\lambda_i(\bar{x})^2 + \omega^2} \right) \nu_g(\bar{x})\, \Sigma_g^f(\bar{x}) + \Sigma^s_{g\to j}(\bar{x})$$

$$\Sigma^s_{g(I)\to j(R)}(\bar{x},\omega) \equiv -\Sigma^s_{g(R)\to j(I)}(\bar{x},\omega) \equiv \frac{1}{k}\alpha_j(\bar{x}) \sum_{i=1}^{m} \frac{\beta_i(\bar{x})\, \lambda_i(\bar{x})\, \omega}{\lambda_i(\bar{x})^2 + \omega^2} \tag{37}$$

$$\times \nu_g(\bar{x})\, \Sigma_g^f(\bar{x}) + \omega \left(\frac{1 + 3\, \Sigma_j^t(\bar{x})\, D_j(\bar{x})}{v_j(\bar{x})} \right) \delta_{gj}$$

where

$$\delta_{gj} = 0 \text{ if } g \neq j$$
$$= 1 \text{ if } g = j$$

The term "kinetic" cross section will be used to apply to the cross sections defined by equations 35 through 37 because of their dependence upon frequency. Since the Φ's have two identifiers, g or j and R or I, it is convenient to identify the fictitious scattering cross section as, for example, $\Sigma^s_{g(R)\to j(R)}(\bar{x},\omega)$, meaning the scattering cross section

that transfers from group g, real component to group j, real component, etc.

With the above definitions, equations 33 and 34 become

$$D_j(\bar{x})\nabla^2 \phi_j^R(\bar{x},\omega) - \Sigma_j^t(\bar{x},\omega)\ \phi_j^R(\bar{x},\omega) + \sum_{g=1}^{n} \Sigma^s_{g(R)\rightarrow j(R)}(\bar{x},\omega)\ \phi_g^R(\bar{x},\omega) \quad (38)$$

$$+ \sum_{g=1}^{n} \Sigma^s_{g(I)\rightarrow j\ (R)}(\bar{x},\omega)\ \phi_g^I(\bar{x},\omega) + S_j^R(\bar{x}) = 0$$

and

$$D_j(\bar{x})\nabla^2 \phi_j^I(\bar{x},\omega) - \Sigma_j^t(\bar{x},\omega)\ \phi_j^I(\bar{x},\omega) + \sum_{g=1}^{n} \Sigma^s_{g(I)\rightarrow j(I)}(\bar{x},\omega)\ \phi_g^I(\bar{x},\omega) \quad (39)$$

$$+ \sum_{g=1}^{n} \Sigma^s_{g(R)\rightarrow j(I)}(\bar{x},\omega)\ \phi_g^R(\bar{x},\omega) + S_j^I(\bar{x}) = 0$$

With this notation, equations 38 and 39 appear to describe the situation of an external source in a nonmultiplying medium. The apparent nonmultiplying character results from the way terms were collected and the manner in which the fictitious scattering cross sections was defined. These equations provide for the possibility of coupling between any group (real or imaginary) and any other group (real or imaginary). This type of problem is readily solvable by existing statics techniques. Although the format of the problem is now similar to conventional statics problems, it should be emphasized at this point that equation 37 can generate a negative "cross section." Also, it is important to note that the solution

to equations 38 and 39 represents the real and quadrature components of the response of the fluctuating component of the neutron flux when the reactor is subjected to a sinusoidally varying external source. Either or both of the components can be negative.

Since part of the virtue in this formulation of the problem is to take advantage of existing statics codes as a method of solution, it is necessary to establish that the real and quadrature components of the amplitude of the fluctuating response satisfy the same boundary conditions as the true flux.

The boundary conditions to be satisfied by the flux, $\Phi_j(\bar{x}, t)$, are

$$\Phi_j(\bar{x}_s, t) = 0 \qquad \text{for } t \geq 0 \tag{40}$$

where $\bar{x}_s$ denotes the (extrapolated) surface of the reactor

$$\lim_{\epsilon \to 0} [\Phi_j(\bar{x}_{b-\epsilon}, t) = \Phi_j(\bar{x}_{b+\epsilon}, t)] \qquad \text{for } t \geq 0 \tag{41}$$

i.e., the flux is continuous across a boundary, b

$$\lim_{\epsilon \to 0} [D_j(\bar{x}_{b-\epsilon}) \nabla \Phi_j(\bar{x}_{b-\epsilon}, t) = D_j(\bar{x}_{b+\epsilon}) \nabla \Phi_j(\bar{x}_{b+\epsilon}, t)] \qquad \text{for } t \geq 0 \tag{42}$$

i.e., the current is continuous across a boundary.

Substitution of equation 6 into 40 through 42 (in view of the fact that the static component of the flux, by definition, must satisfy the above boundary conditions) gives

$$\delta\Phi(\bar{x}_s, t) = 0 \qquad \text{for } t \geq 0 \tag{43}$$

$$\lim_{\epsilon\to 0} [\delta\Phi_j(\bar{x}_{b-\epsilon}, t) = \delta\Phi_j(\bar{x}_{b+\epsilon}, t)] \qquad \text{for } t \geq 0 \tag{44}$$

$$\lim_{\epsilon\to 0} [D_j(\bar{x}_{b-\epsilon})\nabla\, \delta\Phi_j(\bar{x}_{b-\epsilon}, t) = D_j(\bar{x}_{b+\epsilon})\nabla\, \delta\Phi_j(\bar{x}_{b+\epsilon}, t)] \qquad \text{for } t \geq 0 \tag{45}$$

Use equation 17 to substitute for $\delta\Phi_j(\bar{x}, t)$, in equations 43 through 45. The result is

$$\underline{\Phi}_j(\bar{x}_s, \omega) = 0 \qquad \text{for } t \geq 0 \tag{46}$$

$$\lim_{\epsilon\to 0} [\underline{\Phi}_j(\bar{x}_{b-\epsilon}, \omega) = \underline{\Phi}_j(\bar{x}_{b+\epsilon}, \omega)] \qquad \text{for } t \geq 0 \tag{47}$$

$$\lim_{\epsilon\to 0} [D_j(\bar{x}_{b-\epsilon})\nabla\, \underline{\Phi}_j(\bar{x}_{b-\epsilon}, \omega) = D_j(\bar{x}_{b+\epsilon})\nabla\, \underline{\Phi}_j(\bar{x}_{b+\epsilon}, \omega)] \qquad \text{for } t \geq 0 \tag{48}$$

where $e^{i\omega t}$ has been cancelled in equations 47 and 48.

Use of equation 30 to substitute for $\underline{\Phi}_j(\bar{x}, \omega)$ in equations 46 through 48 as well as the following two theorems:

(i) if a complex number is zero, both the real and imaginary parts are zero

(ii) if two complex numbers are equal, the real and imaginary parts are equal,

gives

$$\phi_j^R(\bar{x}_s, \omega) = 0 \qquad \text{for } t \geq 0 \tag{49}$$

$$\phi_j^I(\bar{x}_s, \omega) = 0 \qquad \text{for } t \geq 0 \tag{50}$$

$$\lim_{\epsilon \to 0} [\phi_j^R(\bar{x}_{b-\epsilon}, \omega) = \phi_j^R(\bar{x}_{b+\epsilon}, \omega)] \qquad \text{for } t \geq 0 \tag{51}$$

$$\lim_{\epsilon \to 0} [\phi_j^I(\bar{x}_{b-\epsilon}, \omega) = \phi_j^I(\bar{x}_{b+\epsilon}, \omega)] \qquad \text{for } t \geq 0 \tag{52}$$

$$\lim_{\epsilon \to 0} [D_j(\bar{x}_{b-\epsilon}) \nabla \phi_j^R(\bar{x}_{b-\epsilon}, \omega) = D_j(\bar{x}_{b+\epsilon}) \nabla \phi_j^R(\bar{x}_{b+\epsilon}, \omega)] \qquad \text{for } t \geq 0 \tag{53}$$

$$\lim_{\epsilon \to 0} [D_j(\bar{x}_{b-\epsilon}) \nabla \phi_j^I(\bar{x}_{b-\epsilon}, \omega) = D_j(\bar{x}_{b+\epsilon}) \nabla \phi_j^I(\bar{x}_{b+\epsilon}, \omega)] \qquad \text{for } t \geq 0 \tag{54}$$

Thus, equations 49 through 54 establish that the real and quadrature components of the complex amplitude of the fluctuating component satisfy the same boundary conditions as the normal flux associated with the solution of conventional statics problems.

Interpretation of the results remains to be discussed. Substitution for $\underline{S}_j(\bar{x})$ from equation 31 into equation 16 gives

$$\delta S_i(\bar{x}, t) = [S_j^R(\bar{x}) + i\, S_j^I(\bar{x})]\, e^{i\omega t} \tag{55}$$

or

$$= S_j^o(\bar{x})\, e^{i(\omega t + \zeta)}$$

where

$$S_j^o(\bar{x}) = [S_j^R(\bar{x})^2 + S_j^I(\bar{x})^2]^{\frac{1}{2}} \tag{56}$$

and ζ is the angle for which $-\pi < \zeta \leq \pi$ and

$$\cos \zeta = \frac{S_j^R(\bar{x})}{S_j^o(\bar{x})} \quad , \quad \sin \zeta = \frac{S_j^I(\bar{x})}{S_j^o(\bar{x})}$$

Physically, S_j^o represents the amplitude of the disturbance and ζ represents the reference epoch angle. Since the phase of the input disturbance is arbitrary, it is convenient to choose $S_j^I(\overline{x}) \equiv 0$ which implies $\zeta \equiv 0$.

The response at any point, represented by equation 17, can be written using equation 30 as

$$\delta\Phi(\overline{x}, t) = [\phi_j^R(\overline{x}, \omega) + i\, \phi_j^I(\overline{x}, \omega)]\, e^{i\omega t} \tag{57}$$

or

$$= \phi_j^o(\overline{x}, \omega)\, e^{i(\omega t+\theta)}$$

where

$$\phi_j^o(\overline{x}, \omega) = [\phi_j^R(\overline{x}, \omega)^2 + \phi_j^I(\overline{x}, \omega)^2]^{\frac{1}{2}} \tag{58}$$

and θ is the angle for which $-2\pi < \theta \leq 0$ and

$$\cos\theta = \frac{\phi_j^R(\overline{x}, \omega)}{\phi_j^o(\overline{x}, \omega)} \quad , \quad \sin\theta = \frac{\phi_j^I(\overline{x}, \omega)}{\phi_j^o(\overline{x}, \omega)}$$

As before, the physical interpretation of $\phi_j^o(\overline{x}, \omega)$ is the amplitude of the response and by restricting $S_j^I(\overline{x}) \equiv 0$, θ represents the phase of the response with respect to the disturbance.

Conclusion

Starting with the multigroup, multiregion representation of the telegrapher's equation, the derivation has resulted in a set of coupled, linear, nonhomogeneous differential equations applicable to any stationary

fueled reactor which can be solved by conventional statics techniques. The solution of these equations provides the necessary relationships to calculate at any point the amplitude and phase of the neutron flux response when the reactor is subjected to a small periodic disturbance.

CHAPTER V

APPLICATION OF THEORY

For reference, Table 7 summarizes the numerical effort which evolved in establishing a computational method capable of solving one- and/or two-dimensional complex source problems. The details of each calculation, with the exception of number 5, will be discussed in this chapter. The EXTERMINATOR results which simulated the pile oscillator experiment on the GTRR will be described in Chapter VI.

Table 7. Summary of Computer Codes Used to Analyze the Complex Source Problems Applicable for the NORA Reactor and the GTRR

No.	Reactor	Code Used	Dimensions	Core Description	Cross Sections
1	NORA	CHARLIE	1	Homogenized	Hansson (Norway)
2	NORA	CRAM	1	Homogenized	Hansson (Norway)
3	GTRR	CRAM	2	Fuel and D_2O	THERMOS and COMBO
4	NORA	EXTERMINATOR	1	Homogenized	Hansson (Norway)
5	GTRR	EXTERMINATOR	2	Homogenized	THERMOS and COMBO

The derivation in the preceding chapter resulted in a system of equations, 38 and 39, whose solution describes the response of the neutron

flux when the reactor is subjected to a small periodic disturbance. This chapter will show how, with appropriate identification, the above mentioned equations can be solved with existing statics codes. Numerical results of one- and two-dimensional calculations will be given.

Experimental verification of numerical results obtained using the mathematical technique discussed in Chapter IV would add to the substance of this approach. For this reason, the following problems were solved in an attempt to predict the experimental results obtained from pile oscillator experiments. In these experiments, the reactor was subjected to a small, local, periodic disturbance, obtained by varying the neutron absorption at some particular location. The response to this disturbance was monitored at various other locations within the reactor. The details of the pile oscillator experiment performed on the GTRR are contained in Chapters II and III.

The manner in which the disturbance is simulated in the computations needs further elaboration. As mentioned previously in Chapter II, this disturbance is treated as equivalent to an external source whose strength varies periodically. Thus, the question to be answered is what value should be used for $\underline{S}_j(\bar{x})$ (Chapter IV, equation 16) or better still, what should be used for $S_j^R(\bar{x})$ and $S_j^I(\bar{x})$ (Chapter IV, equation 31). As pointed out in Chapter IV, it is convenient to set $S_j^I(\bar{x}) \equiv 0$. However, $S_j^R(\bar{x})$, the amplitude of the disturbance, remains to be assigned a value. Since the final formulation of the problem resulted in equations 38 and 39 which describe the situation of an external source in a nonmultiplying medium, the value of $S_j^R(\bar{x})$ is arbitrary because the equations are inhomogeneous. The real component of the external source has a value only in

the regions where the disturbance is present; in all other regions $S_j^R(\bar{x}) \equiv 0$. The remaining consideration is the energy dependence. As an example, consider a two-energy group analysis, fast and thermal. It is important that the ratio of the disturbance, i.e., absorption, in the fast group to the thermal group be maintained. If, as was the case in the experiments to be discussed, cadmium is used as the absorber, then the disturbance, i.e., absorption, of the fast neutrons can be considered negligible in comparison with the absorption of the thermal neutrons. Since the ratio of the fast absorption cross section to the thermal absorption cross section of cadmium is approximately 1 to 800 and the ratio of fast flux to thermal flux (at the oscillator) is approximately 1 to 10, the fast neutron absorptions are less than 0.02 percent of the thermal neutron absorptions. Thus, $S_{fast}^R(\bar{x}) \equiv 0$ everywhere. Now, $S_{thermal}^R(\bar{x})$ at a particular point or in one given mesh region is completely arbitrary. If, as was the case here, the cadmium of the pile oscillator extends into several mesh regions in the grid representation, then the ratios of the values of $S_{thermal}^R(\bar{x})$ should be the same as their static flux counterpart. This assumes no significant flux depression effects, which in the actual experiment was not the case. To be completely specific, in the mesh region having the highest static thermal flux value where the oscillator is to be located, $S_{thermal}^R(\bar{x})$ can be set equal to 1.0. In the adjacent mesh regions where the oscillator is to be represented, the appropriate number between zero and one should be used. The phase angle results do not depend upon the magnitude of $S_{thermal}^R(\bar{x})$ since the ratio of the resulting complex fluxes is maintained, yet the amplitude of the response for a particular frequency is directly dependent upon this value. Hence,

$S^{R}_{thermal}(\bar{x})$, once established, must remain fixed for all frequencies under consideration. Then the relationship between the amplitude values for various frequencies will be maintained. Therefore, the role of $\underline{S}_j(\bar{x})$ reduces to establishing the reference angle for the input disturbance and providing an arbitrary normalization constant.

Reactor Model and Parameter Identification

In all cases, the calculations performed were applicable to a two-group, multiregion, one- or two-dimensional reactor model. Modification of $\Sigma^{t}_{j}(\bar{x},\omega)$, as defined by equation 35 in Chapter IV, was made to account for the leakage in the third direction (which was not considered) by defining

$$\hat{\Sigma}^{t}_{j}(\bar{x},\omega) \equiv \Sigma^{t}_{j}(\bar{x},\omega) + D_j(\bar{x})(B^2_z)_j \tag{59}$$

based upon the assumption

$$D_j(\bar{x}) \frac{\partial^2 \phi^{R}_{j}(\bar{x},\omega)}{\partial z} = - D_j(\bar{x})(B^2_z)_j \, \phi^{R}_{j}(\bar{x},\omega) \tag{60}$$

for slab geometry in the third direction. The same identification was valid for the equation involving $\phi^{I}_{j}(\bar{x},\omega)$. The one-dimensional problem considered was a special case of the more general two-dimensional problem and did not require any further assumptions.

For the two-group problem, the following identification was made for convenience. It permitted one subscript to identify the "flux" rather

than a subscript (j) and a superscript (either R or I). The original two groups, 1 and 2, corresponded to fast and thermal energies, respectively.

$$\phi_1^R(\bar{x},\omega) \equiv \phi_1(\bar{x},\omega) \tag{61}$$

$$\phi_1^I(\bar{x},\omega) \equiv \phi_2(\bar{x},\omega)$$

$$\phi_2^R(\bar{x},\omega) \equiv \phi_3(\bar{x},\omega)$$

$$\phi_2^I(\bar{x},\omega) \equiv \phi_4(\bar{x},\omega)$$

Likewise

$$S_1^R(\bar{x}) \equiv S_1(\bar{x}) \tag{62}$$

$$S_1^I(\bar{x}) \equiv S_2(\bar{x})$$

$$S_2^R(\bar{x}) \equiv S_3(\bar{x})$$

$$S_2^I(\bar{x}) \equiv S_4(\bar{x})$$

Thus a two-energy group problem becomes a four-group complex flux problem as follows

group 1 = fast real component

group 2 = fast imaginary component

group 3 = thermal real component

group 4 = thermal imaginary component

With the above assumptions and identifications, equations 38 and 39, for

two-energy groups, become as follows

Equation for the fast real component

$$D_1(\bar{x})\nabla^2 \phi_1(\bar{x},\omega) - \hat{\Sigma}_1^t(\bar{x},\omega)\,\phi_1(\bar{x},\omega) + \sum_{g=1}^{4} \Sigma^s_{g\to 1}(\bar{x},\omega)\,\phi_g(\bar{x},\omega) \qquad (63)$$

$$+ S_1(\bar{x}) = 0$$

Equation for the fast imaginary component

$$D_1(\bar{x})\nabla^2 \phi_2(\bar{x},\omega) - \hat{\Sigma}_1^t(\bar{x},\omega)\,\phi_2(\bar{x},\omega) + \sum_{g=1}^{4} \Sigma^s_{g\to 2}(\bar{x},\omega)\,\phi_g(\bar{x},\omega) \qquad (64)$$

$$+ S_2(\bar{x}) = 0$$

Equation for the thermal real component

$$D_2(\bar{x})\nabla^2 \phi_3(\bar{x},\omega) - \hat{\Sigma}_2^t(\bar{x},\omega)\,\phi_3(\bar{x},\omega) + \sum_{g=1}^{4} \Sigma^s_{g\to 3}(\bar{x},\omega)\,\phi_g(\bar{x},\omega) \qquad (65)$$

$$+ S_3(\bar{x}) = 0$$

Equation for the thermal imaginary component

$$D_2(\bar{x})\nabla^2 \phi_4(\bar{x},\omega) - \hat{\Sigma}_2^t(\bar{x},\omega)\,\phi_4(\bar{x},\omega) + \sum_{g=1}^{4} \Sigma^s_{g\to 4}(\bar{x},\omega)\,\phi_g(\bar{x},\omega) \qquad (66)$$

$$+ S_4(\bar{x}) = 0$$

The following identifications were made using equations 35, 36, 37, and 59.

$$\hat{\Sigma}_1^t(\bar{x},\omega) = \Sigma_1^t(\bar{x}) - \frac{3\, D_1(\bar{x})\, \omega^2}{v_1(\bar{x})^2} + D_1(\bar{x})(B_z^2)_1 \tag{67}$$

$$\hat{\Sigma}_2^t(\bar{x},\omega) = \Sigma_2^t(\bar{x}) - \frac{3\, D_2(\bar{x})\, \omega^2}{v_2(\bar{x})^2} + D_2(\bar{x})(B_z^2)_2 \tag{68}$$

$$\Sigma_{1\to1}^s(\bar{x},\omega) = \frac{1}{k}\left(\chi_1(\bar{x})(1 - \beta(\bar{x})) + \alpha_1(\bar{x}) \sum_{i=1}^{m} \frac{\beta_i(\bar{x})\, \lambda_i(\bar{x})^2}{\lambda_i(\bar{x})^2 + \omega^2}\right) \tag{69}$$

$$\times\, \nu_1(\bar{x})\, \Sigma_1^f(\bar{x}) + \Sigma_{1\to1}^s(\bar{x})$$

$$\Sigma_{1\to2}^s(\bar{x},\omega) = -\frac{1}{k}\left(\alpha_1(\bar{x}) \sum_{i=1}^{m} \frac{\beta_i(\bar{x})\, \lambda_i(\bar{x})\, \omega}{\lambda_i(\bar{x})^2 + \omega^2}\right) \nu_1(\bar{x})\, \Sigma_1^f(\bar{x}) \tag{70}$$

$$- \omega\left(\frac{1 + 3\, \Sigma_1^t(\bar{x})\, D_1(\bar{x})}{v_1(\bar{x})}\right)$$

$$\Sigma_{1\to3}^s(\bar{x},\omega) = \frac{1}{k}\left(\chi_2(\bar{x})(1 - \beta(\bar{x})) + \alpha_2(\bar{x}) \sum_{i=1}^{m} \frac{\beta_i(\bar{x})\, \lambda_i(\bar{x})^2}{\lambda_i(\bar{x})^2 + \omega^2}\right) \tag{71}$$

$$\times\, \nu_1(\bar{x})\, \Sigma_1^f(\bar{x}) + \Sigma_{1\to2}^s(\bar{x})$$

$$\Sigma^{s}_{1\to 4}(\bar{x},\omega) = -\frac{1}{k}\left(\alpha_2(\bar{x})\sum_{i=1}^{m}\frac{\beta_i(\bar{x})\,\lambda_i(\bar{x})\,\omega}{\lambda_i(\bar{x})^2+\omega^2}\right)\nu_1(\bar{x})\,\Sigma^{f}_1(\bar{x}) \tag{72}$$

$$\Sigma^{s}_{2\to 1}(\bar{x},\omega) = \frac{1}{k}\left(\alpha_1(\bar{x})\sum_{i=1}^{m}\frac{\beta_i(\bar{x})\,\lambda_i(\bar{x})\,\omega}{\lambda_i(\bar{x})^2+\omega^2}\right)\nu_1(\bar{x})\,\Sigma^{f}_1(\bar{x}) \tag{73}$$

$$+\ \omega\left(\frac{1+3\,\Sigma^{t}_1(\bar{x})\,D_1(\bar{x})}{v_1(\bar{x})}\right)$$

$$\Sigma^{s}_{2\to 2}(\bar{x},\omega) = \frac{1}{k}\left(\chi_1(\bar{x})(1-\beta(\bar{x}))+\alpha_1(\bar{x})\sum_{i=1}^{m}\frac{\beta_i(\bar{x})\,\lambda_i(\bar{x})^2}{\lambda_i(\bar{x})^2+\omega^2}\right) \tag{74}$$

$$\times\ \nu_1(\bar{x})\,\Sigma^{f}_1(\bar{x}) + \Sigma^{s}_{1\to 1}(\bar{x})$$

$$\Sigma^{s}_{2\to 3}(\bar{x},\omega) = \frac{1}{k}\left(\alpha_2(\bar{x})\sum_{i=1}^{m}\frac{\beta_i(\bar{x})\,\lambda_i(\bar{x})\,\omega}{\lambda_i(\bar{x})^2+\omega^2}\right)\nu_1(\bar{x})\,\Sigma^{f}_1(\bar{x}) \tag{75}$$

$$\Sigma^{s}_{2\to 4}(\bar{x},\omega) = \frac{1}{k}\left(\chi_2(\bar{x})(1-\beta(\bar{x}))+\alpha_2(\bar{x})\sum_{i=1}^{m}\frac{\beta_i(\bar{x})\,\lambda_i(\bar{x})^2}{\lambda_i(\bar{x})^2+\omega^2}\right) \tag{76}$$

$$\times\ \nu_1(\bar{x})\,\Sigma^{f}_1(\bar{x}) + \Sigma^{s}_{1\to 2}(\bar{x})$$

$$\Sigma^{s}_{3\to 1}(\bar{x},\omega) = \frac{1}{k}\left(\chi_1(\bar{x})(1-\beta(\bar{x}))+\alpha_1(\bar{x})\sum_{i=1}^{m}\frac{\beta_i(\bar{x})\,\lambda_i(\bar{x})^2}{\lambda_i(\bar{x})^2+\omega^2}\right) \tag{77}$$

$$\times\ \nu_2(\bar{x})\,\Sigma^{f}_2(\bar{x}) + \Sigma^{s}_{2\to 1}(\bar{x})$$

$$\Sigma^{s}_{3\to2}(\bar{x},\omega) = -\frac{1}{k}\left(\alpha_1(\bar{x}) \sum_{i=1}^{m} \frac{\beta_i(\bar{x})\,\lambda_i(\bar{x})\,\omega}{\lambda_i(\bar{x})^2 + \omega^2}\right) \nu_2(\bar{x})\,\Sigma^{f}_{2}(\bar{x}) \tag{78}$$

$$\Sigma^{s}_{3\to3}(\bar{x},\omega) = \frac{1}{k}\left(\chi_2(\bar{x})(1 - \beta(\bar{x})) + \alpha_2(\bar{x}) \sum_{i=1}^{m} \frac{\beta_i(\bar{x})\,\lambda_i(\bar{x})^2}{\lambda_i(\bar{x})^2 + \omega^2}\right) \tag{79}$$

$$\times\, \nu_2(\bar{x})\,\Sigma^{f}_{2}(\bar{x}) + \Sigma^{s}_{2\to2}(\bar{x})$$

$$\Sigma^{s}_{3\to4}(\bar{x},\omega) = -\frac{1}{k}\left(\alpha_2(\bar{x}) \sum_{i=1}^{m} \frac{\beta_i(\bar{x})\,\lambda_i(\bar{x})\,\omega}{\lambda_i(\bar{x})^2 + \omega^2}\right) \nu_2(\bar{x})\,\Sigma^{f}_{2}(\bar{x}) \tag{80}$$

$$-\,\omega\left(\frac{1 + 3\,\Sigma^{t}_{2}(\bar{x})\,D_2(\bar{x})}{v_2(\bar{x})}\right)$$

$$\Sigma^{s}_{4\to1}(\bar{x},\omega) = \frac{1}{k}\left(\alpha_1(\bar{x}) \sum_{i=1}^{m} \frac{\beta_i(\bar{x})\,\lambda_i(\bar{x})\,\omega}{\lambda_i(\bar{x})^2 + \omega^2}\right) \nu_2(\bar{x})\,\Sigma^{f}_{2}(\bar{x}) \tag{81}$$

$$\Sigma^{s}_{4\to2}(\bar{x},\omega) = \frac{1}{k}\left(\chi_1(\bar{x})(1 - \beta(\bar{x})) + \alpha_1(\bar{x}) \sum_{i=1}^{m} \frac{\beta_i(\bar{x})\,\lambda_i(\bar{x})^2}{\lambda_i(\bar{x})^2 + \omega^2}\right) \tag{82}$$

$$\times\, \nu_2(\bar{x})\,\Sigma^{f}_{2}(\bar{x}) + \Sigma^{s}_{2\to1}(\bar{x})$$

$$\Sigma^{s}_{4\to3}(\bar{x},\omega) = \frac{1}{k}\left(\alpha_2(\bar{x}) \sum_{i=1}^{m} \frac{\beta_i(\bar{x})\,\lambda_i(\bar{x})\,\omega}{\lambda_i(\bar{x})^2 + \omega^2}\right) \nu_2(\bar{x})\,\Sigma^{f}_{2}(\bar{x}) \tag{83}$$

$$+\,\omega\left(\frac{1 + 3\,\Sigma^{t}_{2}(\bar{x})\,D_2(\bar{x})}{v_2(\bar{x})}\right)$$

$$\Sigma^{s}_{4\rightarrow 4}(\bar{x},\omega) = \frac{1}{k}\left(\chi_2(\bar{x})(1 - \beta(\bar{x})) + \alpha_2(\bar{x}) \sum_{i=1}^{m} \frac{\beta_i(\bar{x})\ \lambda_i(\bar{x})^2}{\lambda_i(\bar{x})^2 + \omega^2} \right) \qquad (84)$$

$$\times\ \nu_2(\bar{x})\ \Sigma^{f}_{2}(\bar{x}) + \Sigma^{s}_{2\rightarrow 2}(\bar{x})$$

Equations 63 through 84 provide the relationships necessary for formulating a two-group complex source problem. Appendix B contains a discussion and listing of the program KISEC, which computes the "kinetic" cross sections (equations 67 through 84) needed as input to solve the two-group, multiregion complex source problem described by equations 63 through 66.

One-Dimensional Analysis of the NORA Reactor Using CHARLIE and CRAM

Initial investigation using the approach just described was applied to a one-dimensional model of the NORA reactor. A description of this heavy-water moderated, enriched uranium critical assembly located in Kjeller, Norway, is contained in references 31 and 32 along with the details of the experiment referred to in the following discussion. This experiment was chosen because it provided experimental evidence of the space-dependent response of the NORA reactor to a pile oscillator. In particular, one set of experimental results was for the oscillator located near the center of the core. This configuration, assuming cylindrical symmetry and accounting for axial leakage by the term DB_z^2, as described earlier (equation 59), was amenable to a one-dimensional analysis.

The equations were programmed for solution on the B-5500 computer using a finite difference approximation for the space derivatives. A

maximum of 25 variable radial mesh spaces was allowed. The details of this program (CHARLIE) are described in reference 33. The size of the computer problem should be noted. With four equations applicable at each space point, the final matrix was 104 by 104. The solution to the system of difference equations was obtained by direct matrix inversion and also by the method of conjugate gradients.[34] Both methods yielded essentially the same results.

The "static" two-group constants (furnished by Hansson[35]), which were used in the computations for the NORA reactor, are listed in Table 8. The delayed neutron constants[32] for the NORA reactor are given in Table 9.

Table 8. "Static" Two-Group Constants for the NORA Reactor[35]

	D_1 (cm)	D_2 (cm)	Σ_1^t (cm^{-1})	Σ_2^t (cm^{-1})	$\nu_1 \Sigma_1^f$ (cm^{-1})	$\nu_2 \Sigma_2^f$ (cm^{-1})	$\Sigma_{1\to2}^s$ (cm^{-1})
Core	1.29197	0.81796	0.00991	0.00365	0.0	0.00556	0.00968
D_2O Reflector	1.305	0.82550	0.01090	0.00011	0.0	0.0	0.01090
Graphite Reflector	1.192	1.05	0.00282	0.00083	0.0	0.0	0.00282

$\bar{v}_1 = 2.0 \times 10^6$ cm/sec

$\bar{v}_2 = 2.2 \times 10^5$ cm/sec

Table 9. Delayed Neutron Constants for the NORA Reactor[32]

i	$\beta_i \times 10^{-5}$	λ_i sec^{-1}
1	24.8	0.0127
2	140.2	0.0317
3	124.5	0.115
4	270.1	0.311
5	86.8	1.40
6	18.2	3.87
7	48.2	0.278
8	15.1	0.0169
9	5.2	0.0049
10	2.5	0.00152
11	1.5	0.000427
12	1.7	0.000116
13	0.2	0.000044
14	0.07	0.0000037

$\beta_{total} = 0.0073907$

It was assumed that all neutrons (i.e., prompt and delayed) were born in the fast group.

Thus

$$\chi_1(\bar{x}) \equiv 1 \qquad \alpha_1(\bar{x}) \equiv 1$$

$$\chi_2(\bar{x}) \equiv 0 \qquad \alpha_2(\bar{x}) \equiv 0$$

The axial buckling, B_z^2 (assumed energy independent), was determined by a subroutine of the program CHARLIE. CHARLIE performed a search to find the B_z^2 that would describe a critical reactor. Searching for the value of B_z^2 to make the reactor mathematically critical is an alternate approach to specifying the value of B_z^2 and adjusting the value of the eigenvalue (k) to make the reactor critical. The effect on the final analysis should be slight. No cases were run to investigate the dependence of the answers on the approach taken. The value found for B_z^2 was 5.536047×10^{-4} cm^{-2}. This value of the buckling implies an extrapolated height of 133.52 cm. The measured extrapolated height reported in reference 32 was 132.85 cm. Results of the calculations performed using CHARLIE are shown in Figures 19 and 20. The agreement between the computed and experimental values was indeed good.

One of the primary goals of this research was to establish a technique which could apply to two-dimensional problems. This was accomplished as set forth by equations 38 and 39 of the preceding chapter. Having obtained the degree of success as shown in Figures 19 and 20 for the one-dimensional calculation, extension to two-dimensional calculations was highly desirable. For an existing statics code to be able to solve the

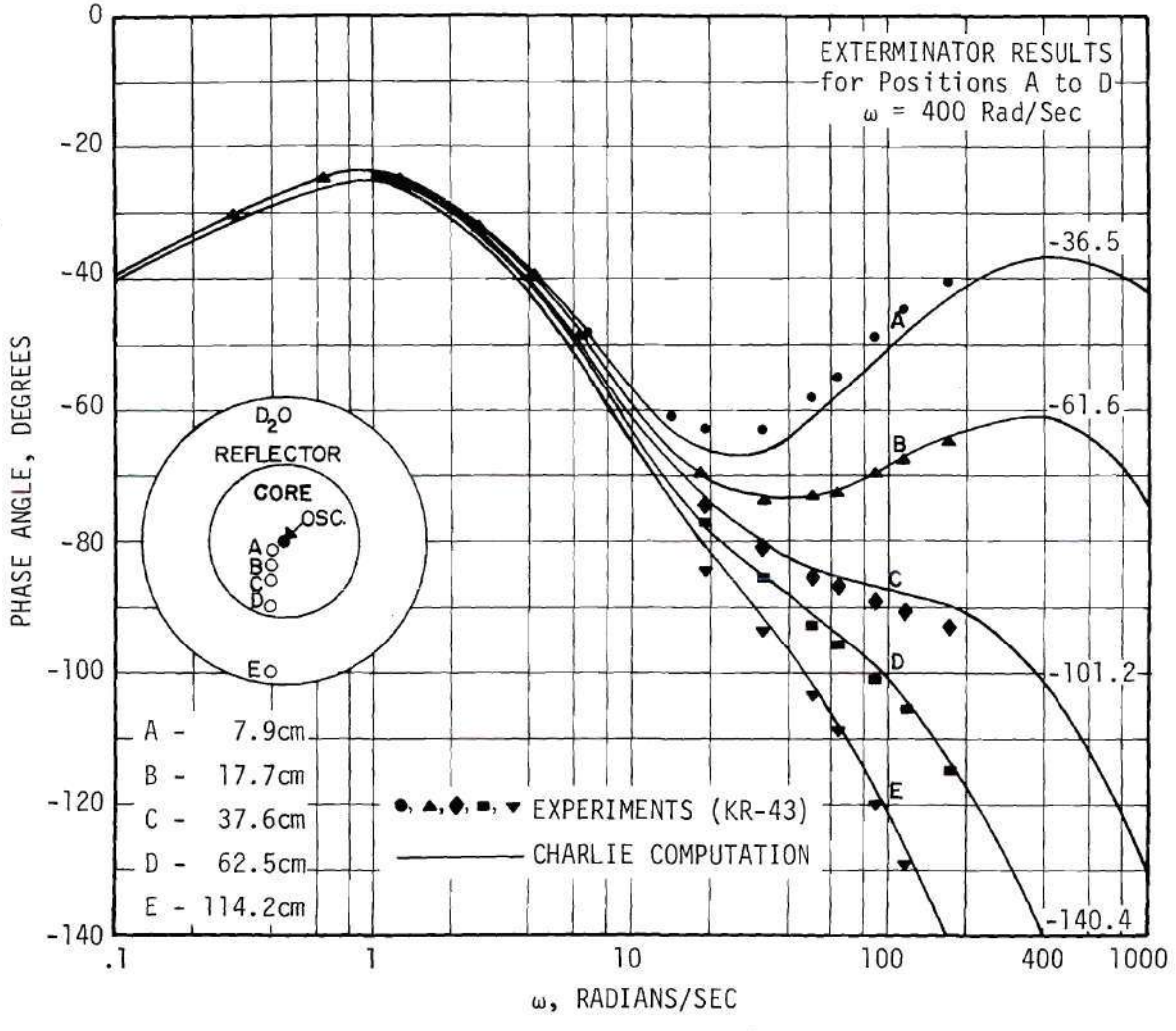

Figure 19. Experimental Phase Angle Results versus Frequency Compared with Digital Computations from CHARLIE and EXTERMINATOR for the NORA Reactor

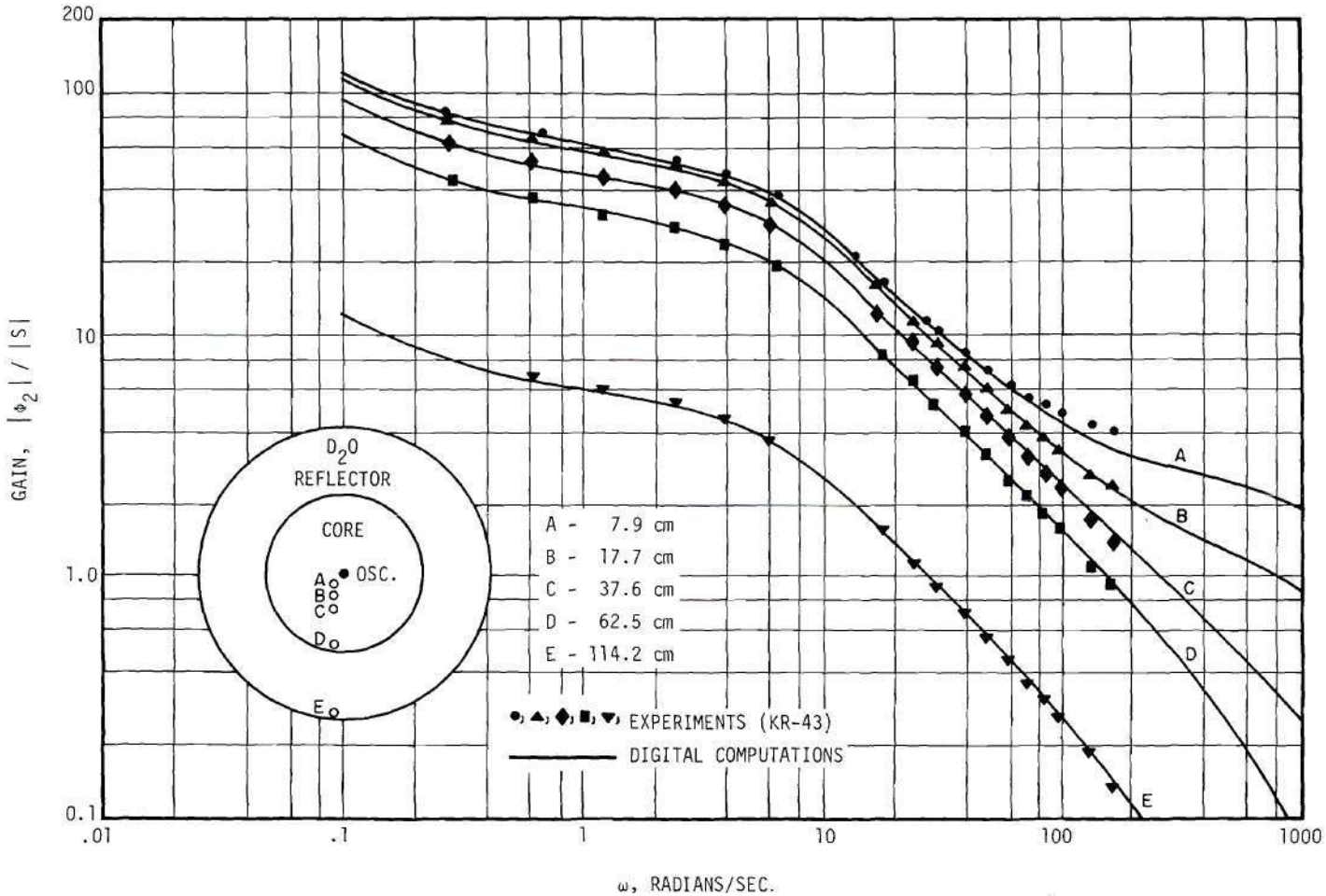

Figure 20. Experimental Gain Results versus Frequency Compared with Digital Computations from CRAM for the NORA Reactor

problem as formulated by equations 63 through 66, the following features had to be present in the code:

1. Allowance for an external source
2. Allowance for scattering from any group to any other group
3. Tolerance for negative values of the flux.

The CRAM code,[36] a multigroup, multiregion, one- or two-dimensional diffusion code, possesses all of these features. To verify the operation of the code and as a check on the previous program, the NORA reactor pile oscillator experiment was again analyzed using the same data previously given. Results of the calculations are shown in Figures 21 and 22. Over the experimental range, the results were in good agreement. However, slow convergence[37] was experienced throughout the entire range. For frequencies greater than 320 radians per second, CRAM did not converge. At low frequencies (less than 0.1 radian/sec), the results of CRAM (Figure 21) were indicative of a subcritical system.[38] This could be explained by the fact that the value of the critical buckling determined by CHARLIE was used instead of determining the critical buckling from the CRAM code, which should have been done. Two further sets of computations were performed to investigate the effect of reactivity. The previous calculations were repeated with CHARLIE and CRAM for the subcritical case $k_{eff} = 0.9977$ (extrapolated height 132.52 cm) and for the supercritical case, $k_{eff} = 1.0035$ (extrapolated height 134.52 cm). The value of k_{eff} was determined by CRAM when the buckling associated with the height was used as an input number for a conventional statics problem. The CRAM results are shown for a particular location in Figures 21 and 22. Figures 23 and 24 show the results from CHARLIE for one selected reactor position. The behavior

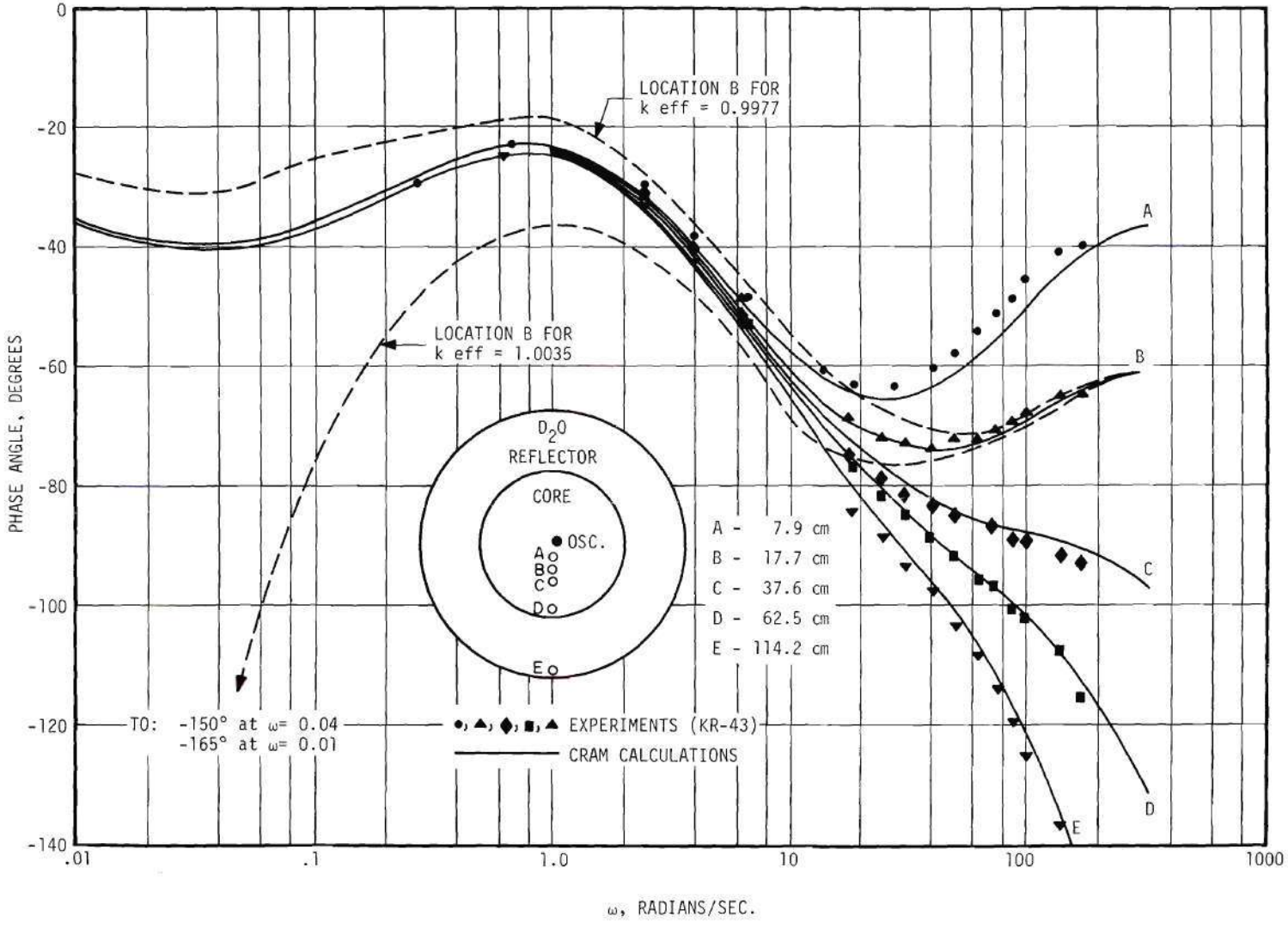

Figure 21. Experimental Phase Angle Results versus Frequency Compared with Digital Computations from CRAM for the NORA Reactor

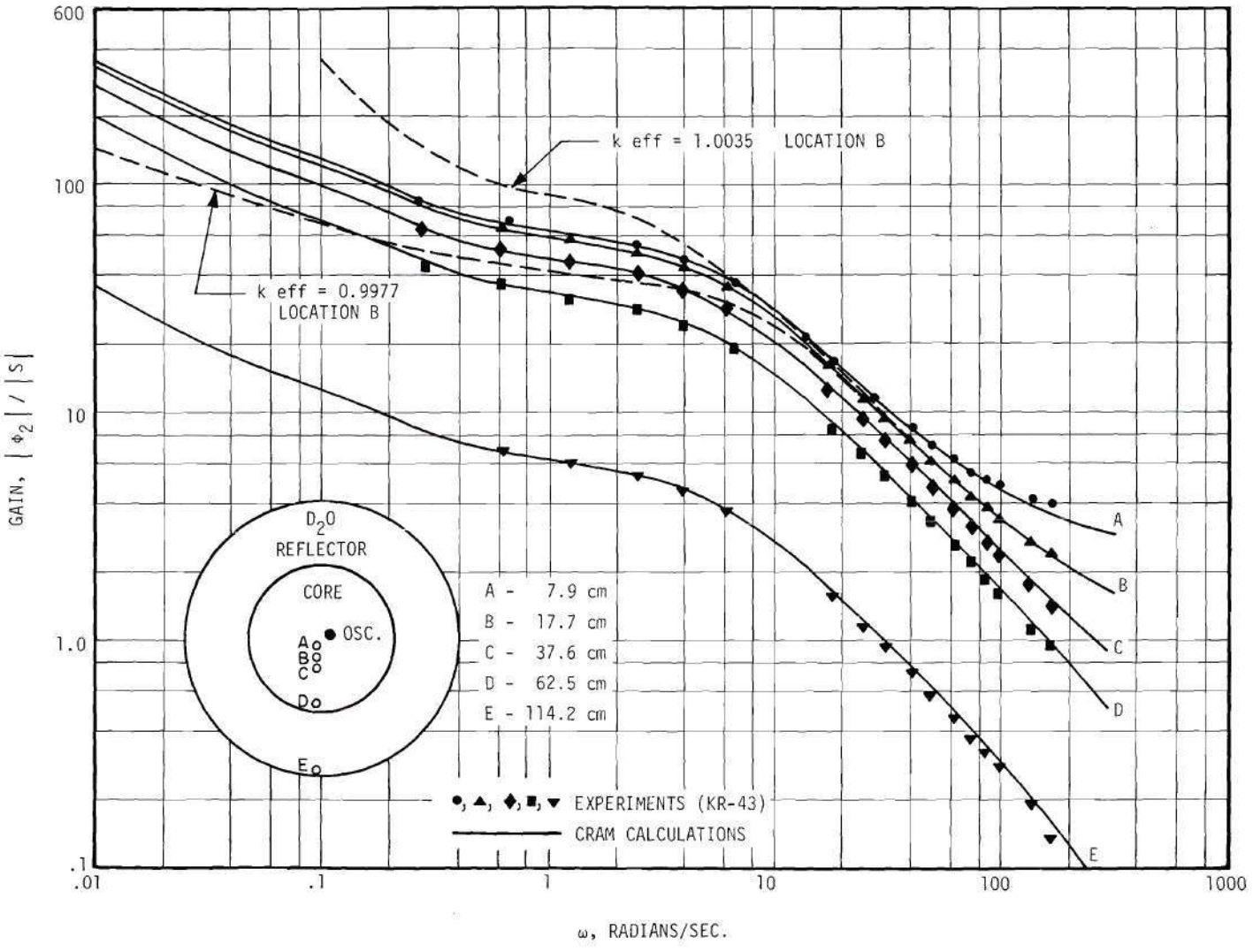

Figure 22. Experimental Gain Results versus Frequency Compared with Digital Computations from CRAM for the NORA Reactor

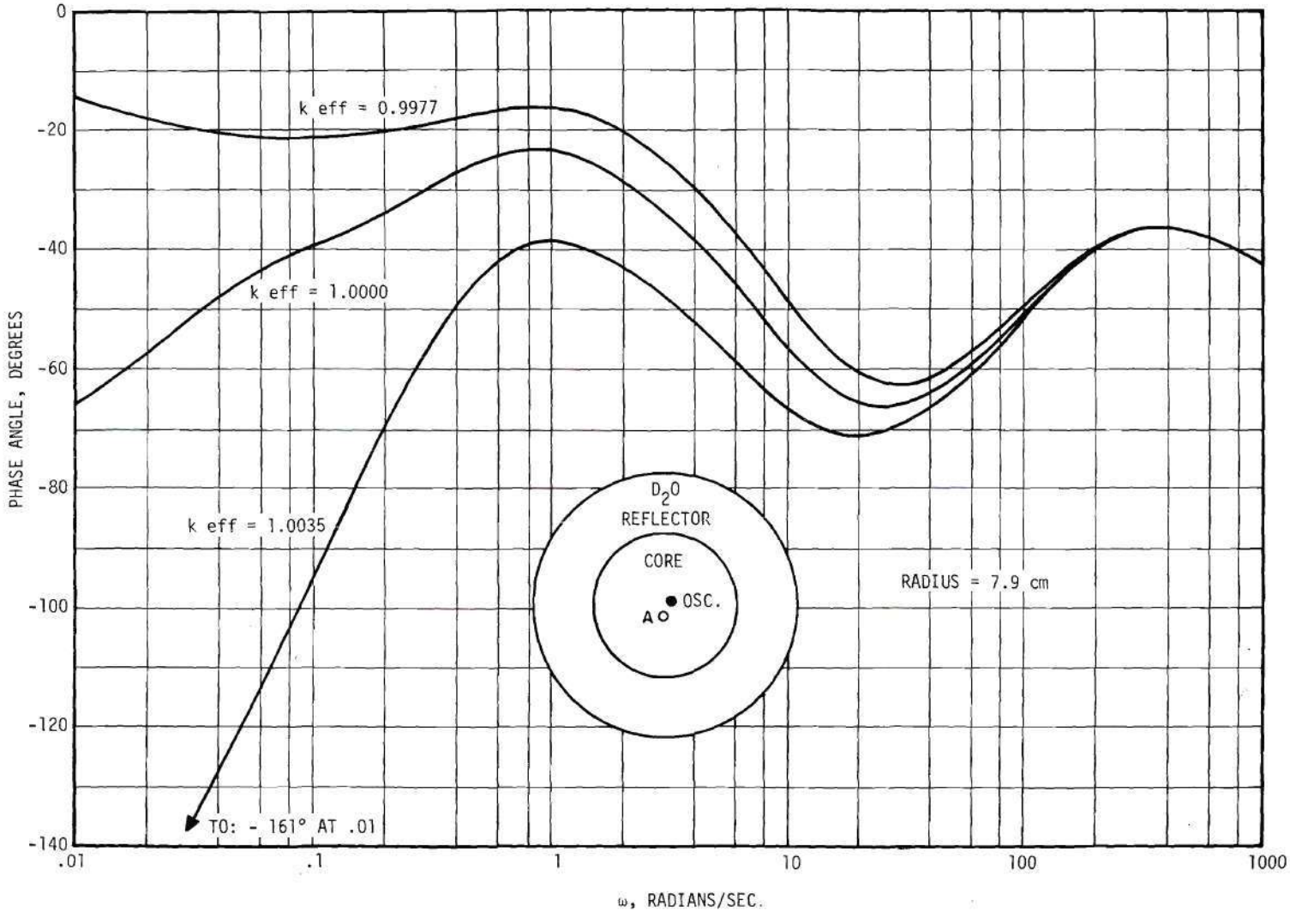

Figure 23. Effect of Reactivity on Computed Phase Shift for the NORA Reactor from CHARLIE

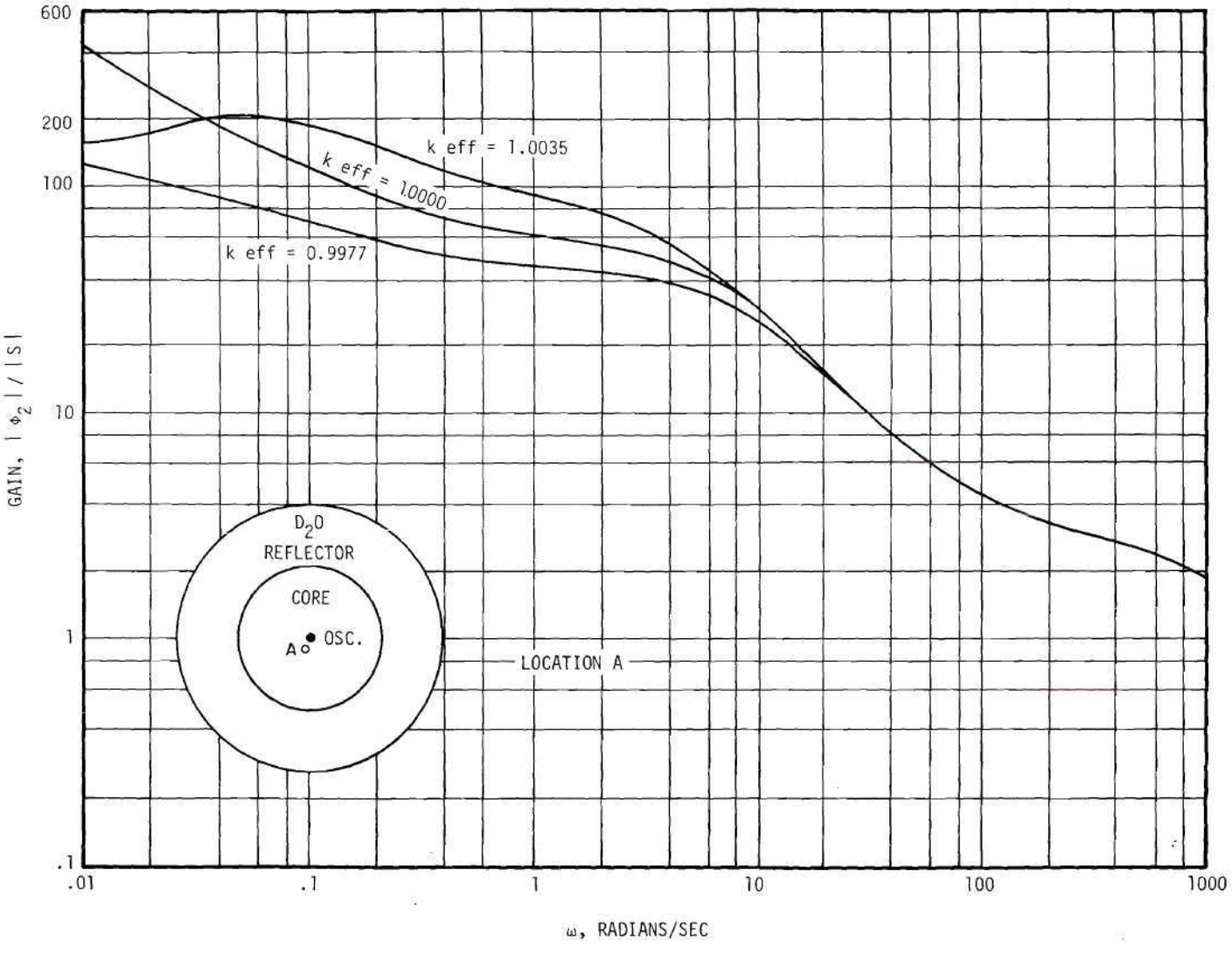

Figure 24. Effect of Reactivity on Computed Gain for the NORA Reactor from CHARLIE

in the gain curve exhibited by the results of CHARLIE was consistent with the results shown in reference 39. The discrepancy in the general shape of the gain curves at low frequencies as determined by CRAM and CHARLIE is an anomaly for which no explanation is apparent.

Two-Dimensional Analysis of the GTRR Using CRAM

Initial two-dimensional calculations[40] were performed using CRAM. From the experience gained in analyzing the NORA reactor, convergence problems were anticipated. However, at the time of these calculations, CRAM was the only code available which was potentially capable of performing an analysis of this type.

The GTRR was selected as the reactor to be analyzed. The oscillator, as shown in Figure 25, was located off the core center line, thus requiring a two-dimensional mathematical model for description. However, the removal cross section used in the mathematical model was not correct for the GTRR. This circumstance, coupled with the lack of definitive convergence, permits only a qualitative discussion of the numerical results. Nevertheless, some of the results are worthy of comment and further discussion.

The grid used to describe the core mid-plane of the reactor is shown in Figure 25. Within the core region, a three-inch by three-inch smeared fuel element was represented explicitly. The smaller grid spacing (both vertically and horizontally) centered about the oscillator was desirable since the steepest gradient in gain and phase shift was anticipated in the region surrounding the disturbance.

Figure 26 shows the static flux distribution for the thermal and

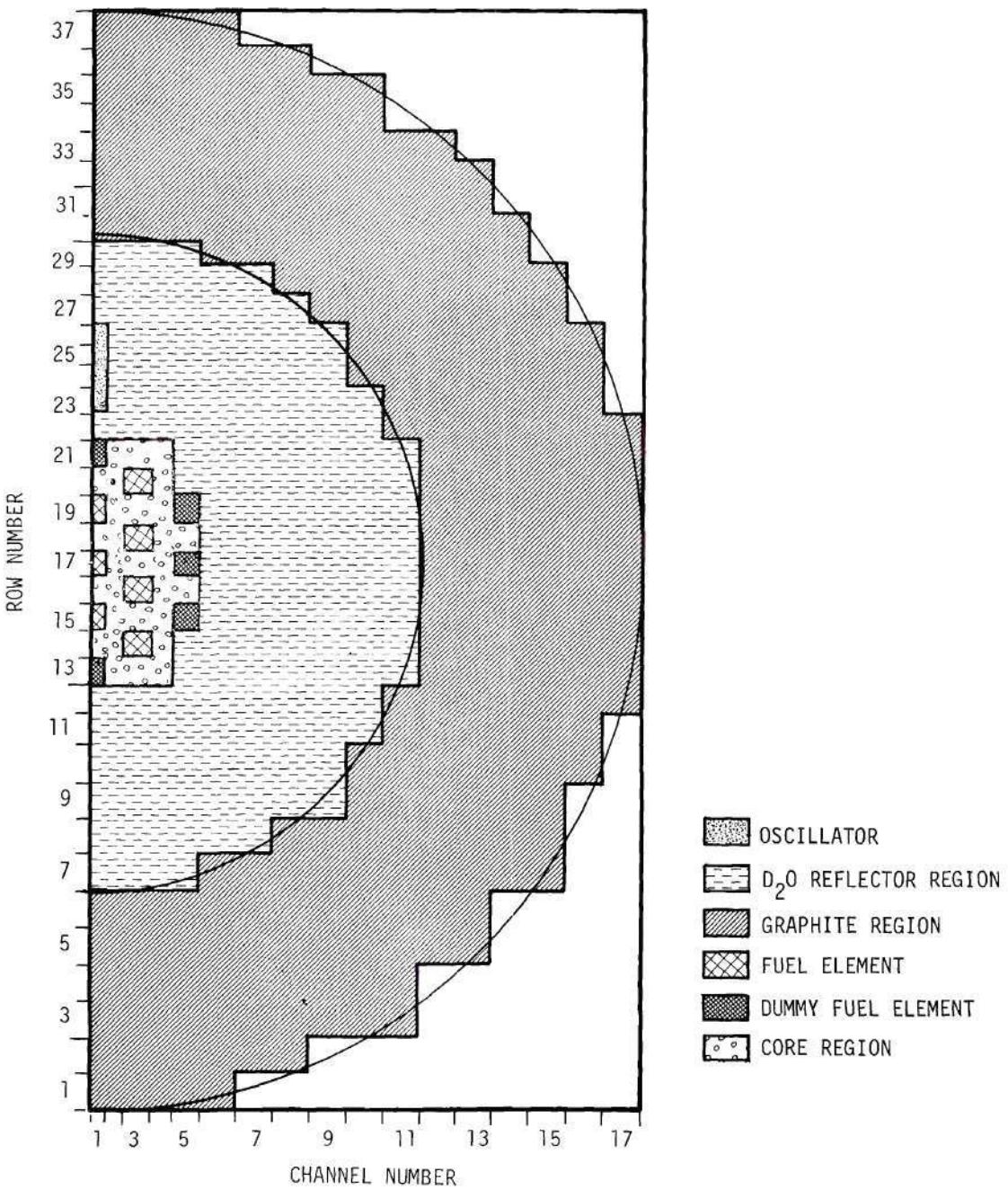

Figure 25. Two-Dimensional Core Grid Representation of GTRR for CRAM Computer Description

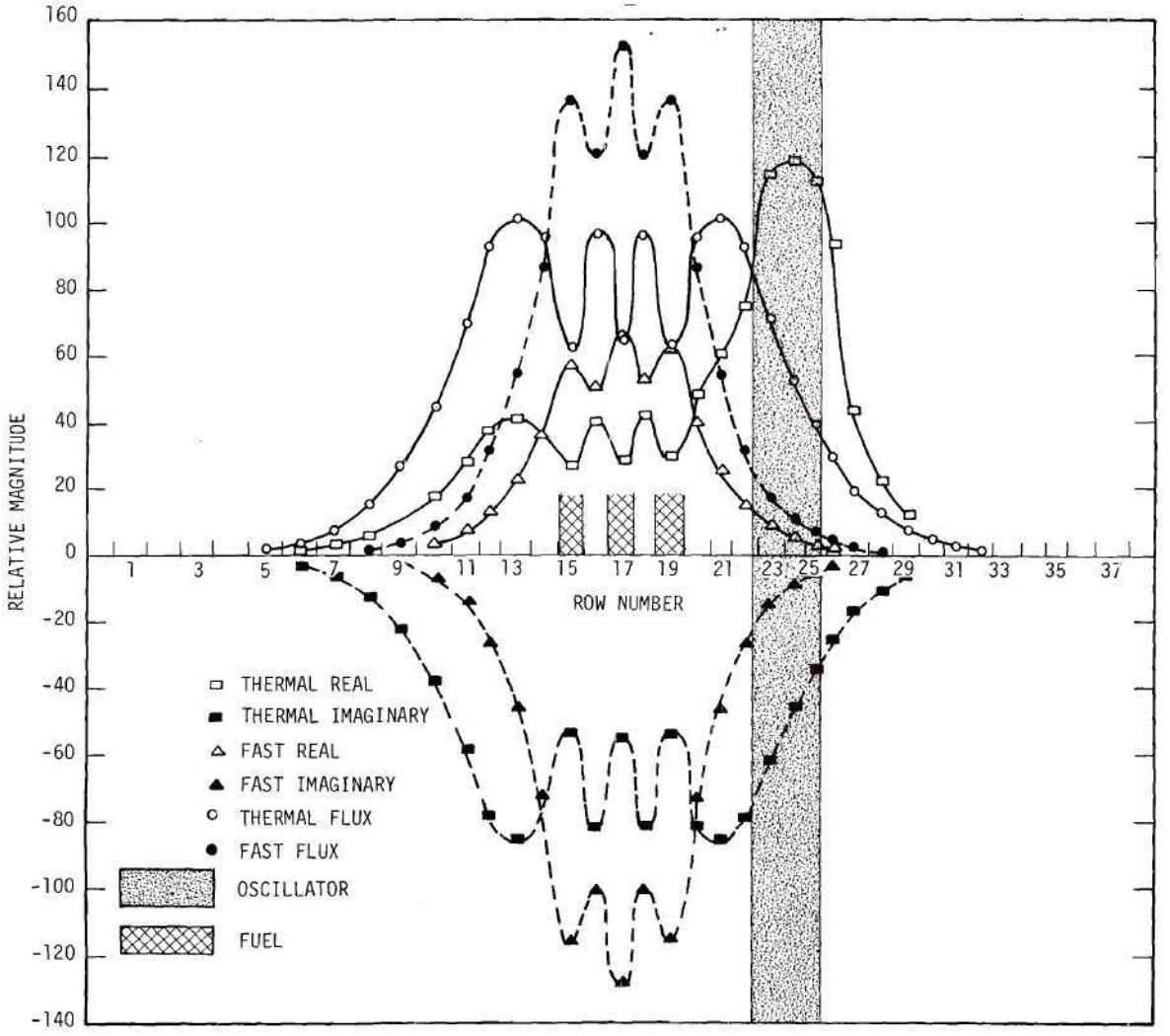

Figure 26. CRAM Results Along Mesh Channel One for the GTRR Static Flux Distribution and the Complex Components of the Thermal and Fast Flux Amplitudes for Input Disturbance Frequency of 20 Radians Per Second

fast fluxes. In addition (for the frequency of 20 radians per second), the complex components of the thermal and fast flux amplitudes are also shown. For this particular frequency, the real components of the respective fluxes have essentially the same shape as their static counterpart. This is not true in general, since for higher frequencies the phase shifts exceed 90 degrees and one or both components must change sign. (Figure 27 shows the static flux distribution for the thermal and fast fluxes using a mesh twice as fine as for Figure 26.)

Results of an analysis of this type provided the gain and phase at the mid-point of each mesh square for the frequency under consideration. The gain and phase are shown in Figures 28 and 29 for selected reactor locations. Since the solution for a given frequency provides the phase for each grid square, it is possible to construct lines of constant phase shift over the entire grid of the reactor. Such a map is shown in Figure 30 for a frequency of 20 radians per second. For ease of interpretation, the figure shows areas of increasing phase shift in five degree increments.

Further information was obtained from a graph of phase shift versus position for a given mesh channel and a particular frequency. The family of curves which resulted by plotting this information for various frequencies is shown in Figure 31. The flat portion of the curve inside the core and in the reflector region opposite the disturbance shows where the response to the disturbance was relatively space-independent. The dynamic effect of the core is evidenced by the rapid change of phase between the oscillator and the core.

It is of interest that, although the complex components of the

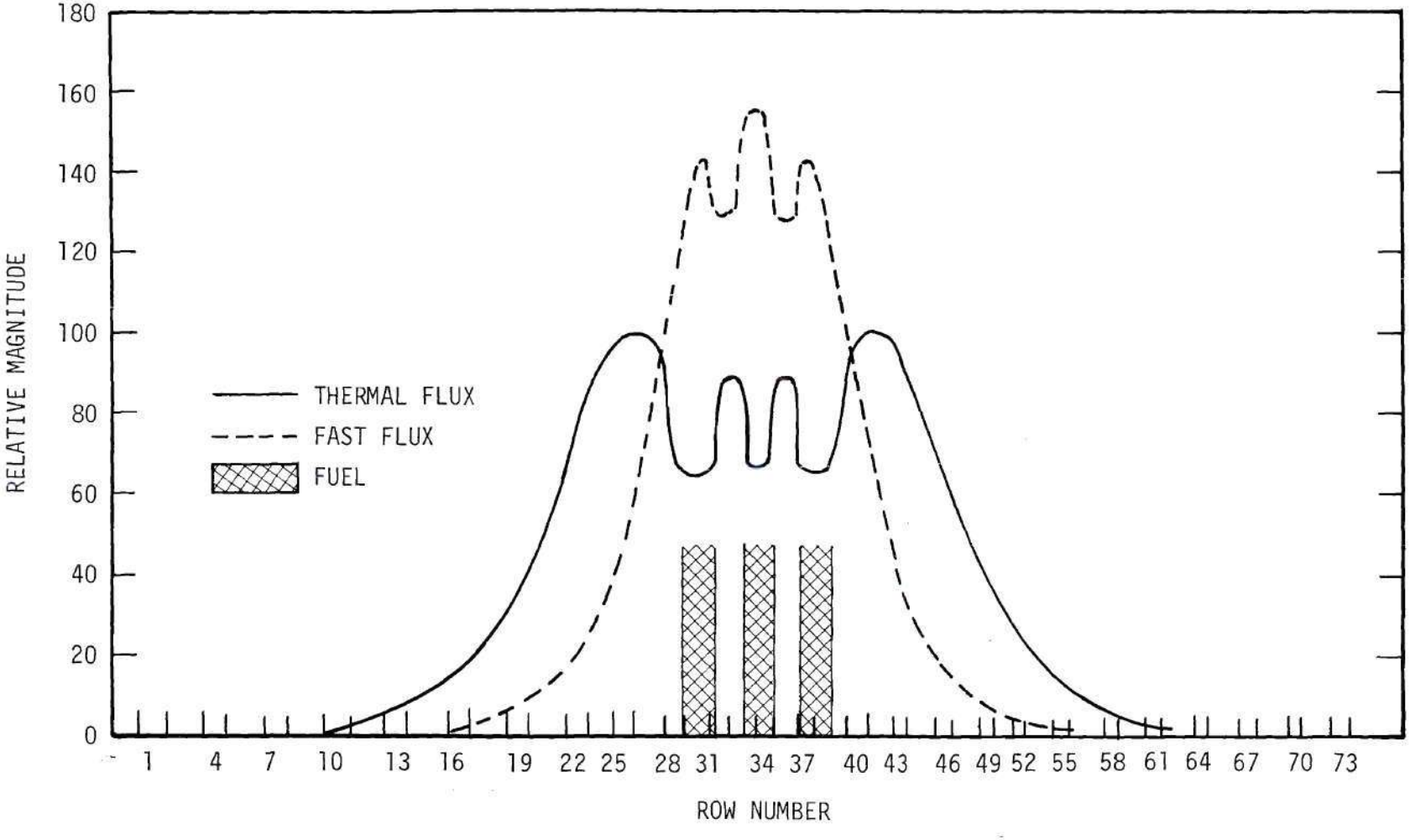

Figure 27. CRAM Results Along Mesh Channel One for the GTRR Fast and Thermal Static Flux Distribution with Refined Mesh Spacing

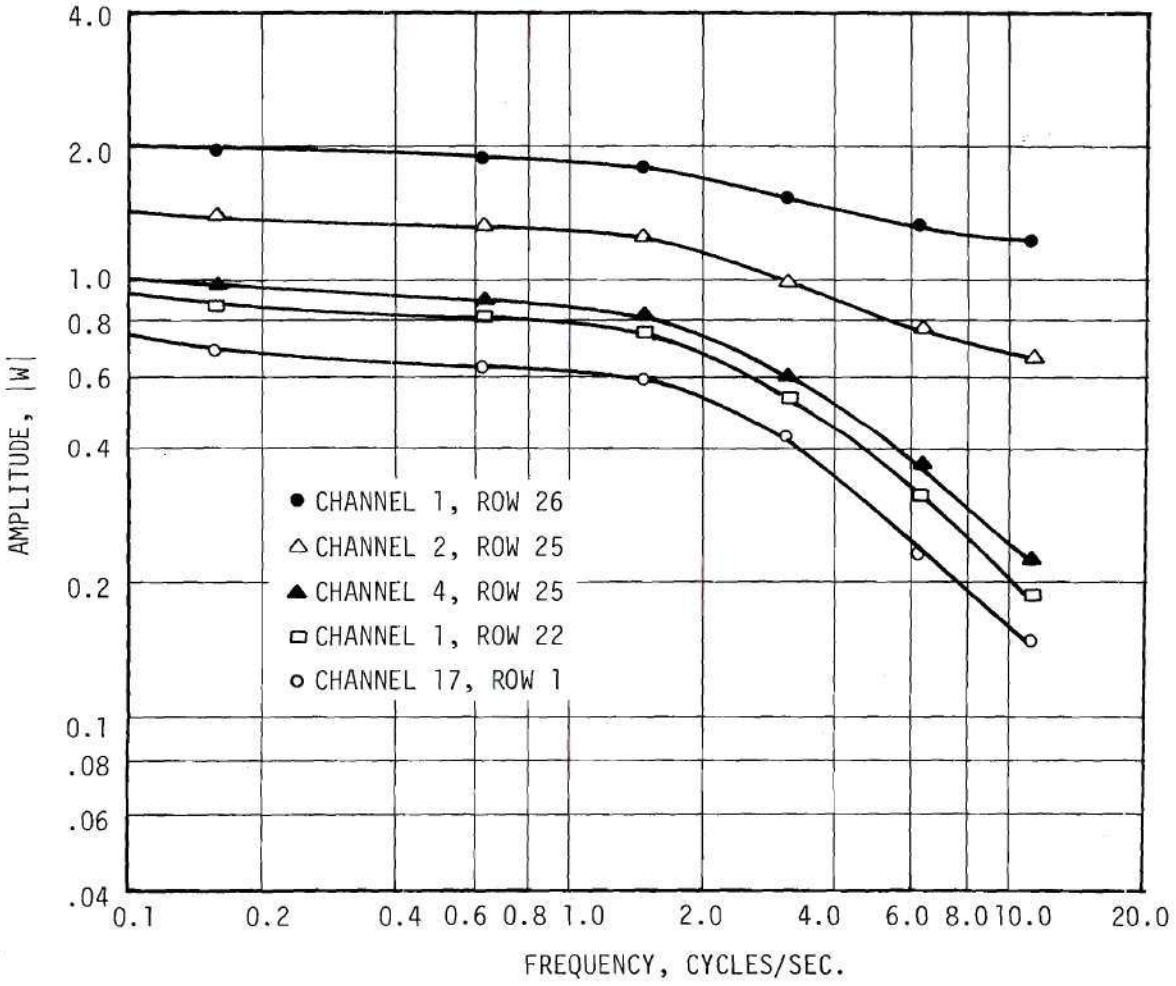

Figure 28. CRAM Results for the Amplitude of the Zero-Power Reactor Source Transfer Function versus Frequency for Various GTRR Locations

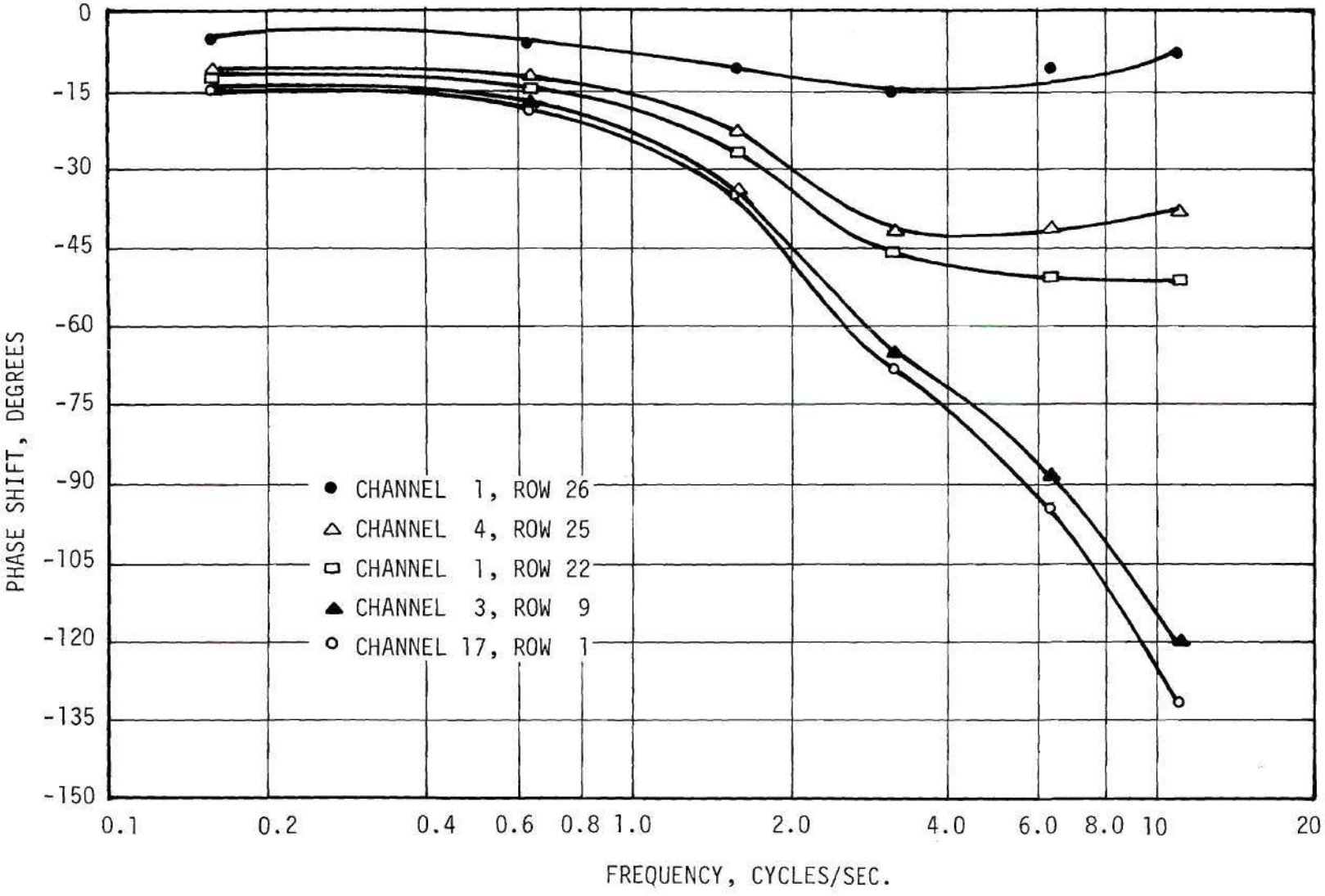

Figure 29. CRAM Results for the Phase Angle of the Zero-Power Reactor Source Transfer Function versus Frequency for Various GTRR Locations

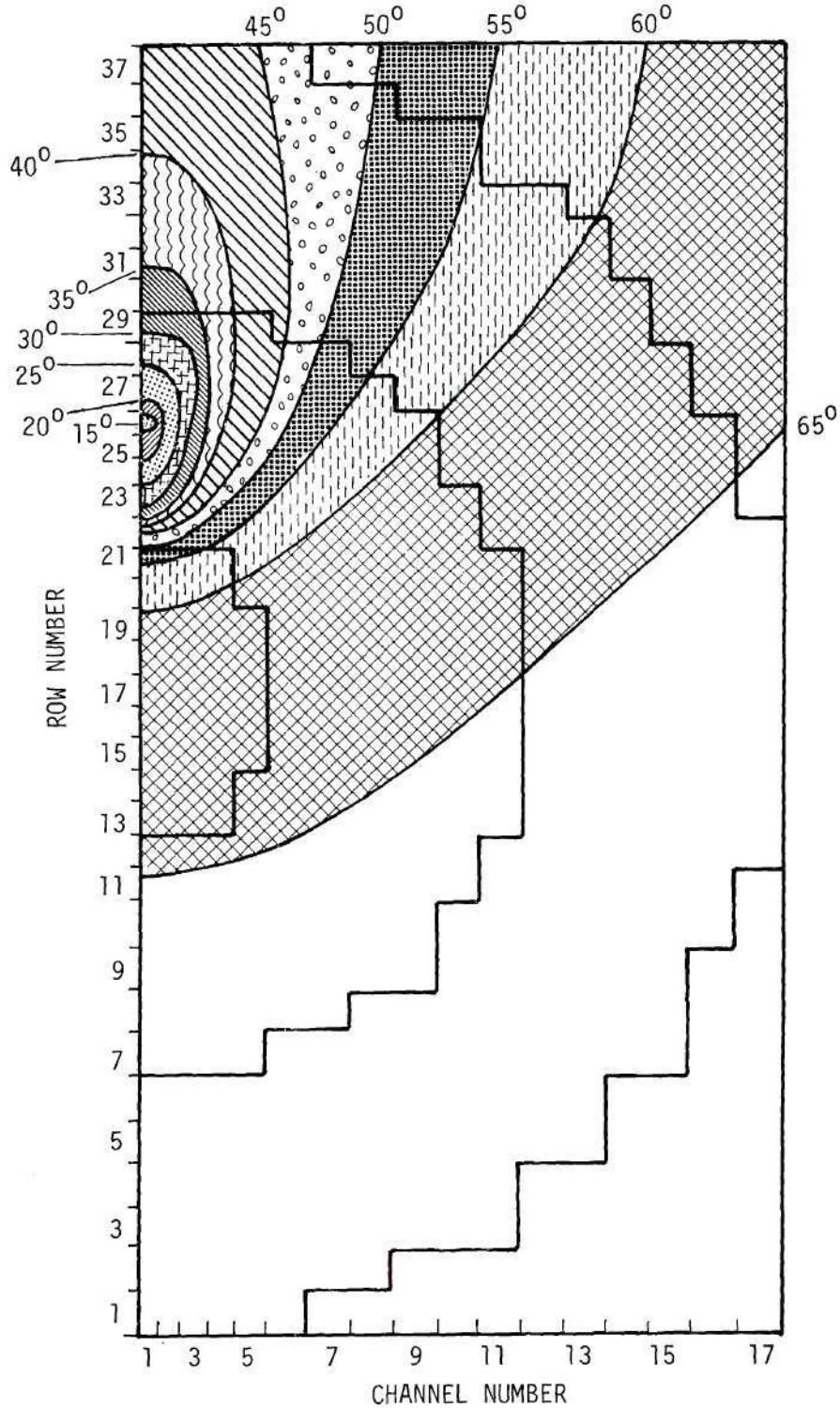

Figure 30. GTRR -- CRAM Results for the Space-Dependent Phase Response of the Neutron Flux for Input Disturbance Frequency of 20 Radians Per Second

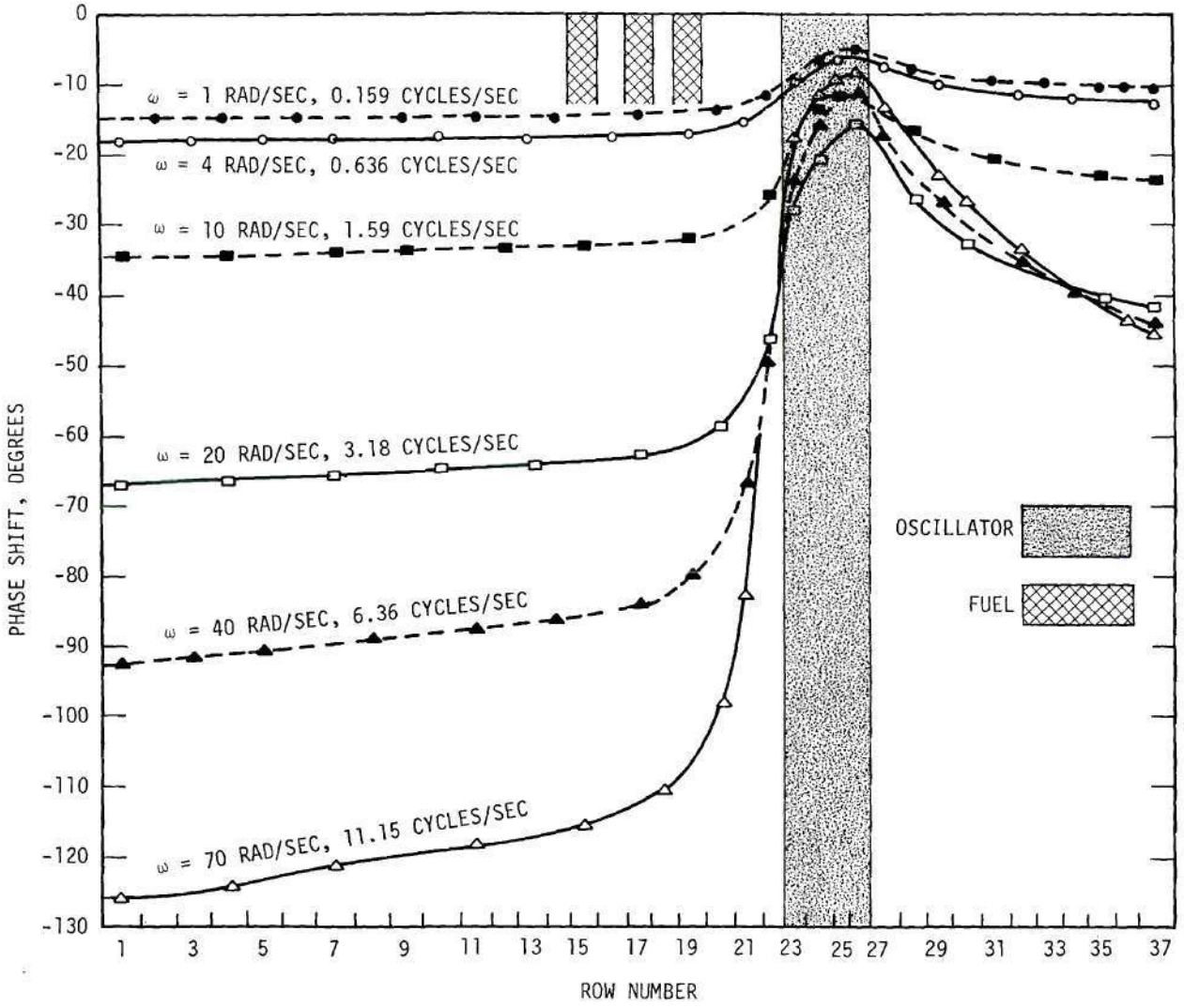

Figure 31. GTRR -- CRAM Results for the Phase Shift of the Neutron Flux versus Position Along Mesh Channel One for Different Frequencies

thermal and fast flux amplitudes show considerable fluctuations (Figure 26), their ratios, and hence the phase shift associated with them, increase continuously with distance from the oscillator (Figures 30 and 31). This phenomenon is physically reasonable. The fluctuations in the complex components were present because the fuel was represented explicitly in the mathematical model. From Figure 26 the information is present to determine the behavior of the amplitude (both fast and thermal) in the fuel and in the surrounding moderator. At a particular frequency, the amplitude is proportional to the square root of the sum of the squares of the real and quadrature components of the flux. Examination of Figure 26 reveals that the absolute value of the components of the fast response peak in the fuel and the absolute value of the components of the thermal response peak in the adjacent moderator. This result indicates that the fuel acts as an amplifier with a gain greater than one for the fast amplitude and less than one for the thermal amplitude. Thus, although the amplitude of the propagating disturbance increases and decreases as it traverses the core, the phase shift, both fast and thermal, monotonically increases with distance in all directions from the oscillator (Figures 30 and 31).

The results obtained from CRAM for the two-dimensional analysis were reasonable. However, solutions for frequencies beyond 70 radians per second were unobtainable due to lack of convergence. In fact, for all the frequencies reported, considering the size of the problem and comparing it with a normal statics problem, the rate of convergence was abnormally slow. These conditions provided further motivation to investigate other codes in an attempt to find a method of solution which was

definitive and could be obtained in a reasonable period of time.

One-Dimensional Analysis of the NORA Reactor to Check Modified EXTERMINATOR

EXTERMINATOR[41] is another one- and two-dimensional neutron diffusion code which allows for scattering from any group to any other group and also has provision for a constant source problem. Following some modifications[42] (namely, making the necessary changes to allow for negative values of the flux), EXTERMINATOR possessed the necessary features to solve a problem of the type being considered here. Initial calculations by EXTERMINATOR were performed in an attempt to reproduce previous results of CHARLIE and CRAM on the NORA one-dimensional problem. EXTERMINATOR was able to solve the low frequency case for a frequency of one radian per second. The number of iterations required varied from 29 to 233 depending upon the angle associated with the arbitrary source input and upon group ordering. A normal problem of this size is solved with less than 25 iterations. EXTERMINATOR was unsuccessful in finding a solution for the high frequency case of 400 radians per second. However, using the refined technique of group rebalancing,[43] convergence was obtained for the high frequency case. The phase angle results of the EXTERMINATOR test case (ω = 400 rad/sec) are shown in Figure 17. The case of one radian per second was rerun with group rebalancing and the problem converged in 13 iterations. As set up for the computer, this type of problem is essentially equivalent to a problem of two reactors which are extremely loosely coupled, one "real" and the other "imaginary."[44] This is exactly the condition under which group rebalancing, according to reference 43, should

and did accelerate convergence.

Based upon the success experienced with the one-dimensional NORA computations, a two-dimensional analysis was performed on the GTRR in an attempt to predict the results of the pile oscillator experiment described in Chapters II and III. The details of the calculations are reported in the next chapter. Included in Chapter VI is a comparison of the computed values with the experimental results.

CHAPTER VI

COMPARISON OF ANALYTICAL RESULTS FROM A TWO-DIMENSIONAL ANALYSIS OF THE GTRR USING EXTERMINATOR AND THE EXPERIMENTAL RESULTS OF THE GTRR PILE OSCILLATOR EXPERIMENT

The two-dimensional grid layout used in the EXTERMINATOR calculations is shown in Figure 32. Symmetry was assumed along the diameter which contained the pile oscillator (Chapter II, Figure 3). The homogenized half-core region was assumed to be composed of 5-1/2 fuel elements, four dummy elements and the associated heavy water. In contrast to the CRAM analysis described in Chapter V, the core was considered as homogenized for this analysis because the primary interest was in the behavior in the reflector corresponding to detector positions 1, 3, and 4, as shown in Figure 32. Had the fuel been represented explicitly, a finer grid would have been desirable, therefore increasing the computation time. In order to insure that mathematically a critical reactor was being analyzed, a two-group static calculation was performed initially to find the axial buckling B_z^2 which would satisfy the input specification of $k_{eff} = 1.0$. The value found for B_z^2 was 0.00163 cm^{-2}. A cross section of the static fluxes along mesh column 1 resulting from this calculation is shown in Figure 33. The two-group coefficients used for this analysis are given in Table 10. These two-group numbers, along with the above value of B_z^2 and the values of $\beta_i$eff and λ_i given in Table 11, were used as input for the B-5500 program KISEC (Appendix B) to generate the required "kinetic" cross sections

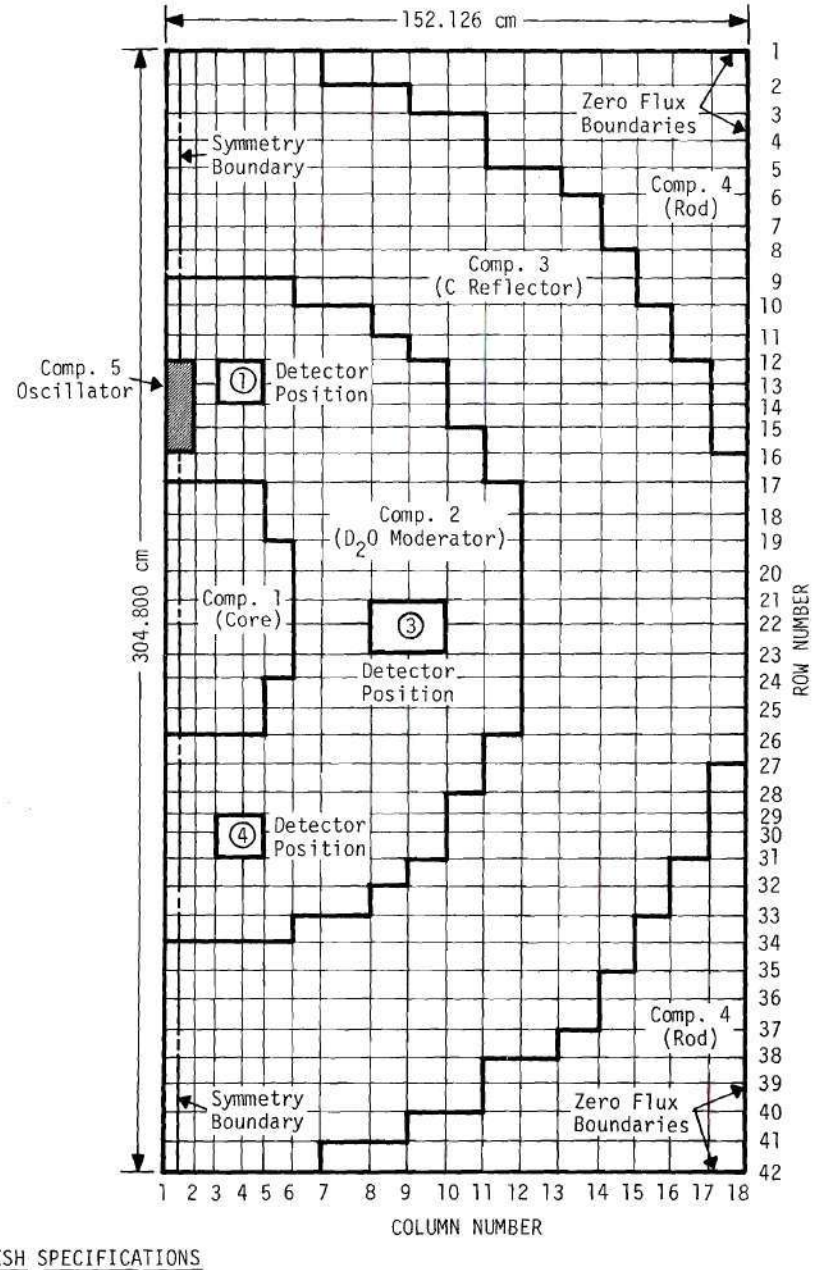

MESH SPECIFICATIONS

ROW	DELTA (cm)								
1	8.890	2	7.620	12	6.350	13	5.080	14	6.350
15	7.620	28	6.350	29	5.080	30	6.350	31	7.620
41	8.890	42							
COLUMN	DELTA (cm)								
1	7.620	2	5.578	3	7.620	4	5.578	5	7.620
6	10.160	18							

Figure 32. GTRR Two-Dimensional Core Grid for EXTERMINATOR Computer Description

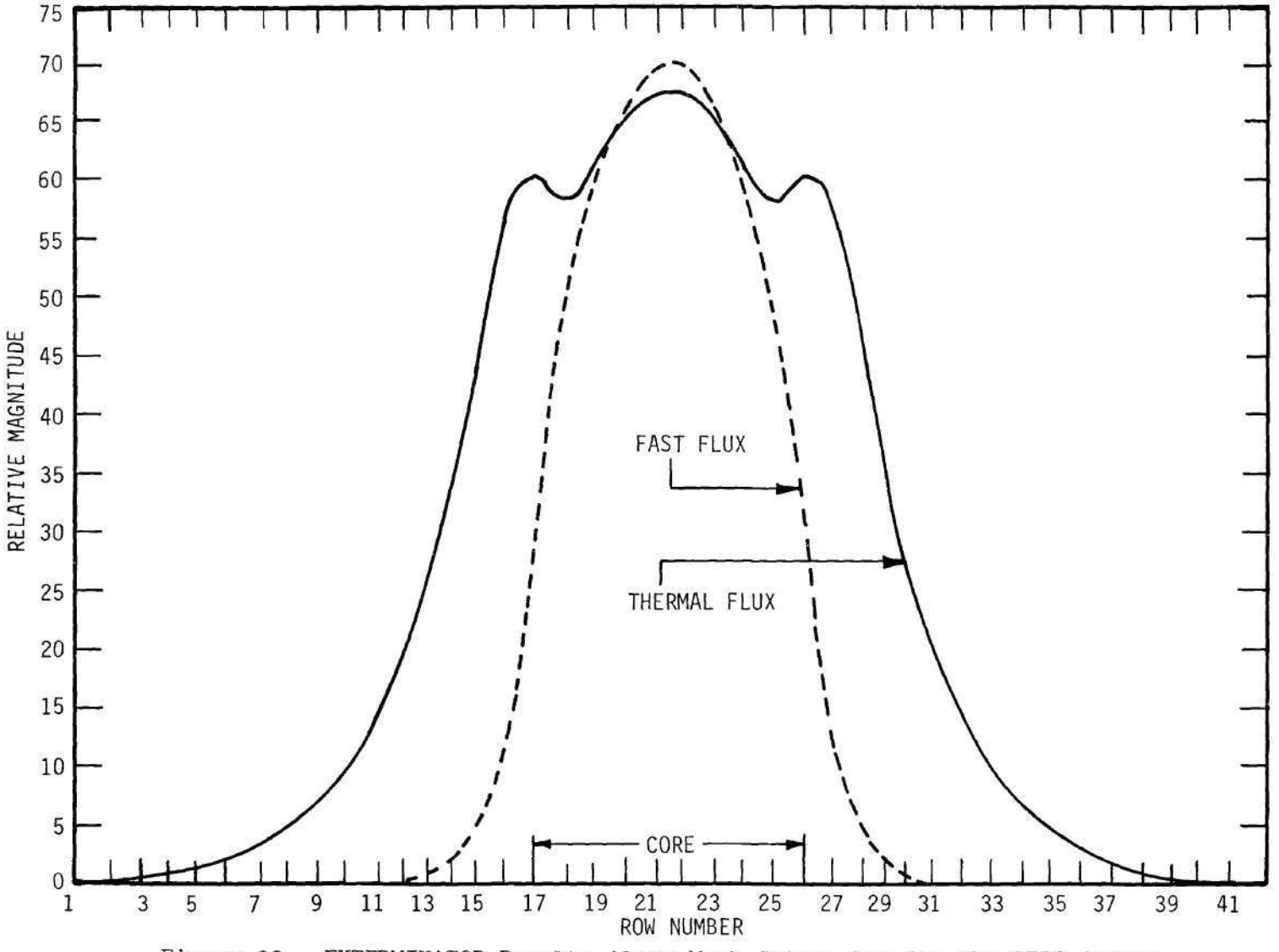

Figure 33. EXTERMINATOR Results Along Mesh Column One for the GTRR Static Flux Distribution

Table 10. "Static" Coefficients for Two-Group Analysis of the GTRR

	D_1 (cm)	D_2 (cm)	Σ_1^a (cm^{-1})	Σ_2^a (cm^{-1})	$\Sigma_{1\rightarrow 2}^s$ (cm^{-1})	$\nu_1 \Sigma_1^f$ (cm^{-1})	$\nu_2 \Sigma_2^f$ (cm^{-1})
Smeared Fuel Element	1.576	1.020	2.67×10^{-3}	4.80×10^{-2}	6.410×10^{-3}	3.630×10^{-3}	9.240×10^{-2}
D_2O Moderator (Core)	1.877	0.840	2.24×10^{-6}	7.51×10^{-5}	1.198×10^{-2}		
Dummy Cell	1.342	0.818	7.71×10^{-5}	5.45×10^{-4}	1.140×10^{-2}		
Homogenized Fuel Cell (Area Weighted)	1.732	0.864	4.75×10^{-4}	8.46×10^{-3}	1.094×10^{-2}	6.764×10^{-4}	1.722×10^{-2}
D_2O Reflector	1.274	0.794	3.68×10^{-5}	8.54×10^{-5}	1.880×10^{-2}		
Graphite Reflector	0.969	0.831	1.12×10^{-5}	2.55×10^{-4}	6.655×10^{-3}		

Table 11. Delayed Neutron Constants for the GTRR[45]

β_i eff	λ_i sec^{-1}
1.85×10^{-3}	1.96
6.12×10^{-4}	4.41×10^{-1}
2.06×10^{-3}	2.88×10^{-1}
1.21×10^{-3}	1.17×10^{-1}
1.50×10^{-3}	3.05×10^{-2}
2.54×10^{-4}	9.25×10^{-3}
2.33×10^{-5}	2.27×10^{-3}
1.51×10^{-5}	7.73×10^{-4}
1.07×10^{-5}	3.15×10^{-4}
1.70×10^{-5}	1.18×10^{-4}
3.79×10^{-6}	5.85×10^{-5}
2.10×10^{-7}	1.37×10^{-5}

for the frequencies of interest.

The solid lines in Figures 34 and 35 are traces from Figures 17 and 18 (Chapter III) showing the experimental results for phase and gain for detector positions 1, 3, and 4 (Figure 32). Plotted on these figures are the computed values for the same positions. The exact location of the effective center of the detector is not known. Therefore, both the largest and the smallest values of phase angle found for any points in the region (heavy black square) enclosing each of the detector positions 1, 3, and 4, as shown in Figure 32, were plotted. The "error bar" as plotted on Figure 34 connects these extreme values and is indicative of the gradient of the phase response in the vicinity of each particular detector location. Qualitatively, the general shape resulting from the numerical computations is reasonable both for the gain and phase curves. Quantitatively, the comparison of the results calls for further investigation.

Figure 36 shows the EXTERMINATOR results for the phase response as a function of frequency for selected positions along mesh column 1. For mesh column 1, point 13 and point 41 represent the extremes in response. Therefore, the data as plotted in Figure 36 show the maximum space-dependence in phase angle for the frequency range covered. Figure 37 is a similar graph showing the amplitude response as a function of frequency for selected positions along column 1. The crossover in the amplitude curves for points 14 and 16 can be explained by noting that this is exactly the location of the pile oscillator (i.e., the source is located between rows 12 and 16 in mesh column 1 for the computations). Thus, the observation to be made is that, although the amplitude for low frequencies is

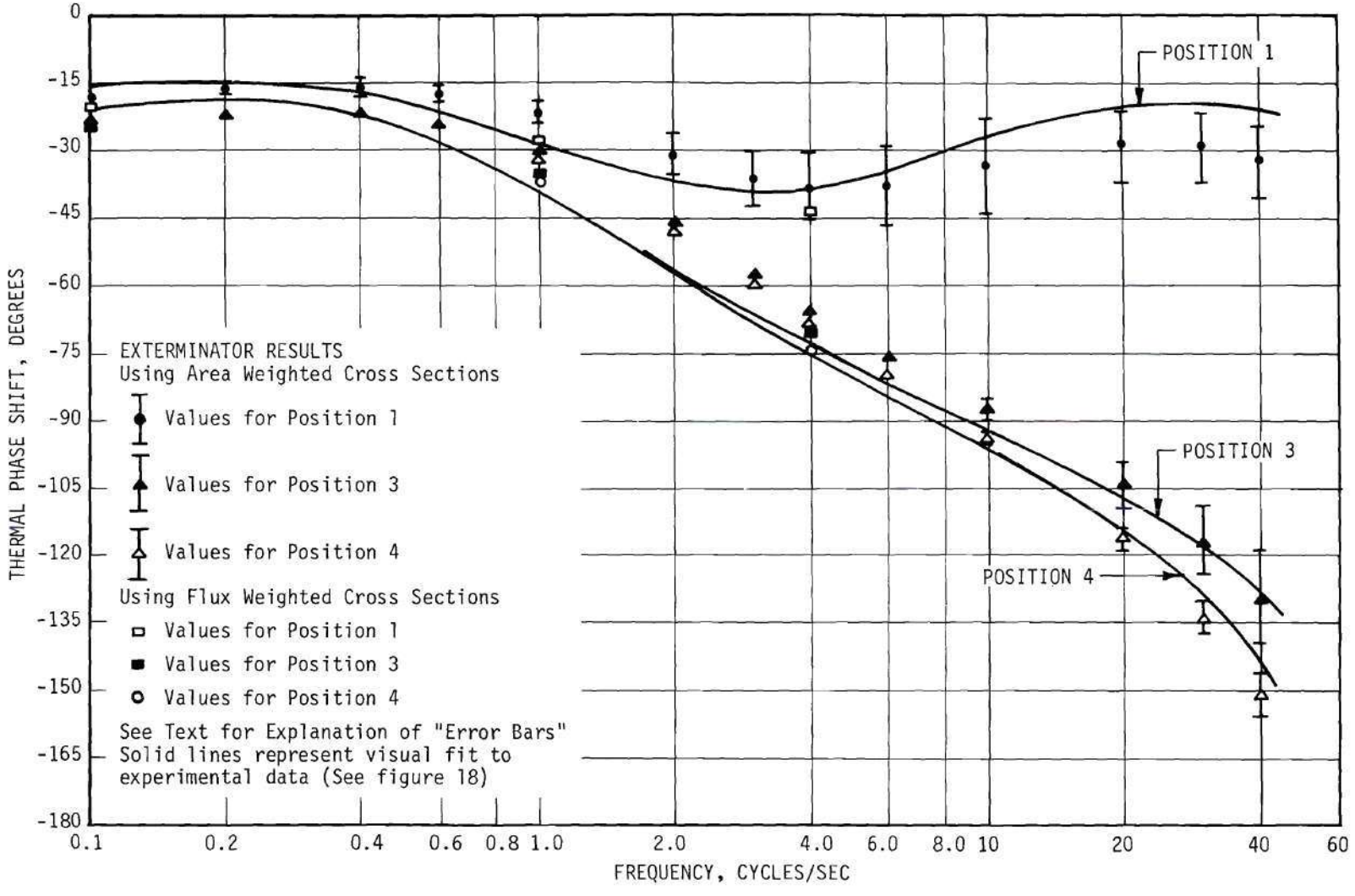

Figure 34. Experimental Thermal Phase Angle Results versus Frequency Compared with Digital Computations from EXTERMINATOR for the GTRR

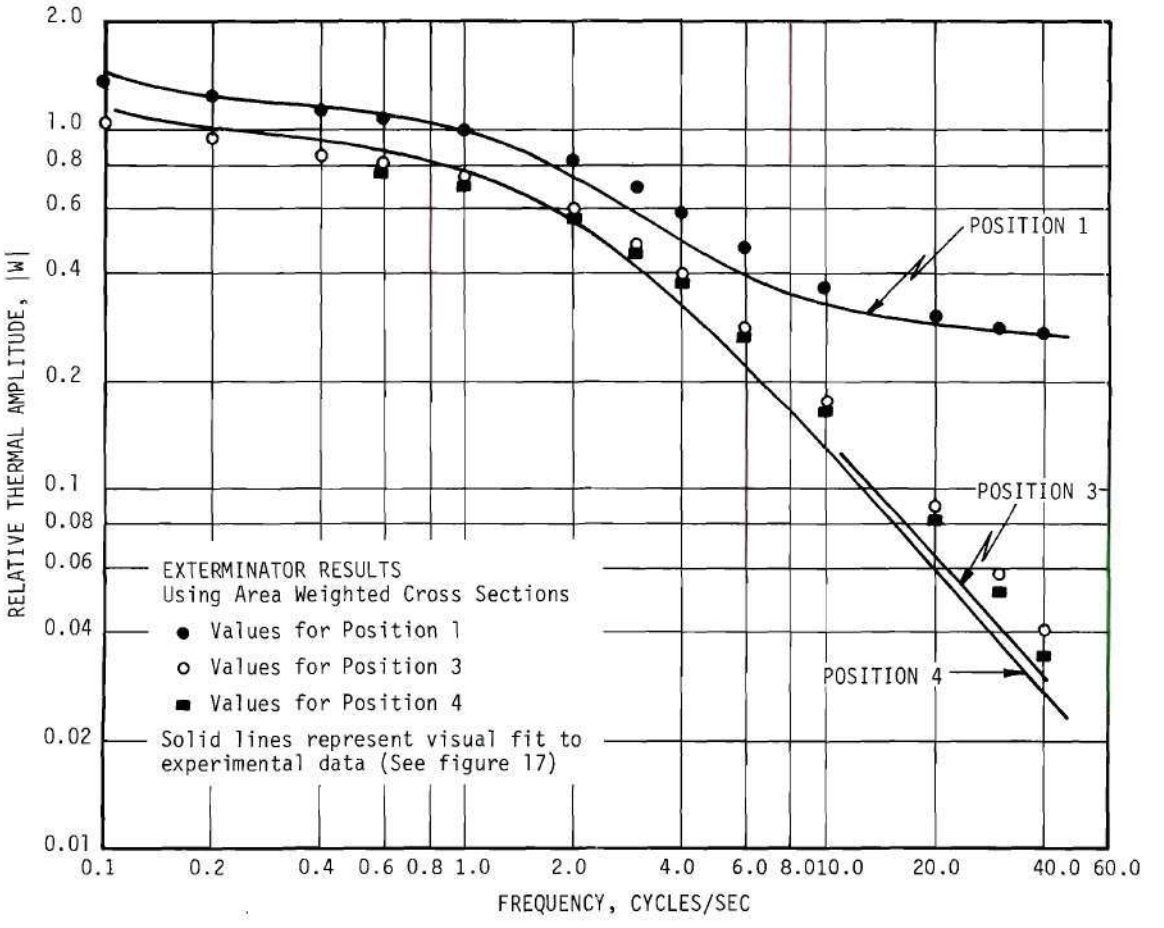

Figure 35. Experimental Thermal Amplitude Results versus Frequency Compared with Digital Computations from EXTERMINATOR for the GTRR

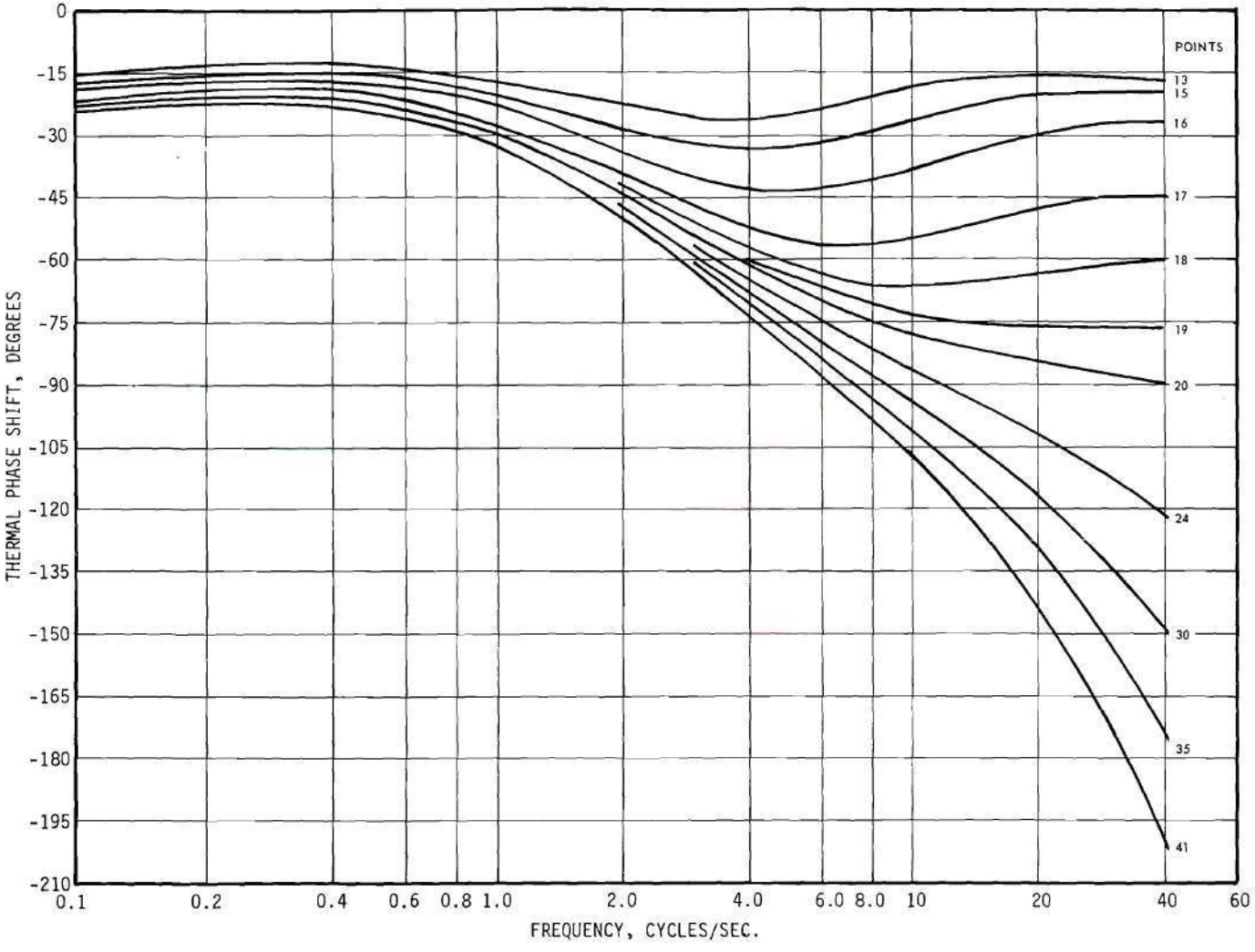

Figure 36. EXTERMINATOR Thermal Phase Angle Results versus Frequency for Selected Positions Along Mesh Column One for the GTRR

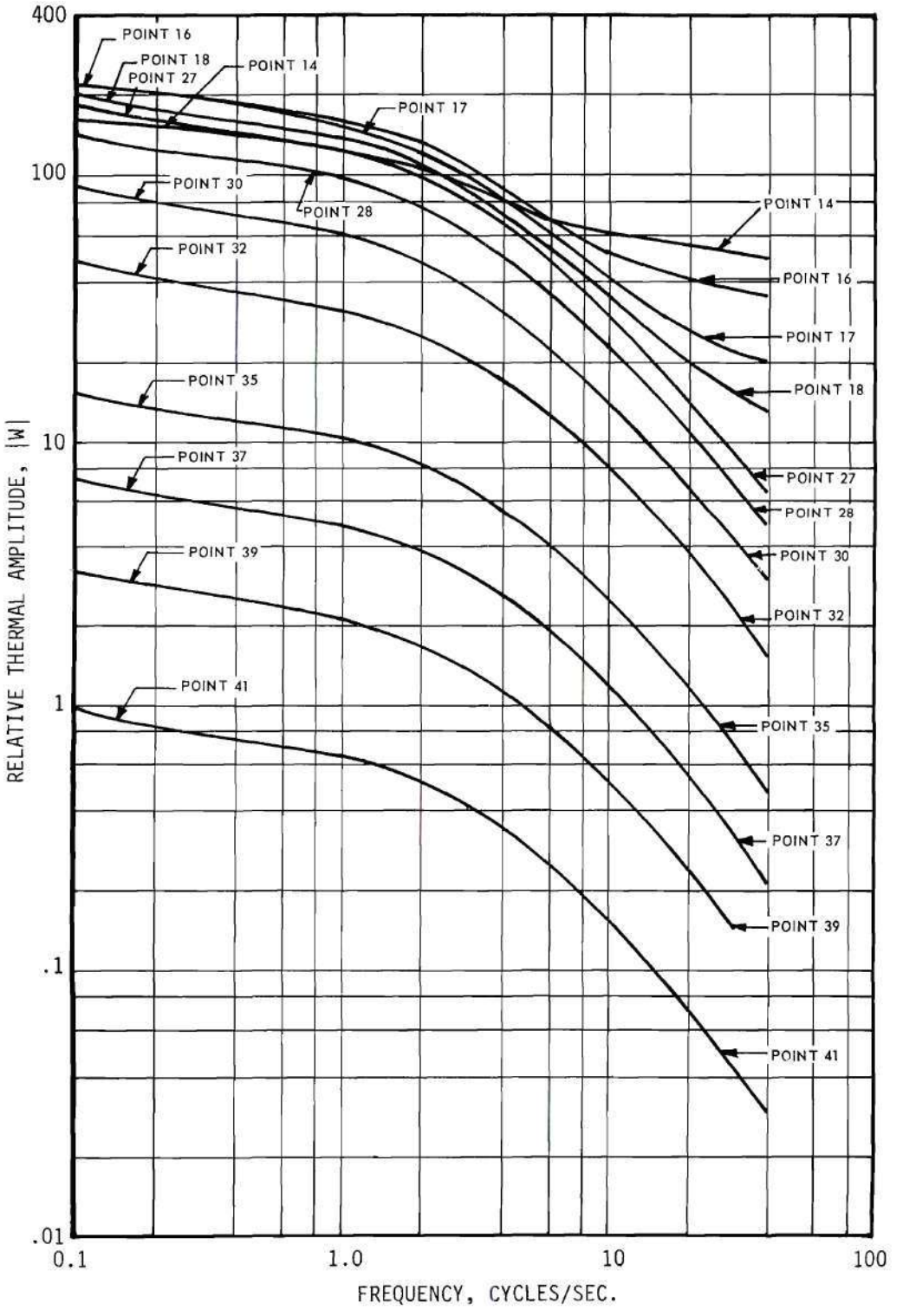

Figure 37. EXTERMINATOR Thermal Amplitude Results versus Frequency for Selected Positions Along Mesh Column One for the GTRR

smaller at point 14, its rate of fall-off with increasing frequency is not as great, and thus for high frequencies its amplitude is greater than that for point 16. This same observation can also be made by referring to Figures 38 through 40. Here the shift toward point 14 in the peak of the thermal real component as the frequency increases would cause the amplitude of point 14 not to decrease as rapidly as point 16 with increasing frequency and thus give rise to the phenomena discussed above.

Figures 38 through 40 show the complex components of the thermal and fast flux amplitudes along mesh column 1 for three different frequencies. These graphs show how each component changes in shape as a function of frequency.

Insight into the behavior of the reactor mid-plane flux can be seen by the sequence of Figures 41 through 43. These show lines of constant thermal phase shift over the entire grid of the reactor for several values of frequency. Figures 44 through 46 show lines of constant "thermal" amplitude for the same frequencies. In order to visualize the gradients present in the phase angle response, Figures 47 and 48 show both the fast and thermal phase angles as a function of position along mesh column 1 for various frequencies.

In an attempt to improve the agreement between the numerical results and the experimental values, a second set of cross sections was generated which "flux weighted" the thermal constants in the fuel cell in order to produce the homogenized coefficients. (Previous cross sections were area weighted to obtain the homogenized coefficients.) Details of the calculations used are in Appendix A. This set of cross sections allowed two possible representations of the reactor core. The homogenized

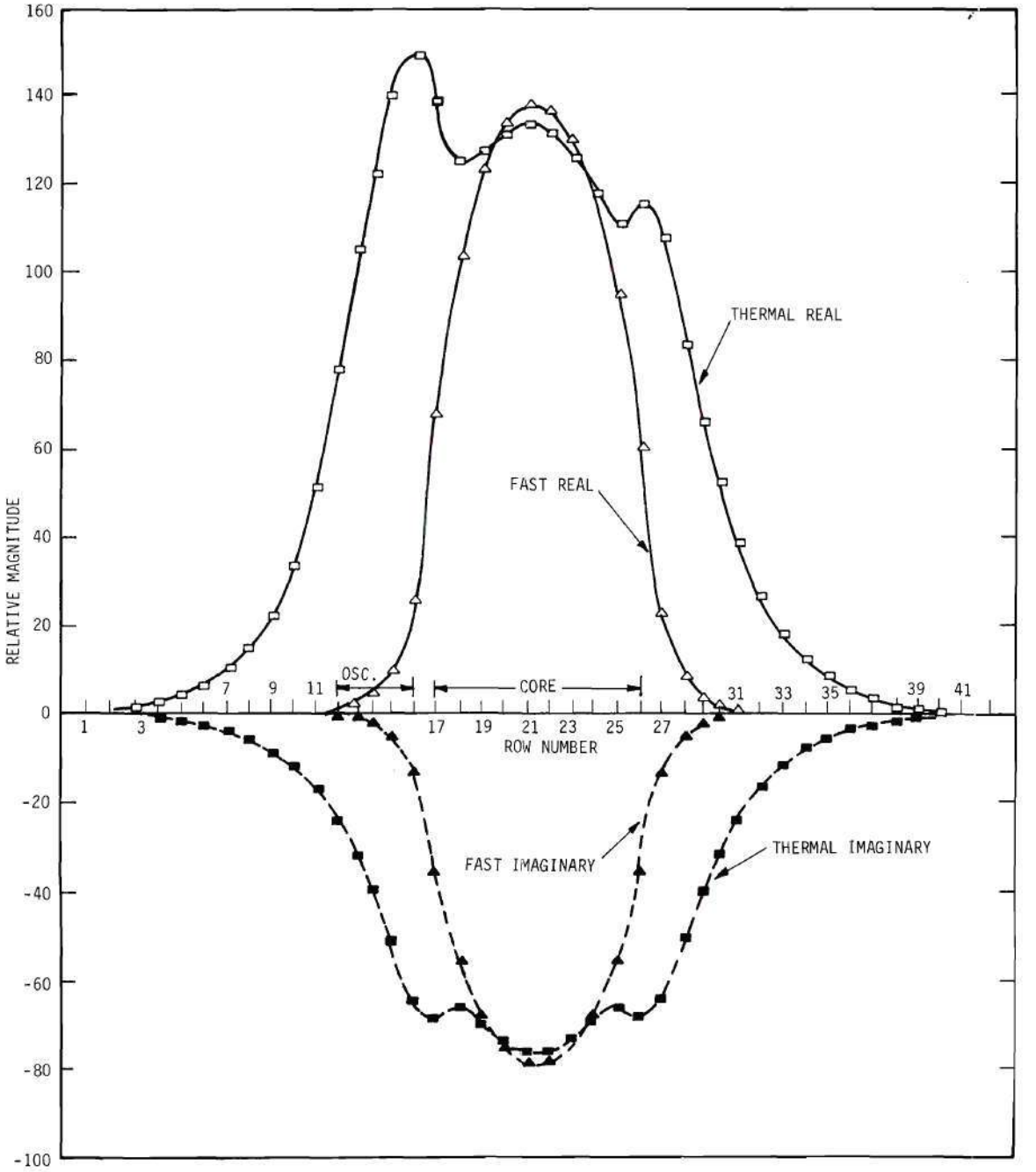

Figure 38. EXTERMINATOR Results Along Mesh Column One of the GTRR for the Complex Components of the Thermal and Fast Flux Amplitudes for an Input Disturbance Frequency of One Cycle Per Second

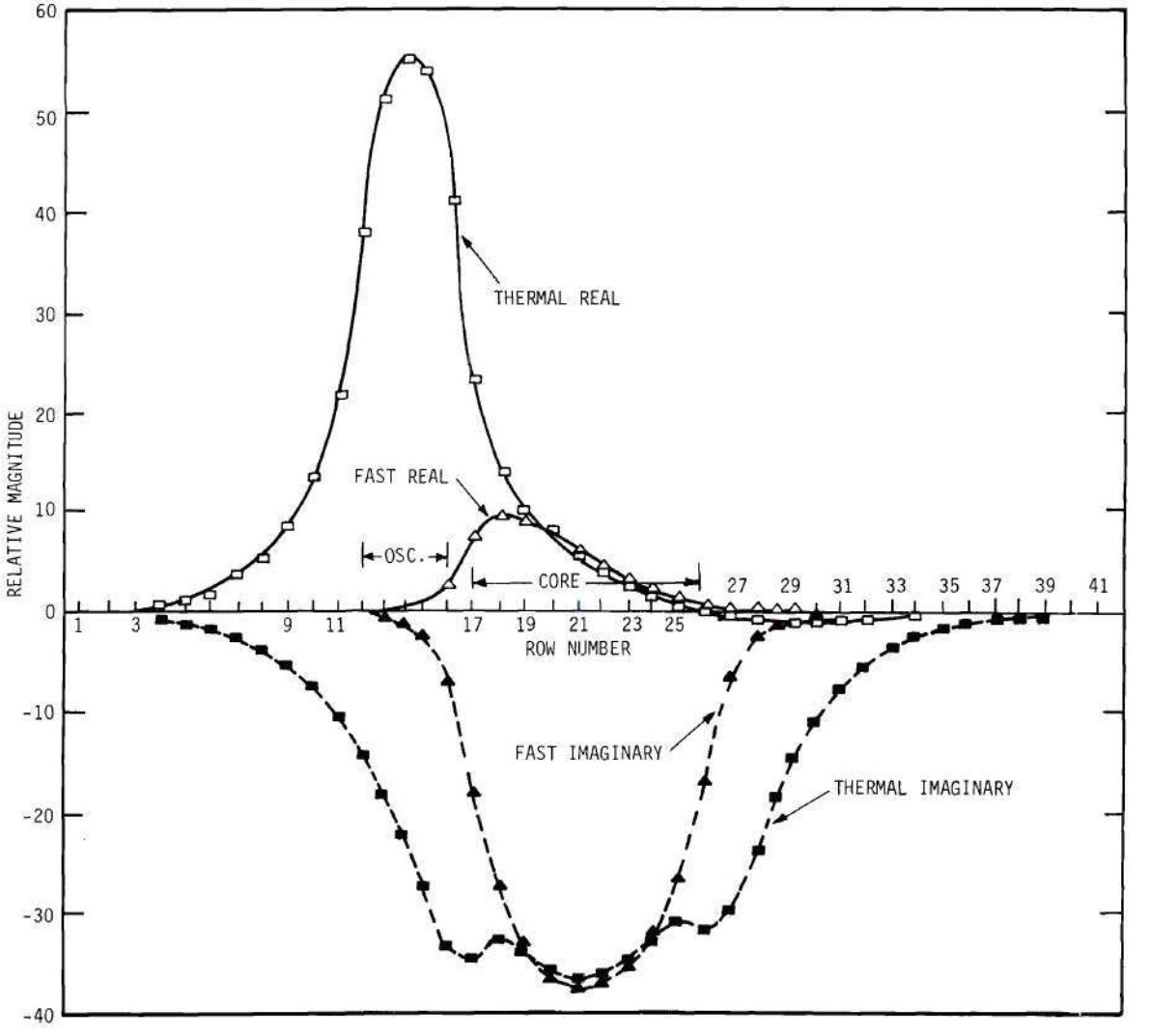

Figure 39. EXTERMINATOR Results Along Mesh Column One of the GTRR for the Complex Components of the Thermal and Fast Flux Amplitudes for an Input Disturbance Frequency of Ten Cycles Per Second

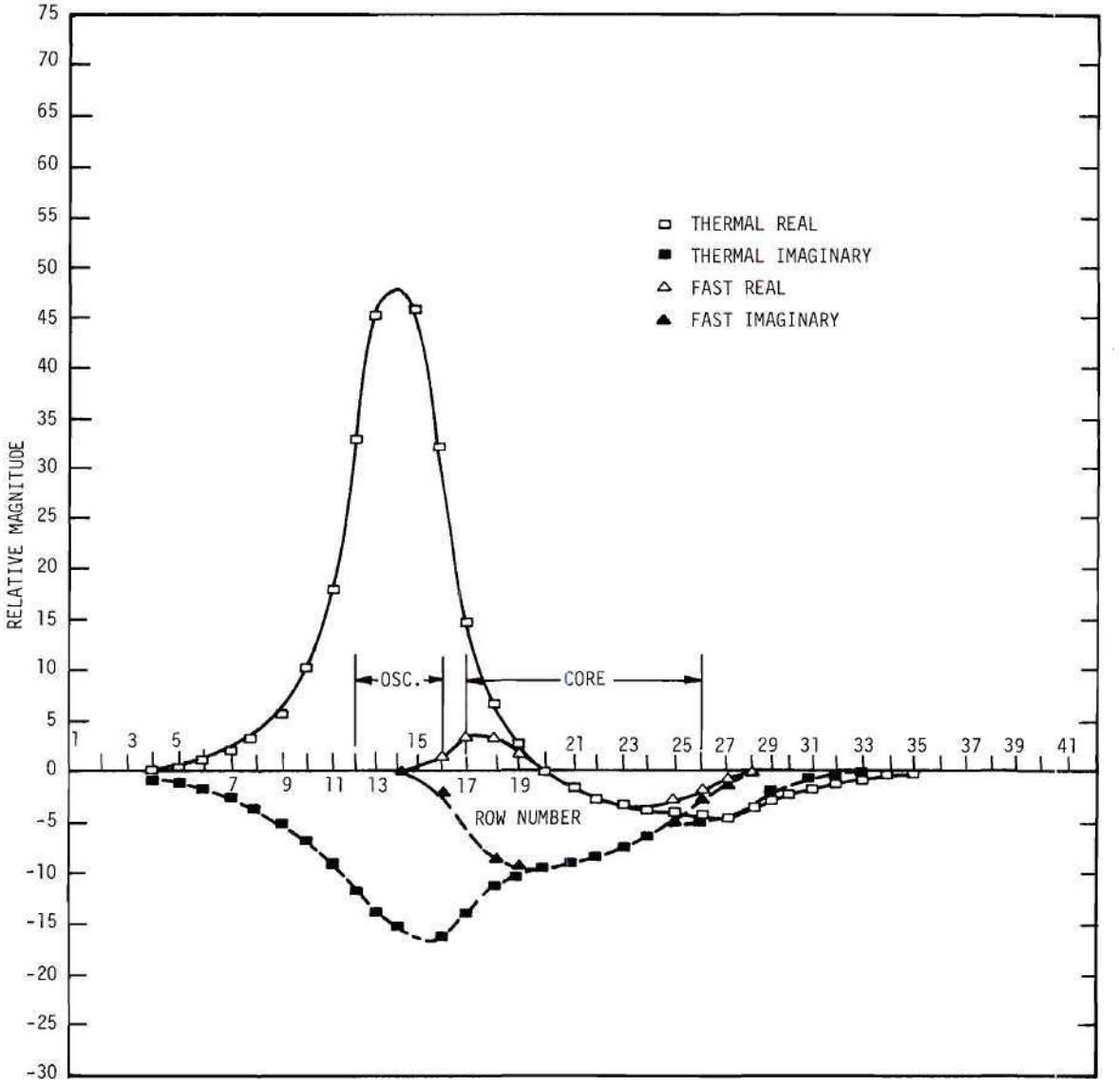

Figure 40. EXTERMINATOR Results Along Mesh Column One of the GTRR for the Complex Components of the Thermal and Fast Flux Amplitudes for an Input Disturbance Frequency of 41 Cycles Per Second

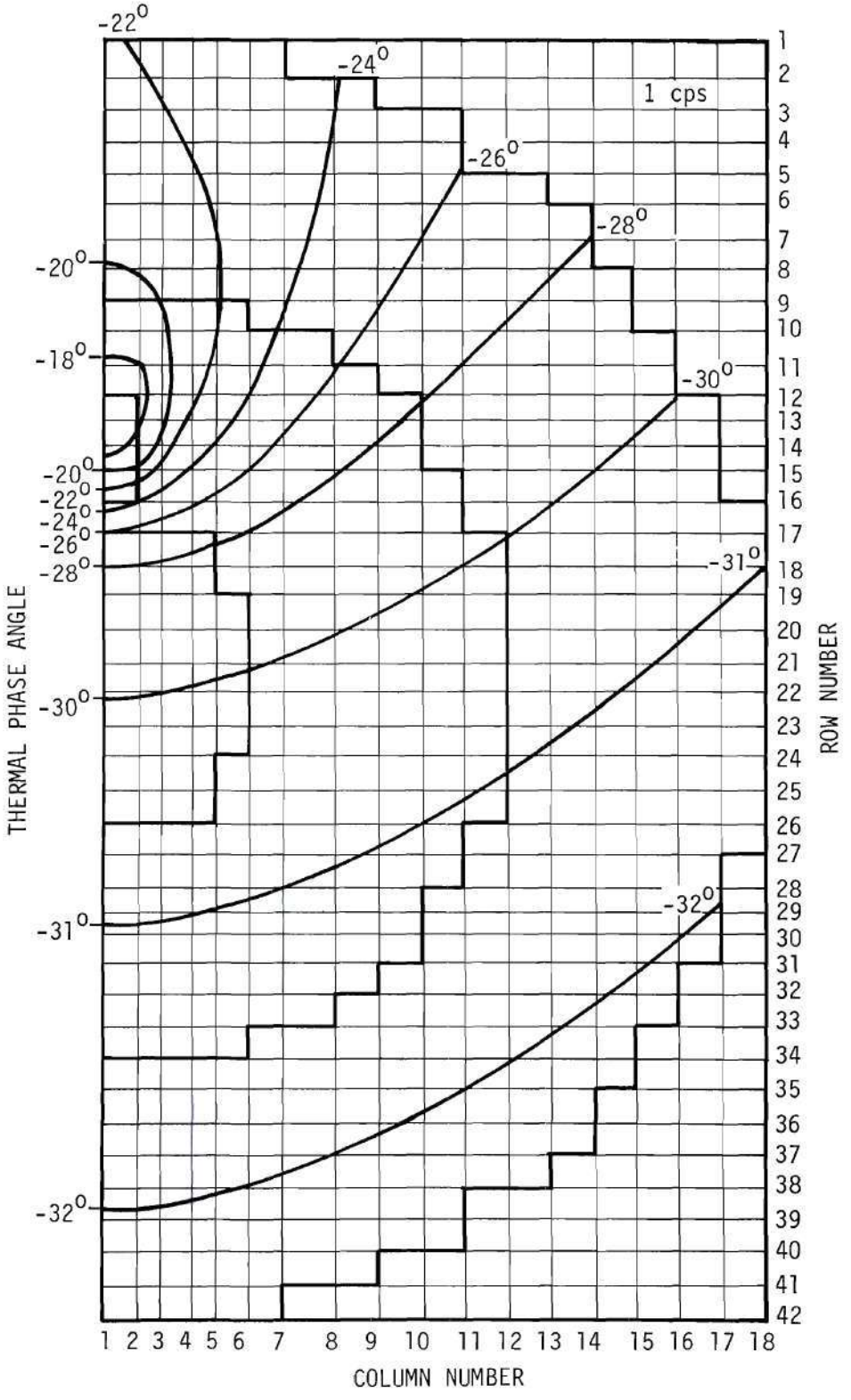

Figure 41. EXTERMINATOR Results for the GTRR Space-Dependent Thermal Phase Angle Response to an Input Disturbance Frequency of One Cycle Per Second

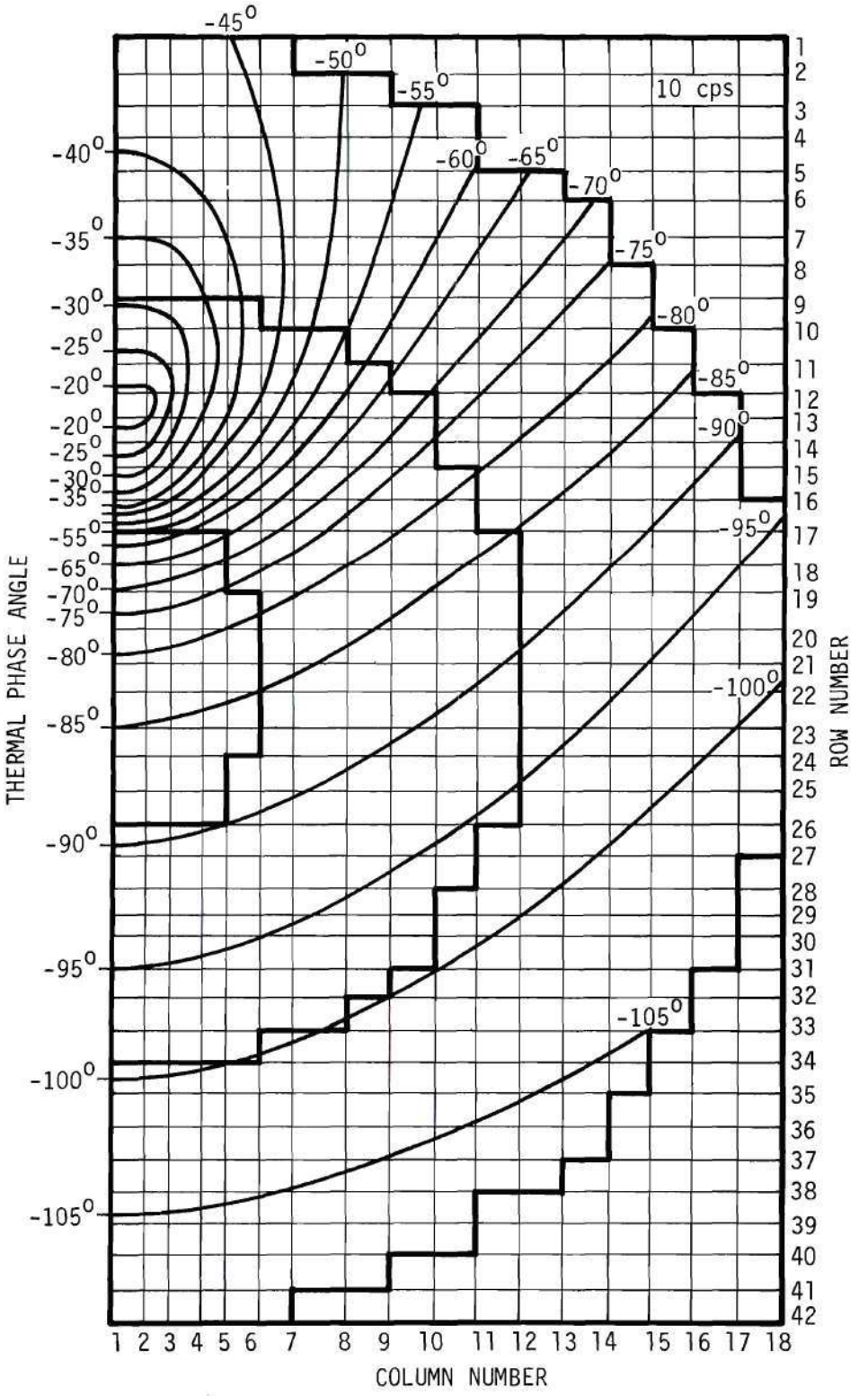

Figure 42. EXTERMINATOR Results for the GTRR Space-Dependent Thermal Phase Angle Response to an Input Disturbance Frequency of Ten Cycles Per Second

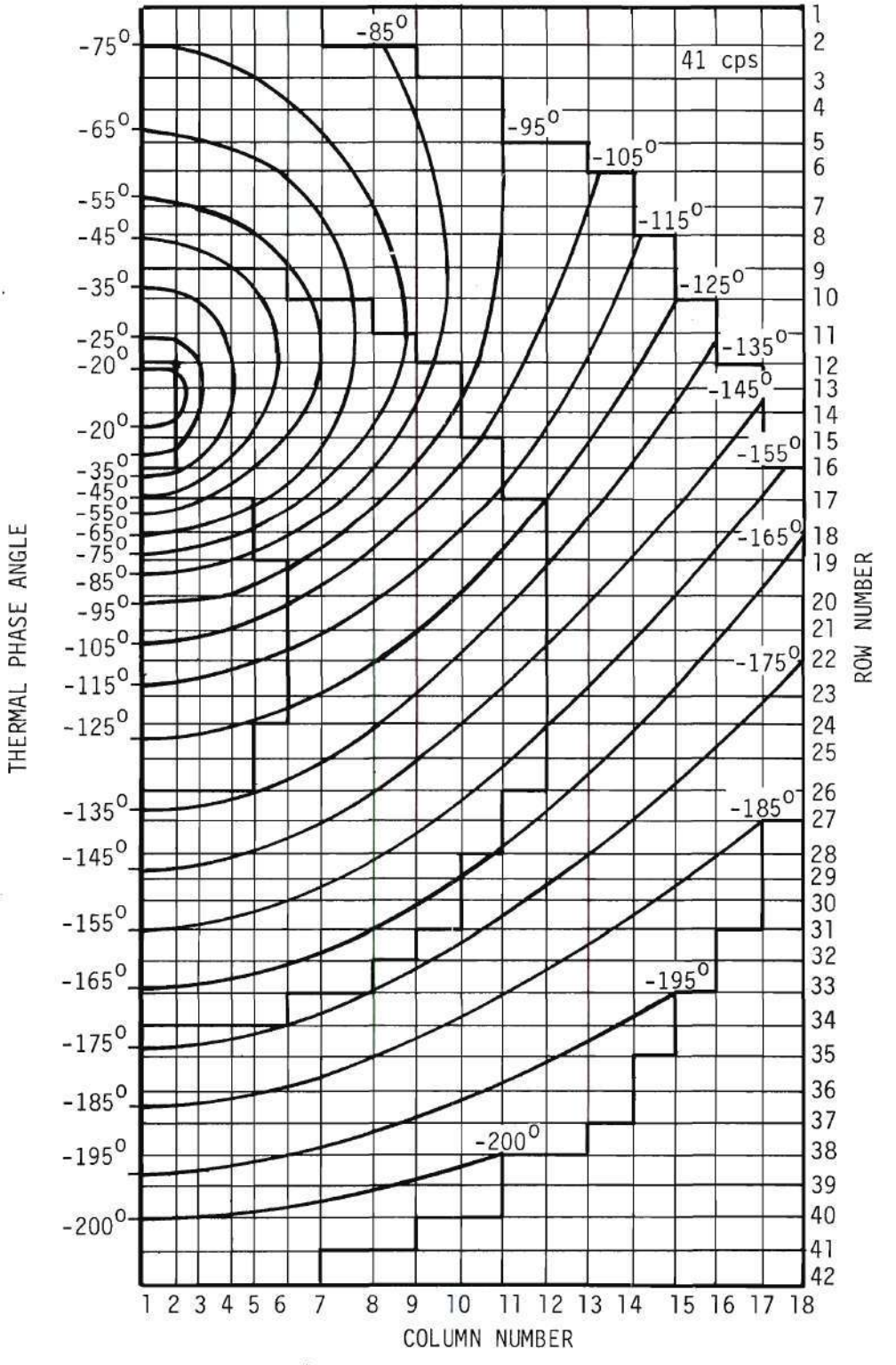

Figure 43. EXTERMINATOR Results for the GTRR Space-Dependent Thermal Phase Angle Response to an Input Disturbance Frequency of 41 Cycles Per Second

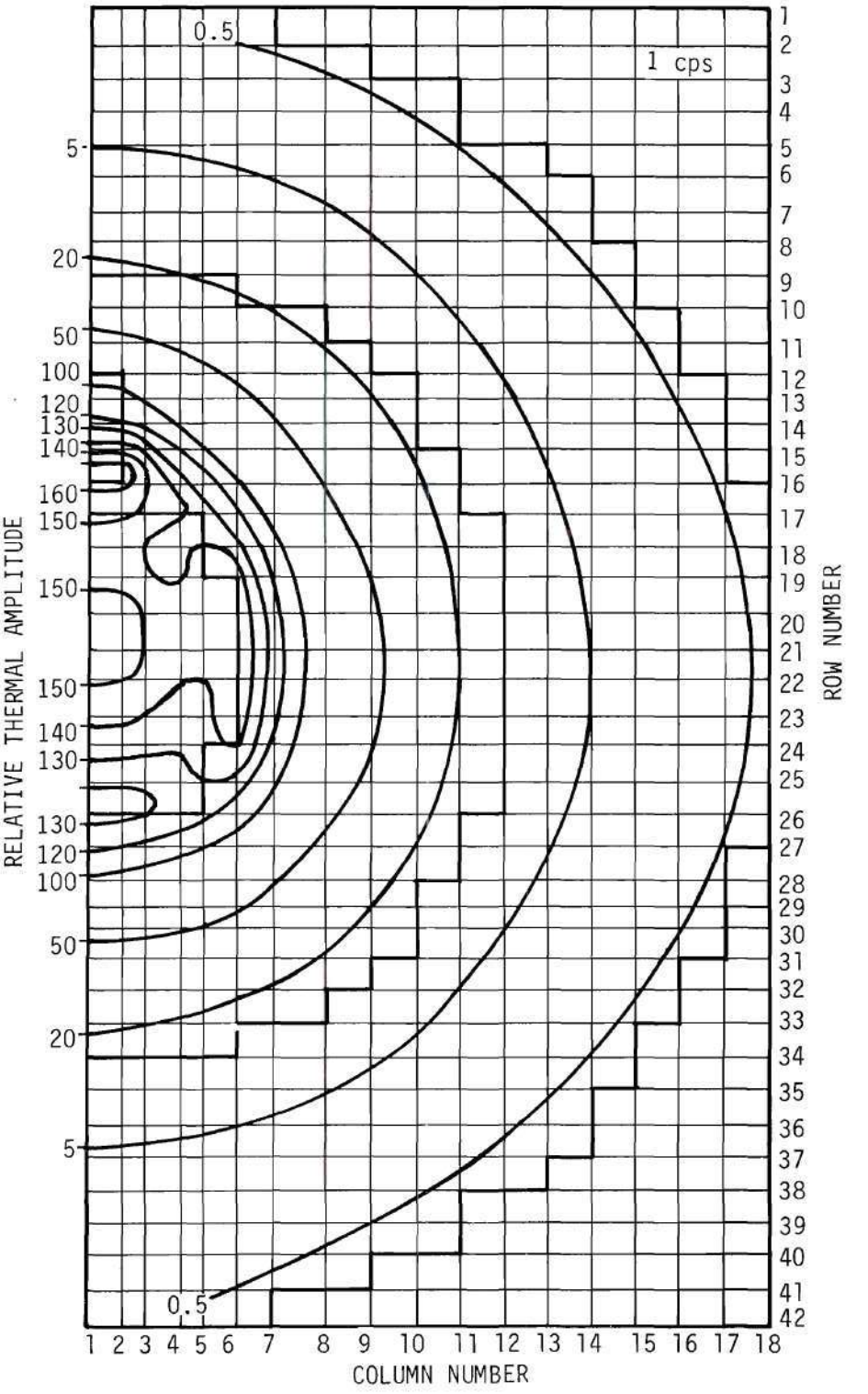

Figure 44. EXTERMINATOR Results for the GTRR Space-Dependent Thermal Amplitude Response to an Input Disturbance Frequency of One Cycle Per Second

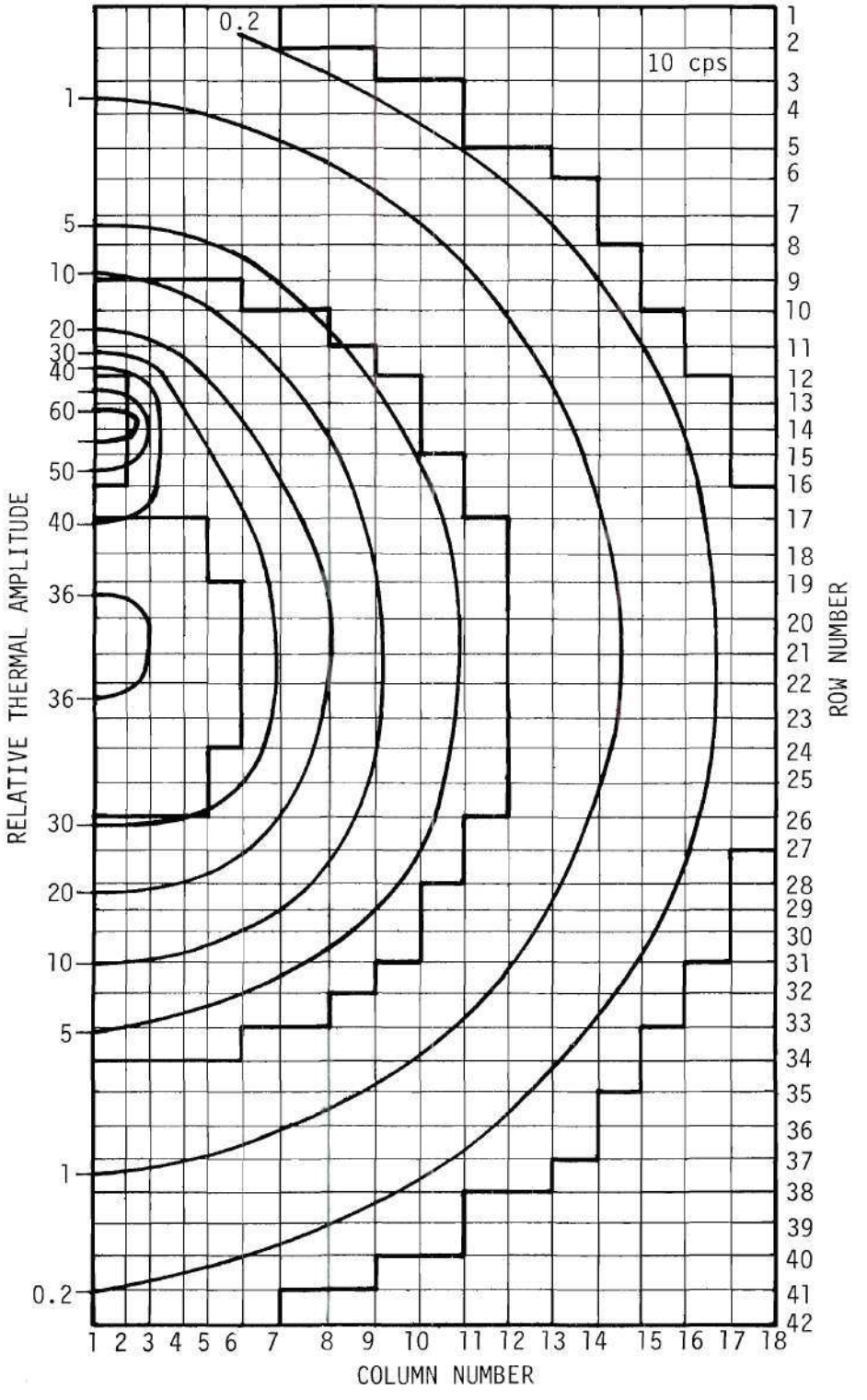

Figure 45. EXTERMINATOR Results for the GTRR Space-Dependent Thermal Amplitude Response to an Input Disturbance Frequency of Ten Cycles Per Second

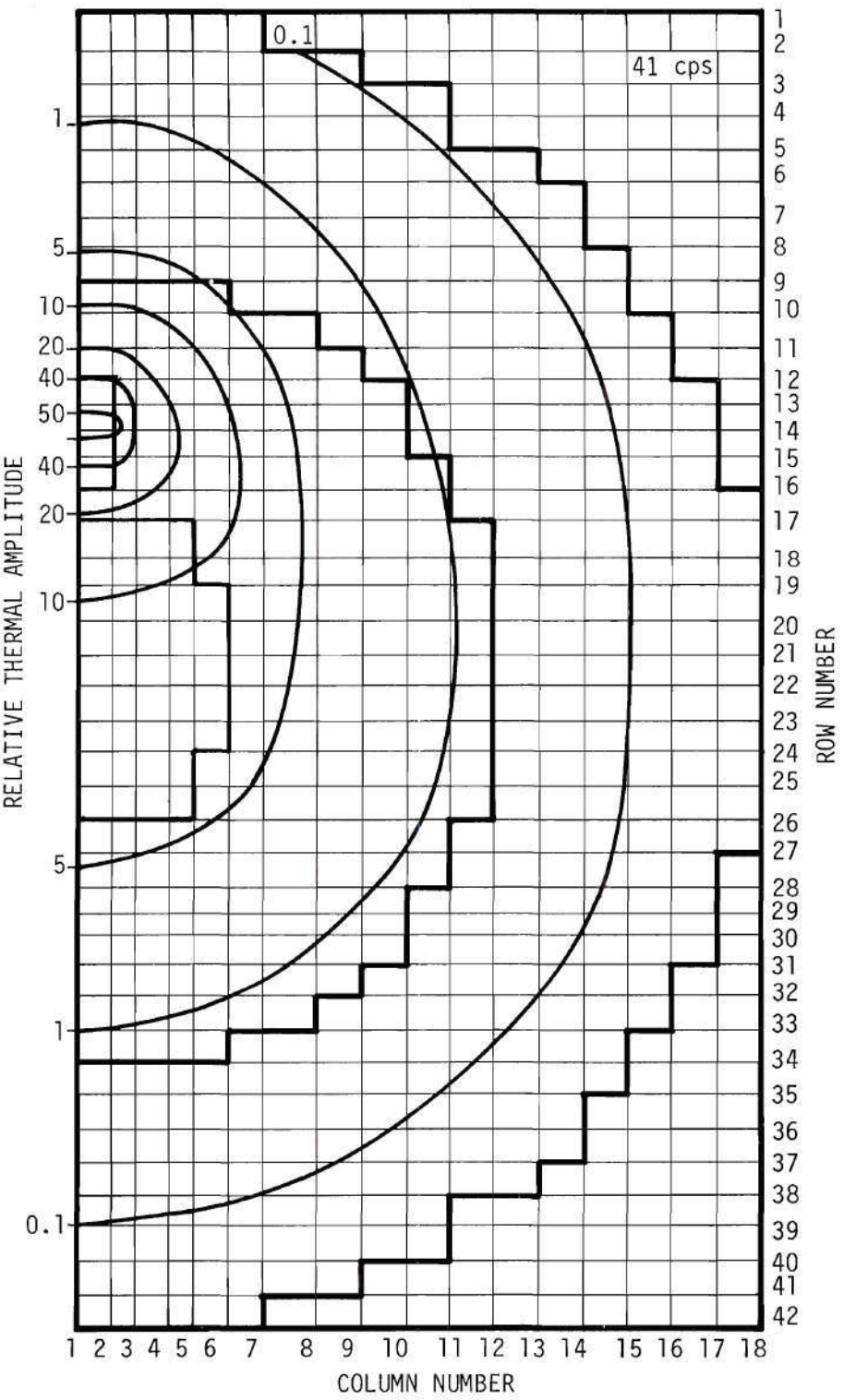

Figure 46. EXTERMINATOR Results for the GTRR Space-Dependent Thermal Amplitude Response to an Input Disturbance Frequency of 41 Cycles Per Second

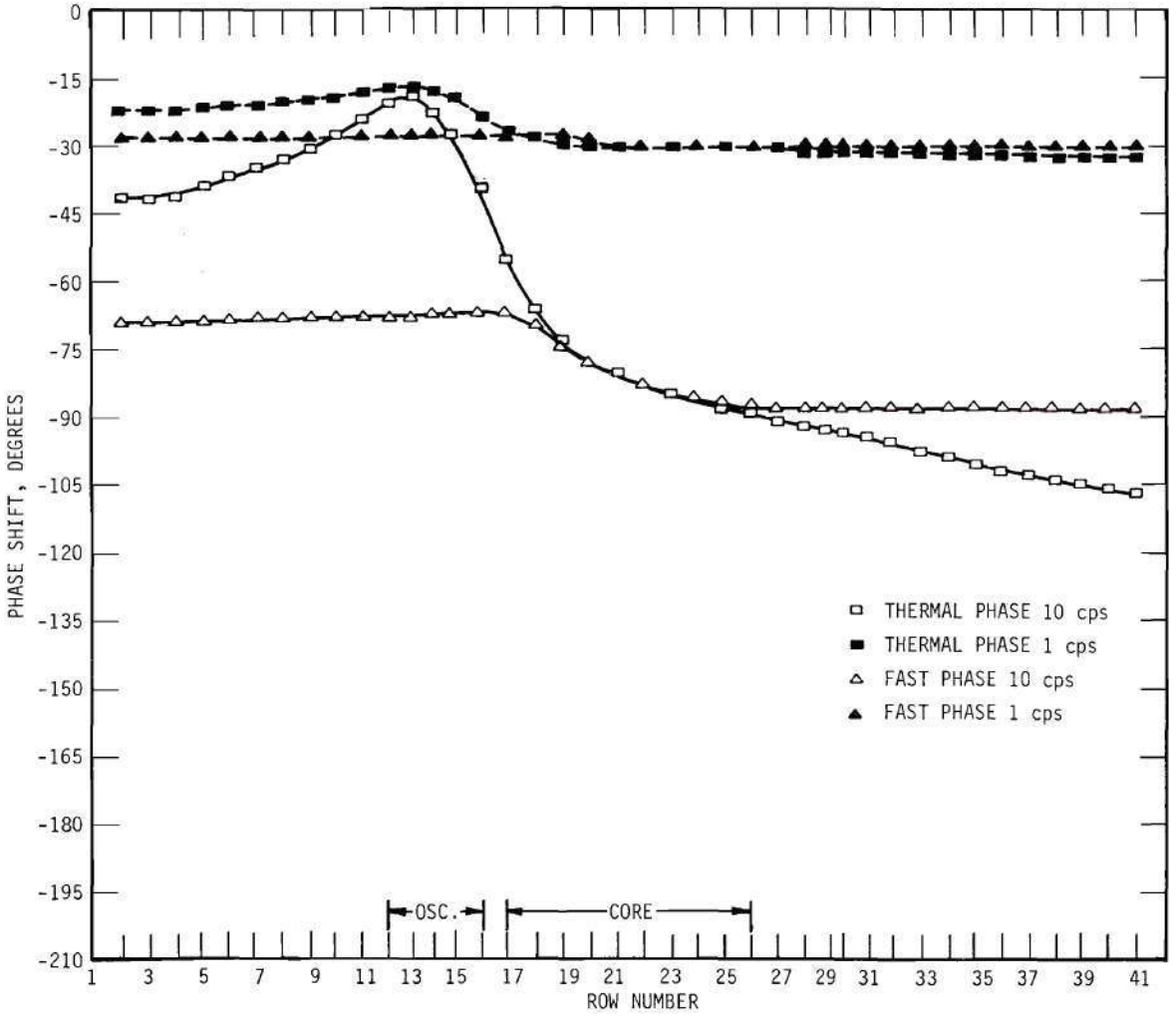

Figure 47. EXTERMINATOR Results for the Fast and Thermal Phase Angle Response of the GTRR versus Position Along Mesh Column One for Various Frequencies

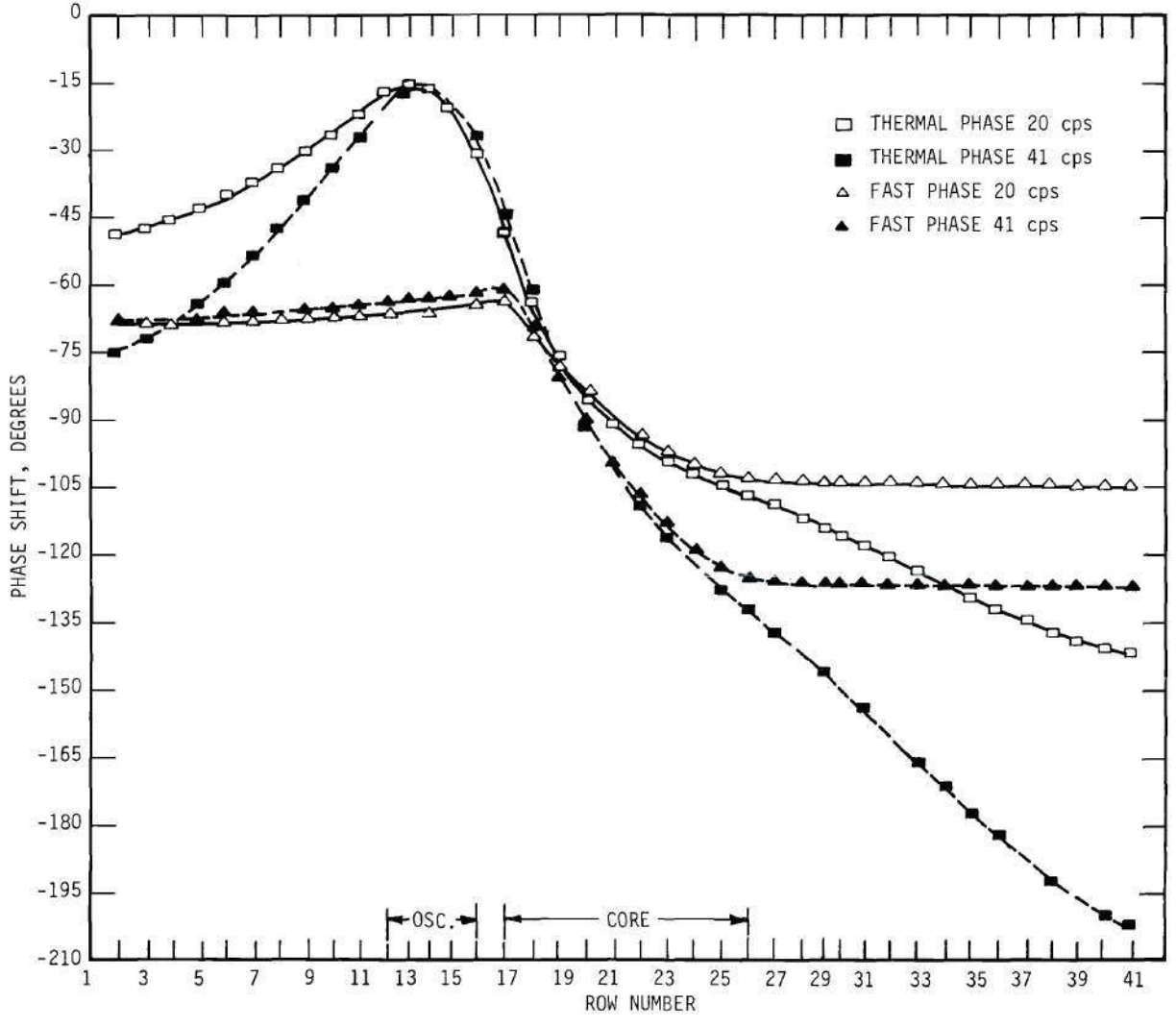

Figure 48. EXTERMINATOR Results for the Fast and Thermal Phase Angle Response of the GTRR versus Position Along Mesh Column One for Various Frequencies

fuel cell constants are used for a single region core representation. If the smeared fuel element constants are used, as was done in the CRAM analysis, the fuel and heavy water of the core could be represented separately. Specifying that the reactor be critical (i.e., $k_{eff} = 1$), the value of the axial buckling (considering the core homogenized) was found to be 0.00119 cm^{-2}. However, when the fuel and heavy water of the core were represented separately, the value of the buckling found was 0.00180 cm^{-2}. This result established the need for further investigation of the two-group coefficients.

Three additional calculations were run as test cases using these new flux weighted coefficients for frequencies of 0.1, 1.0, and 4.0 cycles per second (assuming a homogenized core). The phase angle results corresponding to detector positions 1, 3, and 4 are plotted in Figure 34, together with the results of previous EXTERMINATOR cases using the area weighted cross sections. The results for the three test cases were inconclusive. From Figure 34, the low frequency result (0.1 cps) shows less agreement with the experimental results. At 1.0 cps there is better agreement between experimental values and the values found for the additional test case. However, at 4.0 cps the results for positions 3 and 4 are in closer agreement with the experimental results but for position 1 the agreement is worse. Based upon the fact that the flux weighted two-group coefficients needed further investigation and that to perform a complete analysis of a number of frequencies would require a large amount of computer time, there was not sufficient justification to perform any further detailed calculations.

CHAPTER VII

CONCLUSIONS

As stated in Chapter I, the purpose of this thesis was to develop a numerical technique capable of predicting the response of the neutron flux throughout the reactor when it is subjected to a small periodic disturbance. The results obtained from the one-dimensional numerical analysis were in close agreement with the experimental values of gain and phase for the NORA reactor (Figures 19 and 20). Extension of this approach to include analysis of a two-dimensional system required seeking a different method of solution. That is, the system of equations in the one-dimensional case could be solved by direct matrix inversion. However, for a two-dimensional problem, the size of the matrix prohibits this approach. Investigation of existing computer codes revealed the possibility of using CRAM and EXTERMINATOR. These codes allowed for an external source, provided for scattering from any group to any other group, and in the case of CRAM, allowed for a negative flux. EXTERMINATOR, following modification by Mr. T. B. Fowler of Oak Ridge National Laboratory, would allow for a negative flux. Considerable convergence difficulties were experienced for both one- and two-dimensional problems using CRAM. Subsequent investigation of this problem revealed no satisfactory solution. Preliminary calculations using EXTERMINATOR revealed convergence difficulties similar to those which occurred when using CRAM. However, when the technique of individual group rebalancing was applied, conver-

gence was definitive. The speed of convergence remains the primary obstacle to extensive use of this technique. The two-dimensional results obtained for the analysis of the GTRR were in qualitative agreement with experimental measurements (Figures 34 and 35). Based upon further investigation and closer examination of the input constants, it has been deduced that a major improvement in these numbers is possible.

The goals of this thesis were realized. A pile oscillator experiment was designed and data taken which showed the space-dependent effect present in the response of the neutron flux of the GTRR when subjected to a periodic disturbance produced by varying the absorption present at a particular location. A numerical technique was developed which computed the space-dependent kinetic response of a stationary fueled reactor when subjected to a small periodically varying external source.

CHAPTER VIII

RECOMMENDATIONS

The results of this work have demonstrated that EXTERMINATOR is capable of providing the means of solution to problems of the type investigated herein. However, the usefulness of this technique is limited by the large amounts of computer time involved due to the slow convergence. Further problems should be investigated for the specific purpose of developing techniques to speed convergence. When the speed of convergence is made acceptable, the extension to more groups, three dimensions, and the incorporation of feedback would be an area of fruitful investigation.

From the results reported pertaining to the GTRR, it is clear that a thorough investigation of the two-group coefficients is merited. With the acquisition of a consistent set of coefficients, repetition of the analysis of the GTRR pile oscillator experiment would be rewarding.

Further parameter studies are feasible, particularly if the speed of convergence is increased. Specifically, by varying the height and thus changing the value of k_{eff}, families of curves could be generated indicating the response of the reactor as a function of k_{eff}. This particular parameter study was investigated by both CHARLIE and CRAM for the one-dimensional analysis. However, the results from EXTERMINATOR have not been obtained for various reactivities.

No allowance for the effect of photoneutrons on the transfer func-

tion has been incorporated in the mathematical model. Experimentally, at low power levels, the photoneutron source in the reactor is significant. The consequence of this phenomenon should be investigated.

The operating history of the reactor was not considered. Both at high and low power levels, there are significant reasons to believe that this parameter is important. Future experiments should attempt to isolate the variations in the response of the gain and phase as a function of operating history.

Further experimental programs should be established along with continued development of the analytical model. A thorough investigation should attempt to reveal the sensitivity of the results both experimentally and analytically. For example, a long vertical oscillator could be fabricated and the experiment repeated. These results should more closely approximate the mathematical model used for the analysis described in this thesis. Analytically, a parameter study should be performed to establish the sensitivity of the results to variations in the input constants. In fact, future research might reveal that this "static-kinetic" experiment and associated analysis constitute a much more detailed and sensitive test of the accuracy of a set of group constants than do current conventional statics measurements and analyses.

APPENDICES

APPENDIX A

GENERATION OF THE "STATIC" COEFFICIENTS FOR A TWO-GROUP ANALYSIS OF THE GEORGIA TECH RESEARCH REACTOR

A physical description of the Georgia Tech Research Reactor was given in Chapter II, Instrumentation and Equipment. In Chapter V, Application of Theory, a computational procedure was described in which a grid was used to represent the reactor core mid-plane. Application of this technique to a particular reactor requires numerical values of the descriptive constants for each of the regions being represented. In this appendix are presented the steps followed in generating the values of these constants.

The regions for which constants were determined were the core, the heavy water surrounding the core, and the graphite reflector. Two sets of constants were determined for the core, based upon the following assumptions:

1. the entire core was considered as homogenized
2. only the fuel element (three inches by three inches) was considered homogenized (smeared).

The calculations to obtain the pertinent number densities for the individual elements within these regions will be outlined in the subsequent discussion. Table 12 provides the basic data used in the computations.

Table 12. Parameter Values Used in the Determination of the Number Densities

Component	Density (grams/cm^3)	Atomic or Molecular Weight
Al (1100)	2.71[47]	26.9815
C (AGOT graphite)	1.70	12.01115
D		2.01410
O		15.9994
U-235		235.0439
U-238		238.0508
U	19.05[48]	
D_2O (72°F)	1.10490[49]	20.0276
H_2O (72°F)	0.99775[50]	18.0151

Moderator purity = 99.77 weight percent D_2O

Average enrichment in the fuel = 93.18 weight percent U-235

Fuel element loading = 142.19 grams of U-235 + 10.41 grams of U-238

Atom Density Calculations

To obtain the atom densities, the following relation was used.

$$N = \frac{\text{nuclei}}{\text{vol}} = \left(\frac{\text{mass}}{\text{vol}}\right)\left(\frac{\text{mole}}{\text{mass}}\right)\left(\frac{\text{nuclei}}{\text{mole}}\right) \tag{85}$$

where

ρ = density = mass/volume

$\hat{A}$ = nuclei/mole = Avogadro's number

$= (0.6023 \times 10^{24})$

a = mass/mole = atomic or molecular weight

Substituting these definitions into the expression for N gives

$$N = \frac{\rho \hat{A}}{a} \tag{86}$$

Graphite Reflector

Number density for atoms of C

$$N(C) = \frac{(1.70)(0.602252)(10^{24})}{(12.01115)} \tag{87}$$

$$= (0.0852)(10^{24}) \frac{\text{atoms C}}{\text{cm}^3 \text{ reflector}}$$

Moderator (99.77 weight percent D_2O)

$$\text{V.F. } (D_2O) = \text{Volume fraction of } D_2O \tag{88}$$

$$= \frac{(0.9977)\ \rho_m}{(1.10490)}$$

$$\text{V.F. } (H_2O) = \frac{(0.0023)\ \rho_m}{(0.99775)} \tag{89}$$

where ρ_m = density of the moderator (grams/cm^3)

$$\text{V.F. } (D_2O) + \text{V.F. } (H_2O) = 1 \tag{90}$$

Combining equations 88, 89, and 90 and solving for ρ_m gives

$$\rho_m = 1.1046 \text{ grams/cm}^3 \text{ moderator} \tag{91}$$

Number density for molecules of D_2O

$$N(D_2O) = \frac{(0.9977)(1.1046)(0.602252)(10^{24})}{(20.0276)} \tag{92}$$

$$= (0.03314)(10^{24})\ \frac{\text{molecules of } D_2O}{\text{cm}^3 \text{ moderator}}$$

Number density for atoms of D

$$N(D) = 2\ N(D_2O) \tag{93}$$

$$= (0.06628)(10^{24})\ \frac{\text{atoms D}}{\text{cm}^3 \text{ moderator}}$$

Number density for molecules of H_2O

$$N(H_2O) = \frac{(0.0023)(1.1046)(0.602252)(10^{24})}{(18.0151)} \tag{94}$$

$$= (0.000085)(10^{24}) \frac{\text{molecules of } H_2O}{\text{cm}^3 \text{ moderator}}$$

Number density for atoms of H

$$N(H) = 2\ N(H_2O) \tag{95}$$

$$= (0.00017)(10^{24}) \frac{\text{atoms H}}{\text{cm}^3 \text{ moderator}}$$

Number density for atoms of O

$$N(O) = N(D_2O) + N(H_2O) \tag{96}$$

$$= (0.03322)(10^{24}) \frac{\text{atoms O}}{\text{cm}^3 \text{ moderator}}$$

The computation of the number densities for the fuel region was based upon a fuel element smeared (homogenized) within a square, three inches on a side. A cross section of a fuel element with the pertinent dimensions indicated is shown in Figure 49.

Smeared Fuel Element

Total cross section area = 9 in^2 = 58.1 cm^2

Active fuel length in a fuel element = 23.5 in = 59.7 cm

Number density for atoms of U-235

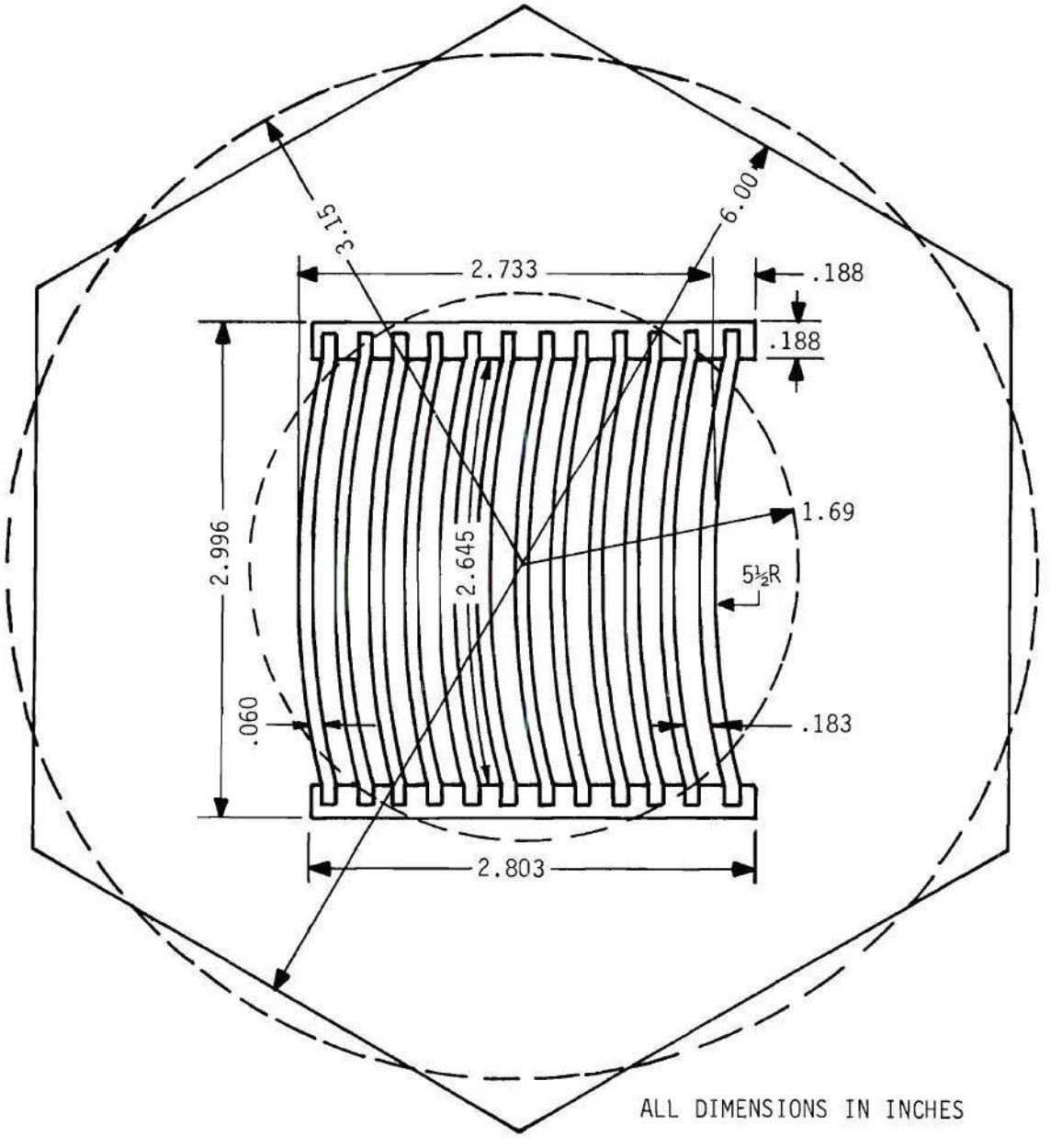

Figure 49. Typical GTRR Fuel Cell Cross Section

$$N(U\text{-}235) = \frac{(142.19)(0.602252)(10^{24})}{(59.7)(58.1)\ (235.0439)} \tag{97}$$

$$= (0.000105)(10^{24})\ \frac{\text{atoms U-235}}{\text{cm}^3\ \text{smeared fuel element}}$$

Number density for atoms of U-238

$$N(U\text{-}238) = \frac{(10.41)(0.602252)(10^{24})}{(59.7)(58.1)\ (238.0508)} \tag{98}$$

$$= (0.00000759)(10^{24})\ \frac{\text{atoms U-238}}{\text{cm}^3\ \text{smeared fuel element}}$$

Area Computations

The cross-sectional "area" of the uranium was computed as follows in order to determine the volume fraction of the aluminum and moderator within the smeared fuel element.

$$\text{Uranium area} = \frac{152.60\ \text{gm U}}{23.5\ \text{in}}\ \frac{\text{cm}^3}{19.05\ \text{gm U}}\left(\frac{1\ \text{in}}{2.54\ \text{cm}}\right)^3 \tag{99}$$

$$= 0.0208\ \text{in}^2$$

The dimensions necessary to compute the cross-sectional metal area are given in Figure 49.

$$\text{Area 12 plates} = (12)(0.060)(2.645)$$

$$= 1.90\ \text{in}^2$$

$$\text{Area 2 side plates} = (2)(0.188)(2.803)$$

$$= 1.05\ \text{in}^2$$

$$\text{Metal area} = 2.95 \text{ in}^2 \tag{100}$$

$$\begin{aligned}\text{Moderator area} &= \text{total area} - \text{metal area} \\ &= 9.00 - 2.95 \\ &= 6.05 \text{ in}^2\end{aligned} \tag{101}$$

$$\begin{aligned}\text{Aluminum area} &= \text{metal area} - \text{Uranium area} \\ &= 2.93 \text{ in}^2\end{aligned} \tag{102}$$

Volume Fractions

The volume fraction of each fuel element component was based upon the cross-sectional areas previously computed.

$$\begin{aligned}\text{Volume fraction of Al} &= \text{Aluminum area} \div \text{total area} \\ &= \frac{2.93}{9.00} \\ &= 0.326\end{aligned} \tag{103}$$

$$\text{Volume fraction of Moderator} = 0.672 \tag{104}$$

$$\text{Volume fraction of Uranium} = 0.002 \tag{105}$$

Number density for atoms of Al

$$N(\text{Al}) = \frac{(0.326)(2.71)(0.602252)(10^{24})}{(26.9815)} \tag{106}$$

$$= (0.0197)(10^{24}) \frac{\text{atoms Al}}{\text{cm}^3 \text{ smeared fuel element}}$$

Number density for atoms of D

$$N(D) = (\text{volume fraction of moderator in smeared fuel element}) \times (\text{number density for atoms of D in moderator}) \tag{107}$$

$$= (0.672)(0.06628)(10^{24})$$

$$= (0.0445)(10^{24}) \frac{\text{atoms D}}{\text{cm}^3 \text{ smeared fuel element}}$$

Number density for atoms of H

$$N(H) = (0.672)(0.00017)(10^{24}) \tag{108}$$

$$= (0.00011)(10^{24}) \frac{\text{atoms H}}{\text{cm}^3 \text{ smeared fuel element}}$$

Number density for atoms of O

$$N(O) = (0.672)(0.03322)(10^{24}) \tag{109}$$

$$= (0.0223)(10^{24}) \frac{\text{atoms O}}{\text{cm}^3 \text{ smeared fuel element}}$$

An alternate approach to representing the core as composed of smeared fuel elements surrounded by heavy water is to consider the core as completely homogenized and thus represent the entire core as one region. In order to determine the core parameters under this assumption, a typical "fuel cell" was defined by the following technique. Figure 50 shows the 19 possible fuel element positions arranged on a six-inch triangular pitch. Also shown is the hexagonal pattern superimposed upon the

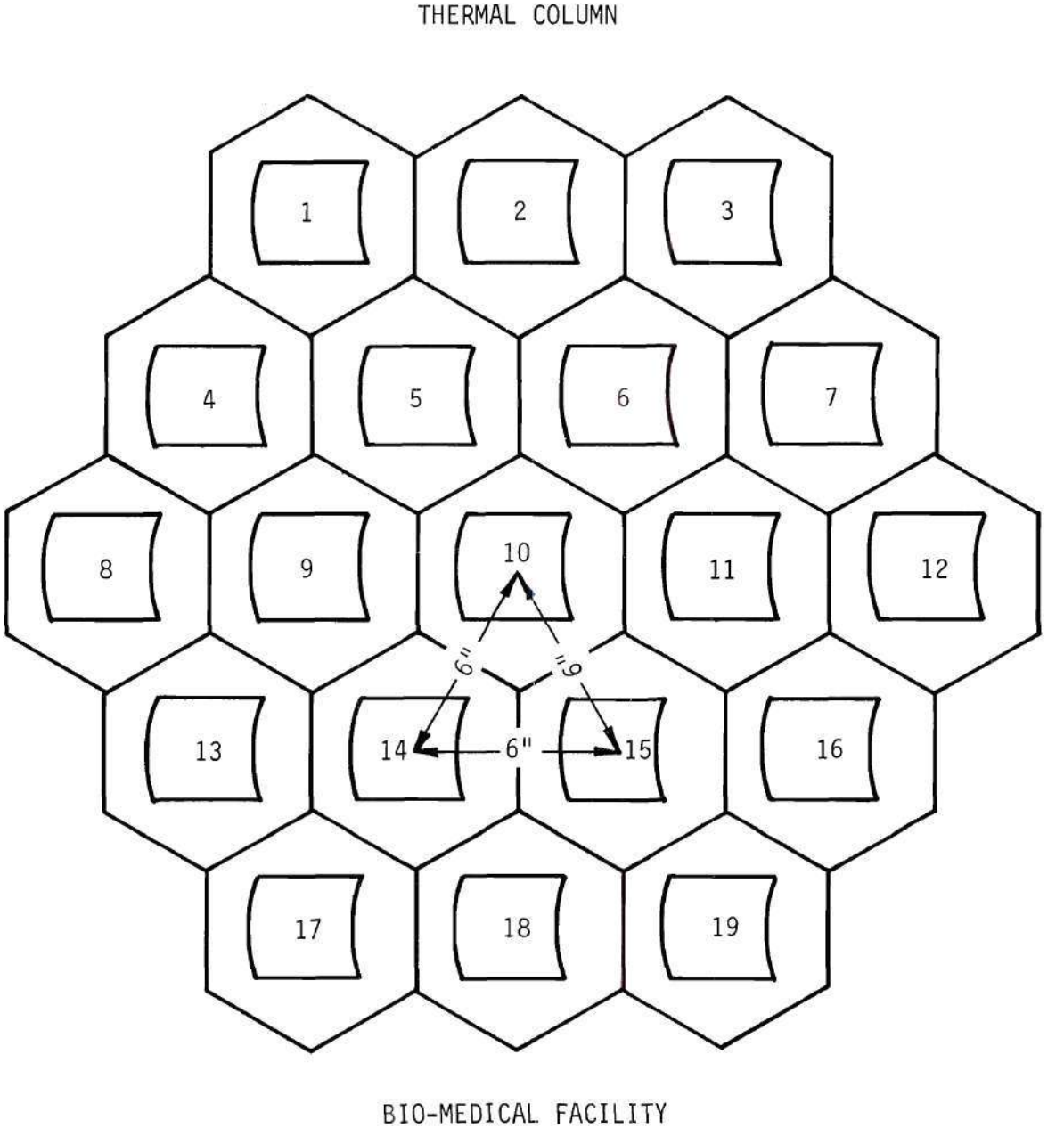

Figure 50. GTRR Core Lattice with 19 Hexagonal Fuel Cells

array. Assuming a fuel element is located within its boundaries, each hexagon defines a fuel cell (Figure 49). The number densities for the homogenized fuel cell were obtained by volume weighting (area weighting) over the fuel cell the proper number densities previously calculated.

Homogenized Fuel Cell

Area fuel cell = 201 cm^2 (Figure 49)

Area fuel element = 58.1 cm^2

Area D_2O surrounding the fuel element = 143 cm^2

$$\text{Volume fraction of fuel element in fuel cell} = \frac{\text{area fuel element}}{\text{area fuel cell}} = 0.289 \quad (110)$$

$$\text{Volume fraction of } D_2O \text{ surrounding fuel element in fuel cell} = 0.711 \quad (111)$$

Number density for atoms of U-235

$$N(\text{U-235}) = (\text{volume fraction of fuel element in fuel cell}) \times (\text{number density for atoms of U-235 in smeared fuel element}) \quad (112)$$

$$= (0.289)(0.000105)(10^{24})$$

$$= (0.0000303)(10^{24}) \frac{\text{atoms U-235}}{cm^3 \text{ homogenized fuel cell}}$$

Number density for atoms of U-238

$$N(\text{U-238}) = (0.289)(0.00000759)(10^{24}) \tag{113}$$

$$= (0.00000219)(10^{24}) \frac{\text{atoms U-238}}{\text{cm}^3 \text{ homogenized fuel cell}}$$

Number density for atoms of Al

$$N(\text{Al}) = (0.289)(0.0197)(10^{24}) \tag{114}$$

$$= (0.00569)(10^{24}) \frac{\text{atoms Al}}{\text{cm}^3 \text{ homogenized fuel cell}}$$

Number density for atoms of D

$$N(\text{D}) = \left[(0.289)(0.0445) + (0.711)(0.06628)\right](10^{24}) \tag{115}$$

$$= (0.0600)(10^{24}) \frac{\text{atoms D}}{\text{cm}^3 \text{ homogenized fuel cell}}$$

Number density for atoms of H

$$N(\text{H}) = \left[(0.289)(0.00011) + (0.711)(0.00017)\right](10^{24}) \tag{116}$$

$$= (0.00015)(10^{24}) \frac{\text{atoms H}}{\text{cm}^3 \text{ homogenized fuel cell}}$$

Number density for atoms of O

$$N(\text{O}) = \left[(0.289)(0.0223) + (0.711)(0.03322)\right](10^{24}) \tag{117}$$

$$= (0.0301)(10^{24}) \frac{\text{atoms O}}{\text{cm}^3 \text{ homogenized fuel cell}}$$

A summary of the number densities used to determine the two-group coefficients is given in Table 13.

Coefficient Generation

Fast Group Coefficients

The fast group coefficients were generated using COMBO[51] (a multi-group spectrum code for the Philco 2000). The primary purpose of this code is to generate consistent polygroup constants for use in space-dependent diffusion theory calculations. A fundamental mode solution of the transport equation in the B_1 approximation is used to obtain the 68-group spectrum. Neutron moderation by hydrogen or deuterium is described by the Greuling-Goertzel approximation; the Fermi Age approximation is used for all other elements.

The low energy cut-off (boundary between "fast" and "thermal" groups) used for the results reported was 0.79 electron volts. Previous calculations performed using essentially the same number densities showed little variation in the results between using 0.68 electron volts or 0.87 electron volts as the low energy cut-off. The temperature used for each calculation was 72°F.

Each problem required as input one set of atom densities to describe the composition under consideration. The calculations performed were based upon a one-region, one-dimensional model. An input buckling was used to account for the effect of leakage. The source spectrum to be

Table 13. Number Densities, in Units of 10^{24} Atoms/cm^3, for Coefficient Generation

Component	Reflector (Graphite)	Moderator (99.77 wt % D_2O)	Smeared Fuel Element (3" × 3")	Homogenized Fuel Cell (Area = 201 cm^2)
Al	0.0	0.0	0.0197	0.00569
C	0.0852	0.0	0.0	0.0
D	0.0	0.06628	0.0445	0.0600
H	0.0	0.00017	0.00011	0.00015
O	0.0	0.03322	0.0223	0.0301
U-235	0.0	0.0	0.000105	0.0000303
U-238	0.0	0.0	0.00000759	0.00000219

used also had to be indicated.[52] No broad group self-shielding factors were used, i.e., a spatially flat flux was assumed in all COMBO problems. Resonance absorption in COMBO is treated by either the narrow resonance or narrow resonance infinite mass approximation. For the GTRR, both the U-235 and U-238 are essentially infinitely dilute.

The following tabulation details the input used to determine the fast coefficients for each composition of interest.

Smeared fuel element

Atom densities (Table 13)

$B^2 = 10^{-50}$

Source spectrum = fission source spectrum

D_2O in core surrounding smeared fuel element

Atom densities (Table 13)

$B^2 = 10^{-50}$

Source spectrum = fission source spectrum

Homogenized fuel cell

Atom densities (Table 13)

$B^2 = 0.862 \times 10^{-2}$ based upon core radius $\approx$ 26 cm

Source spectrum = fission source spectrum

D_2O moderator surrounding the core

Atom densities (Table 13)

$B^2 = 0.5 \times 10^{-2}$

Source spectrum = leakage source spectrum resulting from the homogenized fuel cell calculation

Graphite reflector surrounding the D_2O moderator

Atom densities (Table 13)

$B^2 = 10^{-50}$

Source spectrum = leakage source spectrum resulting from the D_2O moderator calculation

Thermal Group Coefficients

The thermal group coefficients were generated using a modified version of THERMOS[53] (a thermalization transport theory code for reactor lattice calculations). The general purpose of THERMOS[54] is to predict thermal neutron reaction rates for a given lattice configuration. THERMOS solves the isotropic integral transport equation for the space and energy (30 groups) dependence of the flux in a lattice cell. Transport kernels for slab or cylindrical configurations are computed within the code. Energy exchange kernels [$\Sigma_{so}(E' \rightarrow E)$] may be supplied as input or generated within the code using the Brown-St. John Model. The particular kernels used for these calculations were as follows:

1. Nelkin-Honeck Model for bound deuterium
2. Nelkin Model for bound hydrogen
3. Free gas kernel [constant σ_s(thermal), physical mass] for all other elements.

A three-region, one-dimensional THERMOS calculation was used to determine the thermal core parameters. The cylindrical approximation of a fuel cell (Figure 49) was used to determine the extent of region 1 (the fuel region) and region 2 (the D_2O surrounding the fuel). That is, the radius (r = 1.69 inches) of a circle whose area is equal to nine square

inches (area of the smeared fuel element) was used to define region 1. The radius (r = 3.15 inches) of a circle whose area was equal to 31.2 square inches (area of the hexagonal fuel cell) was used to define region 2. The third region, a pure scattering medium having a thickness of three centimeters (Σ_s = 1), was used to surround the D_2O in order to return the neutrons isotropically instead of using the conventional reflective boundary condition[55] at the outer edge of the D_2O region. Results from the computation provided thermal core parameters for both situations of interest. It provided thermal coefficients for the smeared fuel element and a separate set of thermal coefficients for the D_2O surrounding the fuel. It also flux weighted the respective coefficients and thus provided as an additional part of the output the homogenized cell coefficients.

The geometrical input specifications needed for the determination of the thermal-group coefficients for the heavy-water moderator surrounding the core were as follows:

1. cylindrical geometry (no leakage)
2. radius = 10 cm (ten space points).

Similar input specifications were used to determine the coefficients for the graphite reflector surrounding the heavy-water moderator. All THERMOS computations were based upon a temperature of 72°F.

The "static" coefficients for a two-group analysis of the GTRR, obtained from using COMBO and THERMOS, are given in Table 14.

Table 14. "Static" Coefficients for Two-Group Analysis of the GTRR

	D_1 (cm)	D_2 (cm)	Σ_1^a (cm^{-1})	Σ_2^a (cm^{-1})	$\Sigma_{1\to2}^s$ (cm^{-1})	$\nu_1 \Sigma_1^f$ (cm^{-1})	$\nu_2 \Sigma_2^f$ (cm^{-1})
Smeared Fuel Element	1.585	1.021	2.785×10^{-3}	5.052×10^{-2}	6.335×10^{-3}	3.794×10^{-3}	9.768×10^{-2}
D_2O Moderator (Core)	1.329	0.856	5.617×10^{-5}	7.220×10^{-5}	1.193×10^{-2}		
Homogenized Fuel Cell (Flux Weighted)	1.364	0.895	7.319×10^{-4}	1.199×10^{-2}	6.377×10^{-3}	9.199×10^{-4}	2.308×10^{-2}
D_2O Reflector	1.267	0.799	3.669×10^{-5}	8.482×10^{-5}	1.648×10^{-2}		
Graphite Reflector	0.936	0.832	1.236×10^{-5}	2.546×10^{-4}	9.204×10^{-3}		

APPENDIX B

"KINETIC" CROSS SECTION GENERATION FOR COMPLEX SOURCE PROBLEM

In order to solve the two-dimensional complex source problem by using the statics code EXTERMINATOR, it was necessary to generate the "kinetic" cross sections needed as input. The term "kinetic" is used because of the dependence of the fictitious cross sections upon omega, the frequency of the external source. The equations defining the two-energy, two-dimensional "kinetic" cross sections are given in Chapter V, equations 67 through 84. KISEC, a computer program in the ALGOL language for the Burroughs B-5500, was written to perform the calculations for the multienergy, two-dimensional equations equivalent to equations 67 through 84.

The listing of the program KISEC is included for reference on the following pages.

```
%                                                                       0
%                                                                      10
%                              KISEC                                   20
%                                                                      30
%                                                                      40
% PROGRAM TO COMPUTE KINETIC CROSS SECTIONS TO BE USED AS INPUT FOR     50
% "EXTERMINATOR" WHEN SOLVING COMPLEX SOURCE TYPE PROBLEM               60
%                                                                      70
% RESTRICTIONS IN THE PROGRAM                                          80
%   NOC = NUMBER OF CASES I.E. NUMBER OF ANGULAR VELOCITIES ≤ 35       90
%   NOR = NUMBER OF REGIONS ≤ 10                                      100
%   GPS = NUMBER OF ENERGY GROUPS ≤ 10                                110
%   NPC = NUMBER OF PRECURSORS IN ANY REGION ≤ 20                     120
%                                                                     130
BEGIN                                                                140
INTEGER NOC,NOR, GPS, I,DBLNOGPS,J,K,L, DELT, T;                     150
INTEGER ARRAY NPC [0:10] ;                                           160
ALPHA ARRAY TITLE[0:12];                                             170
REAL ARRAY SIGTOT, DIFCOEF, SIGMABS, NUSIGFIS, BZSQD, VEL[0:10,0:10];180
REAL ARRAY CHI,  ALPHA[0:10,0:10], BETAI, LAMBDAI[0:20,0:10];        190
REAL ARRAY OMEGA[0:35];                                              200
REAL ARRAY SIGTRANSFER[0:10,0:10,0:10], BETA, SUML, SUMW [0:10];     210
REAL ARRAY KDIFCOF, KSIGMABS [0:20,0:10], KSIGTRANSFER[0:20,0:20,0:10] ;220
REAL ARRAY KSIGTOT[0:20,0:10];                                       230
REAL ARRAY DBZSIGTOT[0:20,0:10];                                     240
REAL ARRAY DIFKSIGTOT,DIFKSIGMABS[0:20,0:10];                        250
REAL ARRAY DIFKSIGTRANSFER[0:20,0:20,0:10];                          260
LABEL  L1, L2, L3, L4 ;                                              270
FILE     CARD  (2,10);                                               280
FILE OUT PRINT 6(2,15);                                              290
FORMAT FMT0 (6E14.6);                                                300
FORMAT FMT1 (12A6);                                                  310
FORMAT FMT2 (6I12);                                                  320
FORMAT FMT3 (6R12.5);                                                330
FORMAT FMT4(//"DIFFUSION COEFFICIENT FOR GROUP 1 TO GROUP ",I2/);    340
FORMAT FMT5 (///" INPUT VALUES FOR REGION ",I2//);                   350
FORMAT FMT6 (/"MACROSCOPIC ABSORPTION CROSS SECTION FOR GROUP 1 TO GROUP 360
 ",I2/);                                                             370
FORMAT FMT7 (/"NU TIMES MACROSCOPIC FISSION CROSS SECTION FOR GROUP 1 TO 380
 GROUP ",I2/);                                                       390
FORMAT FMT8 (/"MACROSCOPIC SCATTER OR TRANSFER CROSS SECTION FROM GROUP 400
J TO GROUP T ( T VARIES HORIZONTALLY, J VARIES VERTICALLY)"/);       410
FORMAT FMT9 (/"ENERGY DEPENDENT BUCKLING ( BZ SQUARED )"/);          420
FORMAT FMT10 (/"AVG. VELOCITY FOR GROUP 1 TO GROUP ",I2/);           430
FORMAT FMT11 (/"FRACTION OF FISSION NEUTRONS BORN IN GROUP 1 TO GROUP ", 440
I2/);                                                                450
FORMAT FMT12 (/"FRACTION OF DELAYED NEUTRONS BORN IN GROUP 1 TO GROUP ", 460
I2/);                                                                470
FORMAT FMT13 (" BETA[I],LAMBDA[I] FOR I = 1 TO ",I2/);               480
FORMAT FMT14 (/"DIFFUSION COEFFICIENTS FOR GROUP 1 TO GROUP ",I2/);  490
FORMAT FMT15 (//X8,"KINETIC COEFFICIENTS FOR REGION ",I2,"   OMEGA = " 500
  R14.7," RADIANS PER SEC"/ );                                       510
FORMAT FMT16 (/" KINETIC MACROSCOPIC ABSORPTION CROSS SECTION FOR GROUP 520
1 TO GROUP ",I2);                                                    530
FORMAT FMT17 (/" KINETIC MACROSCOPIC SCATTER OR TRANSFER CROSS SECTION F 540
ROM GROUP J TO GROUP T");                                            550
FORMAT FMT18 ("     T VARIES HORIZONTALLY AND J VARIES VERTICALLY" );560
FORMAT FMT19 (//"VALUES OF ANGULAR VELOCITIES FOR WHICH KINETIC COEFFICI 570
ENTS WILL BE COMPUTED"/);                                            580
FORMAT FMT20 ("     IF USING DIFFUSION EQUATION "/);                 590
FORMAT FMT21 ("     IF USING TELEGRAPHERS EQUATION "/);              600
LIST LST1 (FOR I=1 STEP 1 UNTIL 12 DO TITLE[I]);                     610
```

```
LIST LST2 (NOC,NOR,GPS);   % NUMBER OF OMEGAS,REGIONS,ENERGY GROUPS          620
LIST LST3 ( FOR J←1 STEP 1 UNTIL GPS DO DIFCOEF[J,K]);                       630
LIST LST4 ( FOR J←1 STEP 1 UNTIL GPS DO SIGMABS[J,K]);                       640
LIST LST5 ( FOR J←1 STEP 1 UNTIL GPS DO NUSIGFIS[J,K]);                      650
LIST LST6 (FOR J←1 STEP 1 UNTIL GPS DO                                       660
           FOR T←1 STEP 1 UNTIL GPS DO SIGTRANSFER[J,T,K]);                  670
LIST LST7 ( FOR J←1 STEP 1 UNTIL GPS DO BZSQD[J,K]);                         680
LIST LST8 ( FOR J←1 STEP 1 UNTIL GPS DO VEL[J,K]);                           690
LIST LST9 ( FOR J←1 STEP 1 UNTIL GPS DO CHI[J,K]);                           700
LIST LST10 (FOR J←1 STEP 1 UNTIL GPS DO ALFHA[J,K]);                         710
LIST LST11 ( NPC[K]);                                                        720
LIST LST12 (FOR I←1 STEP 1 UNTIL NPC[K] DO [BETAI[I,K],LAMBDAI[I,K]]);       730
LIST LST13 (GPS);                                                            740
LIST LST14 ( K, OMEGA[L]);                                                   750
LIST LST15 ( FOR T←1 STEP 1 UNTIL GPS DO SIGTRANSFER[J,T,K]);                760
LIST LST16 (DBLNOGPS);                                                       770
LIST LST17 (FOR J←1 STEP 1 UNTIL DBLNOGPS DO KDIFCOF[J,K]);                  780
LIST LST18 (FOR T←1 STEP 1 UNTIL DBLNOGPS DO KSIGTRANSFER[J,T,K]);           790
LIST LST19 (FOR J←1 STEP 1 UNTIL DBLNOGPS DO KSIGMABS[J,K]);                 800
LIST LST20 (FOR L←1 STEP 1 UNTIL NOC DO OMEGA[L]);                           810
LIST LST21 (K);                                                              820
LIST LST22 (FOR J←1 STEP 1 UNTIL DBLNOGPS DO DIFKSIGMABS[J,K]);              830
LIST LST23 (FOR T←1 STEP 1 UNTIL DBLNOGPS DO DIFKSIGTRANSFER[J,T,K]);        840
%                                                                            850
%     START OF PROGRAM                                                       860
%                                                                            870
%     READ INPUT DATA                                                        880
%                                                                            890
WRITE(PRINT  [NO]) ; %PRINT FILE-ID GOES IN COLS. 7-13. PUT AFTER DECL.      900
READ (CARD,FMT1,LST1);     % TITLE                                           910
READ (CARD,FMT2,LST2);     % NUMBER OF OMEGAS,REGIONS,ENERGY GROUPS          920
NOR ← NOR;                                                                   930
READ (CARD,FMT3,LST20);    % VALUES OF ANGULAR VELOCITIES (OMEGAS)           940
FOR K←1 STEP 1 UNTIL NOR DO                                                  950
BEGIN                                                                        960
READ (CARD,FMT3,LST3);     % DIFFUSION COEFFICIENTS                          970
READ (CARD,FMT3,LST4);     % MACROSCOPIC ABSORPTION CROSS SECTIONS           980
READ (CARD,FMT3,LST5);     % NU TIMES MACROSCOPIC FISSION CROSS SECTION      990
READ (CARD,FMT3,LST6);     % MACROSCOPIC SCATTER OR TRANSFER CROSS SECT     1000
READ (CARD,FMT3,LST7);     % ENERGY DEPENDENT BUCKLING (BZ SQUARED)         1010
READ (CARD,FMT3,LST8);     % AVG. VELOCITY FOR EACH ENERGY GROUP            1020
READ (CARD,FMT3,LST9);     % FRACT OF FIS NEUTS BORN IN ENERGY[J],CHI[J]    1030
READ (CARD,FMT3,LST10);    % FRACT OF DLAY NEUT BRN IN NRG[J], ALFHA[J]     1040
READ (CARD,FMT2,LST11);    % NUMBER OF PRECURSORS                           1050
K ← K;                                                                       1060
NPC[K] ← NPC[K];                                                             1070
IF NPC[K] = 0 THEN GO TO L1;                                                 1080
READ (CARD,FMT3,LST12);    % BETA[I]S AND LAMBDA[I]S                        1090
L1:                                                                          1100
END;                                                                         1110
%                                                                            1120
CLOSE (CARD, RELEASE);                                                       1130
%     PRINT THE INPUT                                                        1140
%                                                                            1150
WRITE (PRINT[PAGE]);                                                         1160
WRITE (PRINT,FMT1,LST1);     % TITLE                                         1170
WRITE (PRINT,FMT19);                                                         1180
WRITE (PRINT,FMT0,LST20);  % VALUES OF ANGULAR VELOCITIES (OMEGAS)          1190
FOR K←1 STEP 1 UNTIL NOR DO                                                  1200
BEGIN                                                                        1210
WRITE (PRINT,FMT5,LST21);    % REGION NUMBER                                 1220
WRITE (PRINT,FMT4,LST13);    %                                             1230
```

```
WRITE (PRINT,FMT0,LST3);      % DIFFUSION COEFFICIENTS                          1240
WRITE (PRINT,FMT6,LST13);     %                                                 1250
WRITE (PRINT,FMT0,LST4);      % MACROSCOPIC ABSORPTION CROSS SECTIONS           1260
WRITE (PRINT,FMT7,LST13);                                                       1270
WRITE (PRINT,FMT0,LST5);    % NU TIMES MACROSCOPIC FISSION CROSS SECTION        1280
WRITE (PRINT,FMT8);                                                             1290
FOR J:=1 STEP 1 UNTIL GPS DO                                                    1300
WRITE (PRINT,FMT0,LST15);   % MACROSCOPIC SCATTER OR TRANSFER CROSS SECT       1310
WRITE (PRINT,FMT9);                                                             1320
WRITE (PRINT,FMT0,LST7);    % ENERGY DEPENDENT BUCKLING (BZ SQUARED)          1330
WRITE (PRINT,FMT10,LST13);                                                      1340
WRITE (PRINT,FMT0,LST8);    % AVG. VELOCITY FOR EACH ENERGY GROUP             1350
WRITE (PRINT,FMT11,LST13);                                                      1360
WRITE (PRINT,FMT3,LST9);    % FRACT OF FIS NEUTS BORN IN ENERGY[J],CHI[J]     1370
WRITE (PRINT,FMT12,LST13);                                                      1380
WRITE (PRINT,FMT3,LST10);   % FRACT OF DLAY NEUT BRN IN NRG[J], ALFHA[J]      1390
WRITE (PRINT,FMT13,LST11);                                                      1400
IF NPC[K] =0 THEN GO TO L2;                                                     1410
WRITE (PRINT,FMT0,LST12);   % BETA[I]S AND LAMBDA[I]S                         1420
L2:                                                                             1430
END;                                                                            1440
%       KINETIC COEFFICIENT COMPUTATIONS                                        1450
   FOR L:=1 STEP 1 UNTIL NOC DO                                                 1460
   BEGIN                                                                        1470
     FOR K:=1 STEP 1 UNTIL NOR DO                                               1480
     BEGIN                                                                      1490
       BETA[K]:= SUML[K]:= SUMW[K]:= 0 ;                                        1500
       IF NPC[K] = 0 THEN GO TO L3 ;                                            1510
       FOR I:=1 STEP 1 UNTIL NPC[K] DO                                          1520
       BEGIN                                                                    1530
         SUML[K] := SUML[K] + (((LAMBDAI[I,K]*2) * BETAI[I,K]) /                1540
                   ((OMEGA[L]*2) + (LAMBDAI[I,K]*2)));                          1550
         SUMW[K] := SUMW[K] + ((OMEGA[L] * LAMBDAI[I,K] * BETAI[I,K])/          1560
                   ((OMEGA[L]*2) + (LAMBDAI[I,K]*2)));                          1570
         BETA[K] := BETA[K] + BETAI[I,K];                                       1580
       END;                                                                     1590
L3:    FOR J:=1 STEP 1 UNTIL GPS DO                                            1600
       BEGIN                                                                    1610
         KDIFCOF[2*J-1,K] := KDIFCOF[2*J,K] := DIFCOEF[J,K];                    1620
         SIGTOT[J,K] := SIGMABS[J,K];                                           1630
         FOR T:=1 STEP 1 UNTIL GPS DO                                           1640
           SIGTOT[J,K] := SIGTOT[J,K] + SIGTRANSFER[J,T,K];                     1650
         DBZSIGTOT[J,K] := DIFCOEF[J,K] * BZSQD[J,K] + SIGTOT[J,K];             1660
         KSIGTOT[2*J-1,K] := KSIGTOT[2*J,K] := DBZSIGTOT[J,K] -                 1670
           ((3*DIFCOEF[J,K]*(OMEGA[L]*2)) / (VEL[J,K]*2)) ;                     1680
       DIFKSIGTOT[2*J-1,K]:= DIFKSIGTOT[2*J,K] := DBZSIGTOT[J,K];               1690
         KSIGMABS[2*J-1,K] := KSIGMABS[2*J,K] := KSIGTOT[2*J,K];                1700
       DIFKSIGMABS[2*J-1,K] := DIFKSIGMABS[2*J,K] := DIFKSIGTOT[2*J,K];         1710
         FOR T:=1 STEP 1 UNTIL GPS DO                                           1720
         BEGIN                                                                  1730
           KSIGTRANSFER[2*J-1,2*T-1,K] := (((CHI[T,K] * (1 - BETA[K]))          1740
             + (ALFHA[T,K] * SUML[K])) * NUSIGFIS[J,K])                         1750
             + SIGTRANSFER[J,T,K] ;                                             1760
           KSIGTRANSFER[2*J,2*T,K] := KSIGTRANSFER[2*J-1,2*T-1,K];              1770
         DIFKSIGTRANSFER[2*J,2*T,K] := KSIGTRANSFER[2*J,2*T,K];                 1780
         DIFKSIGTRANSFER[2*J-1,2*T-1,K] := KSIGTRANSFER[2*J-1,2*T-1,K];         1790
           IF T = J THEN DELT := 1 ELSE DELT := 0 ;                             1800
           KSIGTRANSFER[2*J-1,2*T,K] := (( -1 * ALFHA[T,K] * SUMW[K])           1810
             * NUSIGFIS[J,K]) - (OMEGA[L] / VEL[J,K]) * (1 +( 3                 1820
             * SIGTOT[J,K] * DIFCOEF[J,K])) * DELT ;                            1830
         DIFKSIGTRANSFER[2*J-1,2*T,K] := ((-1 * ALFHA[T,K] * SUMW[K])           1840
         * NUSIGFIS[J,K]) -((OMEGA[L] / VEL[J,K]) * DELT);                      1850
```

```
          KSIGTRANSFER[2×J,2×T-1,K] + - KSIGTRANSFER[2×J-1,2×T,K]};          1860
        DIFKSIGTRANSFER[2×J,2×T-1,K] + - DIFKSIGTRANSFER[2×J-1,2×T,K]};      1870
          KSIGMABS[2×J-1,K] + KSIGMABS[2×J-1,K]                              1880
            - KSIGTRANSFER[2×J-1,2×T-1,K] - KSIGTRANSFER[2×J-1,2×T,K]};      1890
        DIFKSIGMABS[2×J-1,K] +DIFKSIGMABS[2×J-1,K]                           1900
        - DIFKSIGTRANSFER[2×J-1,2×T-1,K]-DIFKSIGTRANSFER[2×J-1,2×T,K]};      1910
          KSIGMABS[2×J,K] + KSIGMABS[2×J,K]                                  1920
            - KSIGTRANSFER[2×J,2×T,K] - KSIGTRANSFER[2×J,2×T-1,K]};          1930
        DIFKSIGMABS[2×J,K] + DIFKSIGMABS[2×J,K]                              1940
        - DIFKSIGTRANSFER[2×J,2×T,K] - DIFKSIGTRANSFER[2×J,2×T-1,K]};        1950
        END};                                                                1960
      END};                                                                  1970
    END};                                                                    1980
DBLNOGPS ← 2 × GPS };                                                        1990
%                                                                            2000
%     PRINT THE OUTPUT                                                       2010
%                                                                            2020
WRITE (PRINT[PAGE])};                                                        2030
WRITE (PRINT,FMT1,LST1)};   % TITLE                                          2040
FOR K ←1 STEP 1 UNTIL NOR DO                                                 2050
BEGIN                                                                        2060
WRITE (PRINT,FMT15,LST14)};                                                  2070
WRITE (PRINT,FMT14,LST16)}; %                                                2080
WRITE (PRINT,FMTO,LST17)}; % DIFFUSION COEFFS FOR COMPLEX SOURCE PROB        2090
WRITE (PRINT,FMT16,LST16)};                                                  2100
WRITE (PRINT,FMT21)};                                                        2110
WRITE (PRINT,FMTO,LST19)};  % KINETIC ABSORPTION CROSS SECTIONS              2120
WRITE (PRINT,FMT16,LST16)};                                                  2130
WRITE (PRINT,FMT20)};                                                        2140
WRITE (PRINT,FMTO,LST22)};% KINETIC ABSORPTION CROSS SECTIONS DIFF THEORY    2150
WRITE (PRINT,FMT17)};                                                        2160
WRITE (PRINT,FMT18)};                                                        2170
WRITE (PRINT,FMT21)};                                                        2180
FOR J←1 STEP 1 UNTIL DBLNOGPS DO                                             2190
WRITE (PRINT,FMTO,LST18)};  % KINETIC TRANSFER CROSS SECTIONS                2200
WRITE (PRINT,FMT17)};                                                        2210
WRITE (PRINT,FMT18)};                                                        2220
WRITE (PRINT,FMT20)};                                                        2230
FOR J←1 STEP 1 UNTIL DBLNOGPS DO                                             2240
WRITE (PRINT,FMTO,LST23)};% KINETIC TRANSFER CROSS SECTIONS DIFF THEORY      2250
END};                                                                        2260
  END};                                                                      2270
END.                                                                         2280
```

APPENDIX C

DATA COLLECTION, REDUCTION, AND ANALYSIS

Data Collection

Collection and storage of the experimental data were accomplished by using the 400-channel analyzer in the multiscaler mode. The dwell time per channel was set by adjusting the output from the channel advance timing oscillator so that 400 channels of data were obtained for each revolution of the pile oscillator drive shaft. This is not meant to imply that the time for one revolution of the drive shaft was divided into 400 equal time increments and data collected in each one of them. Synchronization of the pile oscillator with a free-running timing oscillator was not possible because of the variations in the motor speed. The timing oscillator (with the reset signal option, as used in this experiment) was free-running only between reference pulses. Each reference pulse reset the timer, simultaneously synchronizing the multiscaler and associated electronics to the pile oscillator. Thus, the dwell time per channel was adjusted to allow 400 channels of data to be stored before the next reference pulse was received. This time interval per channel was not arbitrary. Due to the design characteristics of the multiscaler, the "ready accumulate command" and the "accumulate command" for channel zero could not be accommodated simultaneously. This resulted in an interval exactly one dwell time in length, called the "ready accumulate mode," during which no data were stored. One further consideration was necessary while adjust-

ing the dwell advance timing oscillator. A design feature of the TMC Model 404 multiscaler required that in order to execute the "ready accumulate" command (needed to begin a new data collection cycle), the multiscaler had to be in the "stop" mode. Taking into consideration the variations of the motor speed, the dwell time per channel was adjusted so that approximately three-fourths of one dwell time followed the last channel of data collection. During this time, the multiscaler was in the "stop" mode and thus prepared to receive the next "ready accumulate" command. The various modes of operation of the multiscaler were distinguishable by monitoring the voltage level on the dwell advance jack, J-105, using an oscilloscope in the delayed sweep mode of operation. Associated with each channel was a switching time equal to 34 microseconds. Channel zero (the first data collection channel) is an exception, having only a 17 microsecond switching time. A timing diagram of the data collection sequence is shown in Figure 51.

Data Reduction and Analysis

Upon completion of a run, the data stored in the memory of the multiscaler were punched serially on paper tape. Processing of the data was implemented by using the Burroughs B-5500 computer at Georgia Tech. The computer was not equipped with a paper tape input reader. Therefore, an IBM tape-to-card printing punch was used to convert the information from the paper tape to punched cards, a permissible input medium for the B-5500.

DRAHA, the computer program used for analyzing the experimental data, has the following input requirements:

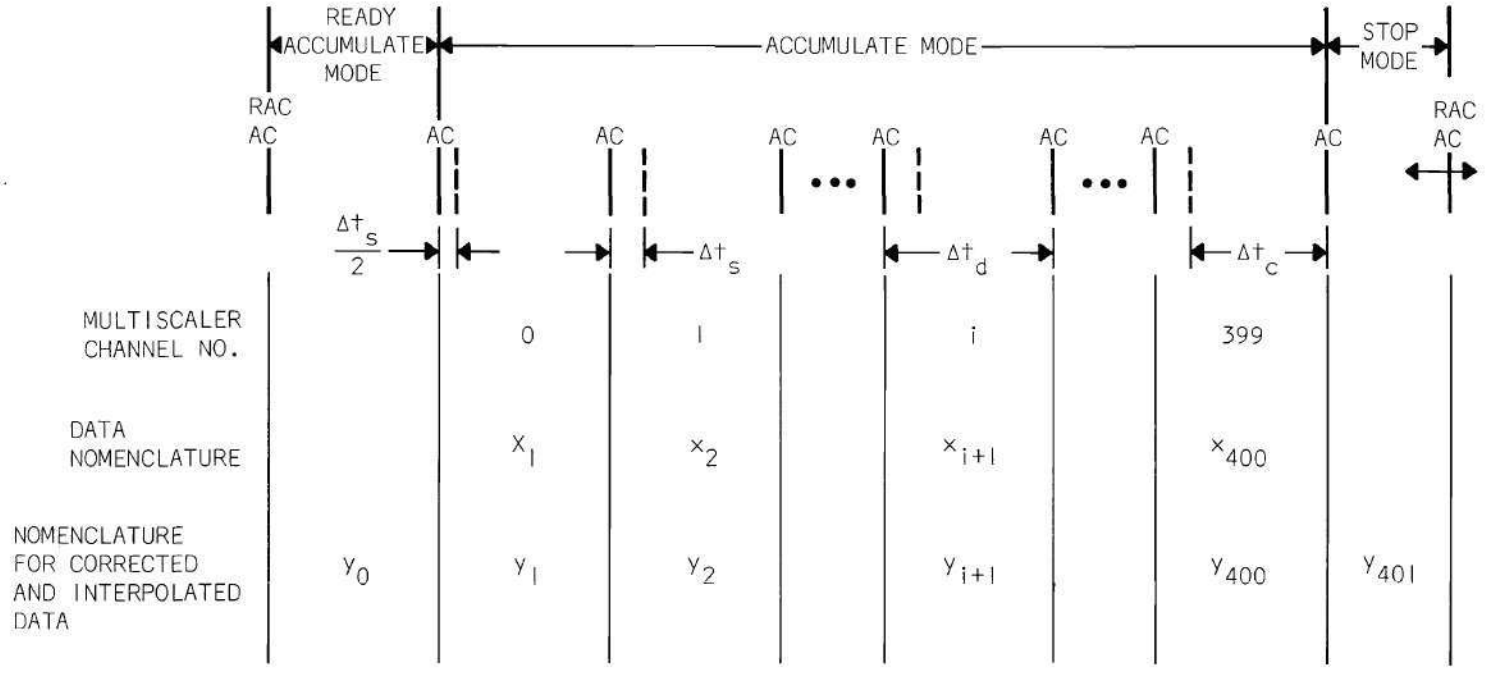

RAC = "READY ACCUMULATE COMMAND" which originates when breaker points separate

AC = "ACCUMULATE COMMAND" or "ADVANCE COMMAND" output of the channel advance timing oscillator

Δt_s = switching time per channel for channels 1 through 399
= 34μ sec.

Δt_d = dwell time per channel per pass (value depends upon frequency of pile oscillator)

Δt_c = data collection time per channel per pass
= Δt_d -34μ sec for channels 1 to 399
= Δt_d -17μ sec for channel 0

Figure 51. Data Collection Timing Sequence and Associated Data Reduction and Analysis Nomenclature

1. the number of data collection runs to be processed
2. the print control indicator 1 or 2
3. the dead time of the detector-multiscaler system, T_d
4. the total number of data points
5. the maximum number of harmonics to be considered, M
6. the number of cycles of equally spaced data points, 1 or 2
7. the total number of drive shaft revolutions, N
8. the data collection time per channel per pass, Δt_c
9. the amount of "overflow" during the experimental data collection
10. the experimental data (counts per channel).

The following discussion not only details the equations solved by DRAHA, but also explains the basis for the calculations performed.

Provision was made in the code to add a constant to all the data if necessary. This condition existed if the total counts per channel exceeded one million (the storage capacity per channel for the multiscaler). "Overflow," as this is called, resulted in the least significant digits being retained in the memory of the multiscaler. Thus, for example, if the total count accumulated in a particular channel was 1,522,503, the actual number retained in the memory was 522,503. For the program to process the proper number required one million to be added to the number obtained from the original input data. "Overflow" was established in a straightforward manner during this experiment since the count rate on the detector remained below 250,000 counts per second. As an illustration, consider the pile oscillator operating at one cycle every four seconds. Thus, a total of approximately one million counts would be stored in the 400 channels or 2,500 counts per channel per revolution. Hence, to accumu-

late one million counts per channel would require 1600 seconds. Therefore, by visual monitoring of the multiscaler, an overflow condition could be established. Although this option was available, it was never needed. No provision was made to add one million to a few select channels around the peaks which could overflow while the other channels did not.

As shown in Figure 51, channel zero, corresponding to the first datum point, collects data 17 microseconds longer than any other channel. The equation

$$x_1 = X_1 \left(\frac{\Delta t_c}{\Delta t_c + 17 \times 10^{-6}} \right) \tag{118}$$

where Δt_c is in seconds

was used to correct the data in channel zero for the different channel switching time.

Further computations were performed to correct the experimental data for the lost counts due to the dead time of the detector-analyzer system. The dead time of the detector-analyzer system was 530 nanoseconds, as determined by Graham.[56] The conventional formula for correcting for lost counts was employed.

$$y_i = \frac{x_i}{1 - \left(\frac{x_i}{N \times \Delta t_c} \right) T_d} \tag{119}$$

Here the expression $\left(\frac{x_i}{N \times \Delta t_c} \right)$ was used to approximate the average count

rate during data collection. This equation produces satisfactory results provided the correction is of the order of ten percent or less. Under this restriction, the experimental technique used resulted in counting rates typically of the order of 200,000 counts per second. Using 530 nanoseconds for the system dead time, the magnitude of the lost count correction can be estimated as follows

$$y_i = \frac{x_i}{1 - (CR \times T_d)} \tag{120}$$

where CR = count rate (counts/sec)

$$y_i = \frac{x_i}{1 - (2 \times 10^5)(5.3 \times 10^{-7})}$$

$$y_i \approx 1.12\, x_i$$

This restriction on the count rate could be met for positions 2, 5, and 6, as shown in Figure 3, by adjusting the power level. For positions 1, 3, and 4, as shown in Figure 3, the count rate had to be reduced, by lowering the linear amplifier gain, to remain below 200,000 counts per second, even with the reactor at the smallest possible power level.

Corrections were made to account for the times during a cycle when no data were being collected, i.e., at the beginning and end of each cycle. Linear interpolation was assumed to be a valid technique to generate the two missing points. Justification for this assumption was based upon two considerations. Each pile oscillator revolution was equivalent to two data cycles, i.e., 720 degrees. Hence, the points were approximately 1-3/4 de-

grees apart. This, coupled with the statistical uncertainty of each datum point, precluded the use of a higher order approximation. Figures 52, 53, and 54, in which every other datum point is plotted, provides a visible picture of why any higher order approximation would not be justified. The first and last data points collected were not used for the linear interpolation. This decision was based upon the various operating anomalies which could and did happen during the course of data collection to affect the contents of the first and last channels. The first channel was affected by the performance of the breaker points. The last channel could conceivably be shortened if the breaker points were separated while data were being stored in the last channel. This condition could exist only if excessive drifting of the channel advance timing oscillator went unnoticed. The equations

$$y_0 = y_2 - \frac{2}{5}(y_2 - y_{399}) \tag{121}$$

and

$$y_{401} = y_{399} - \frac{2}{5}(y_2 - y_{399}) \tag{122}$$

were used to generate the missing end points. With the above corrections and additions, the resulting set of data represented the response of the reactor to cyclic variations in absorption.

The following discussion develops the equations used to fit a finite trigonometric sum to the set of values (i, y_i) over the range $i = 0$ to 401, in which the values of y are periodic with period 201. However, due to the existence of the "stop" mode, which is not one full channel width, the data are not exactly periodic. Therefore, in order to justify the sys-

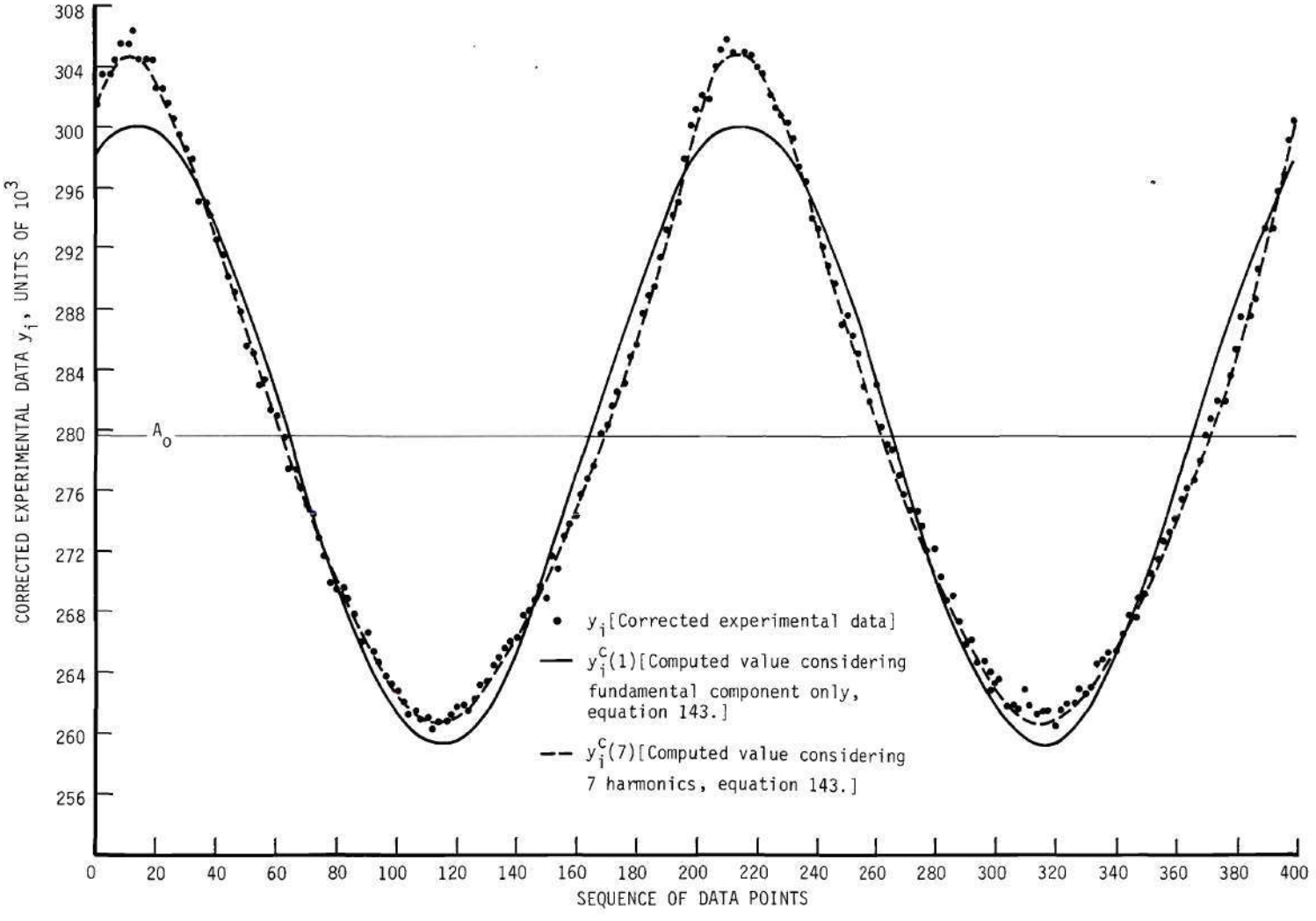

Figure 52. Corrected Experimental Data and Results of Harmonic Analysis -- Detector Position 6 and Pile Oscillator Frequency of 0.498 Cycles Per Second

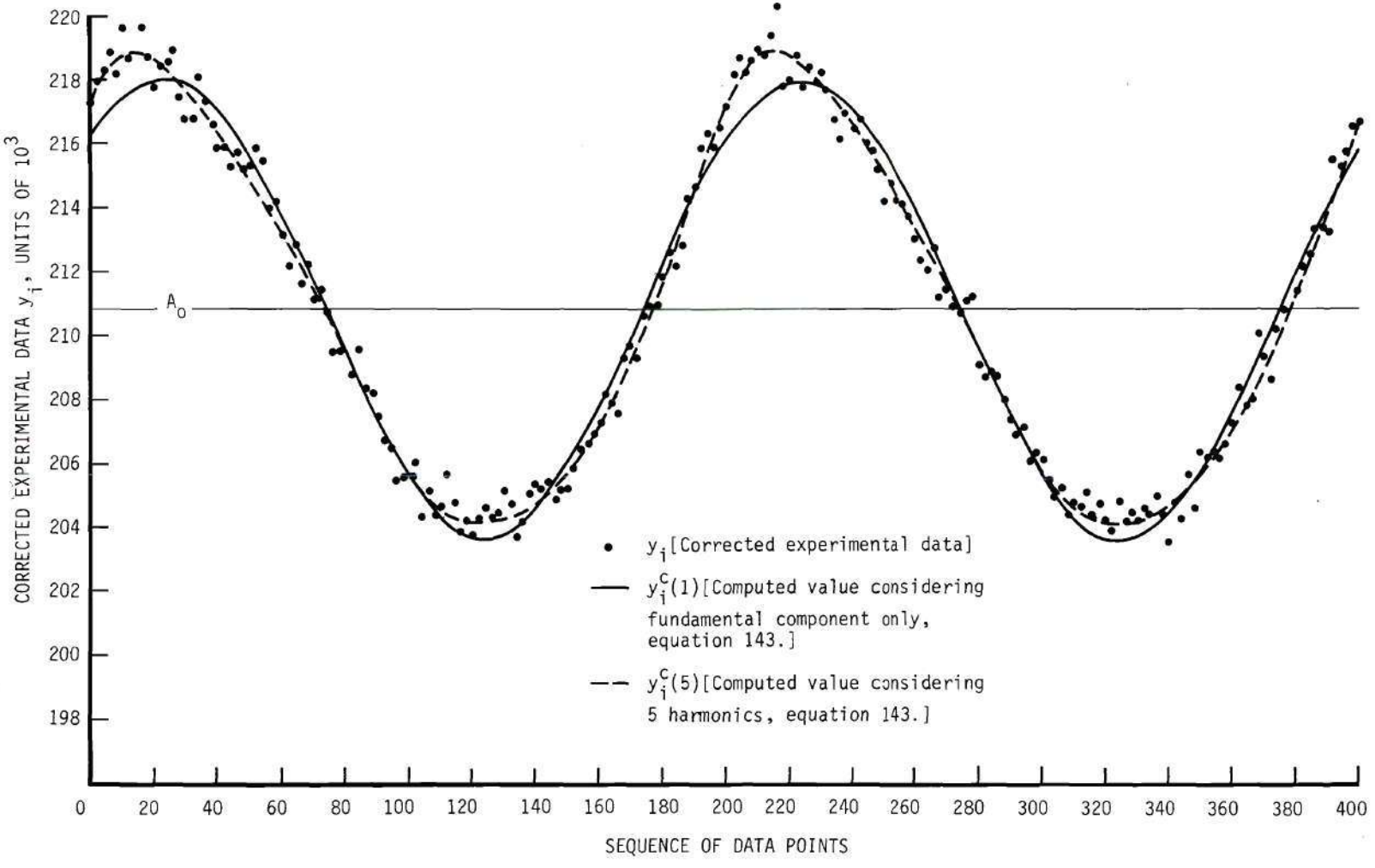

Figure 53. Corrected Experimental Data and Results of Harmonic Analysis -- Detector Position 2 and Pile Oscillator Frequency of 5.45 Cycles Per Second

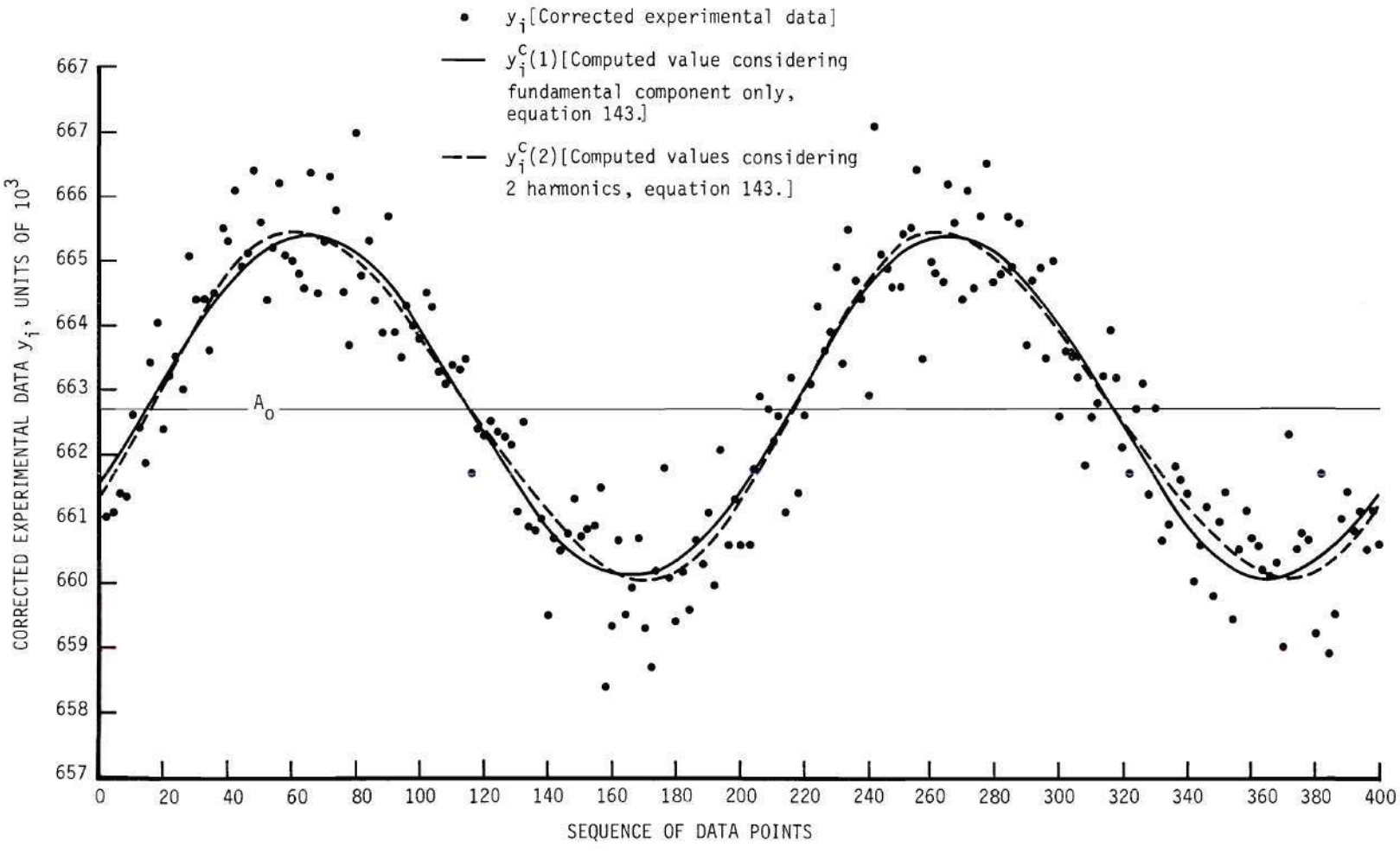

Figure 54. Corrected Experimental Data and Results of Harmonic Analysis -- Detector Position 3 and Pile Oscillator Frequency of 29.6 Cycles Per Second

tematic neglect of approximately one-fourth of the last channel, the following computation was performed.

If the data were continuous instead of discrete, it could be represented by $f(\theta)$, where θ refers to the cadmium position. To calculate the amplitude of the fundamental component, the following equation was used.

$$A = K \int_0^{4\pi} f(\theta) \cos \theta \, d\theta \tag{123}$$

where the upper limit of integration is 4π to account for two cadmium absorption cycles per shaft revolution. Assume $f(\theta)$ has only a cosine component (an analogous argument would apply to the sine component).

$$A = K \int_0^{4\pi} \cos^2 \theta \, d\theta \tag{124}$$

$$= K \, 2\pi$$

Now consider the following, $f(\theta) = \cos(1 + \delta)\,\theta$, where δ represents the error in frequency. We now compute the amplitude to see the effect that the small variation has produced.

$$A' = K \int_0^{4\pi} \cos\,(1 + \delta)\,\theta \cos\,\theta \, d\theta \tag{125}$$

$$= \frac{K}{2} \int_0^{4\pi} (\cos\,[(2 + \delta)\,\theta] + \cos\,[\delta\theta])\, d\theta$$

$$= \frac{K}{2} \left(\frac{\sin\,[(2 + \delta)\,\theta]}{(2 + \delta)} + \frac{\sin \delta\theta}{\delta} \right) \Bigg|_0^{4\pi}$$

$$= \frac{K}{2} \left(\frac{\sin 4\pi\delta}{2 + \delta} + \frac{\sin 4\pi\delta}{\delta} \right)$$

$$\cong \frac{K}{2} \frac{\sin 4\pi\delta}{\delta}$$

The last equation was obtained by eliminating the first term of the previous equation which is small compared to the second term for small δ.

Using the Maclaurin series expansion for $\sin 4\pi\delta$ we obtain

$$A' \cong \frac{K}{2\delta} \left(4\pi\delta - \frac{(4\pi\delta)^3}{3!} + \frac{(4\pi\delta)^5}{5!} - \frac{(4\pi\delta)^7}{7!} \cdots \right) \qquad (126)$$

$$\cong 2K\pi \left(1 - \frac{(4\pi\delta)^2}{3!} + \frac{(4\pi\delta)^4}{5!} - \frac{(4\pi\delta)^6}{7!} \cdots \right)$$

If $\delta = 0$

$A' = 2K\pi$ as before.

Consider the limiting situation of one channel error, i.e., the situation where each shaft revolution was divided into either 401 or 403 equal time divisions (channel widths).

Now

$$A' \cong 2K\pi \left(1 - \frac{\left(\frac{4\pi}{402}\right)^2}{6} \cdots \right) \qquad (127)$$

$$\cong 2K\pi \ (1 - 0.000163)$$

$$\cong 1.999674 \ K\pi$$

Under the above conditions, an error of one complete channel width would make an error of about 0.02 percent in the determination of the amplitude of the fundamental cosine component.

Returning to the development of the equations to fit the data, the desired solution has one form as follows

$$y_i^c = A_o + \sum_{K=1}^{100} A_K \cos \frac{2\pi i}{201} K + \sum_{K=1}^{100} B_K \sin \frac{2\pi i}{201} K \qquad (128)$$

The equations used to determine A_o, A_K, and B_K are similar to those in Sokolnikoff,[57] which apply for one complete cycle of data. The extension to two complete cycles of data is straightforward. For the first cycle

$$A_o = \frac{1}{201} \sum_{i=o}^{200} y_i \qquad (129)$$

and for the second cycle

$$A_o = \frac{1}{201} \sum_{i=201}^{401} y_i \qquad (130)$$

Adding the equations and solving for A_o gives

$$A_o = \frac{1}{402} \sum_{i=o}^{401} y_i \qquad (131)$$

Furthermore, for the first cycle

$$A_K = \frac{2}{201} \sum_{i=o}^{200} y_i \cos \frac{2\pi i}{201} K \qquad (132)$$

and for the second cycle

$$A_K = \frac{2}{201} \sum_{i=201}^{401} y_i \cos \frac{2\pi(i - 201)}{201} K \qquad (133)$$

Since $\cos \frac{2\pi(i - 201)}{201} K = \cos \frac{2\pi i}{201} K$ for i = 201 through 401, the above two equations were added and solved for A_K.

$$A_K = \frac{1}{201} \sum_{i=o}^{401} y_i \cos \frac{2\pi i}{201} K \qquad (134)$$

Likewise

$$B_K = \frac{1}{201} \sum_{i=o}^{401} y_i \sin \frac{2\pi i}{201} K \qquad (135)$$

Thus a form of the solution is

$$y_i^c = A_o + \sum_{K=1}^{100} A_K \cos \frac{2\pi i}{201} K + \sum_{K=1}^{100} B_K \sin \frac{2\pi i}{201} K \qquad (136)$$

where A_o, A_K, and B_K are given by equations 131, 134, and 135, respectively.

Figures 52, 53, and 54 provide the graphic display of the value of the corrected counts in each channel versus the channel number for three different data collection runs. In addition, the line determined by plotting y_i^c (equation 143), considering only the fundamental harmonic, is shown in each figure. A second line is also drawn to show the effect of

using additional harmonics to determine y_i^c. The number of harmonics chosen for the second line was based upon the graph of SUMTEST versus number of harmonics (Figure 55), which shows that beyond the value chosen there is little reduction in the value of SUMTEST and hence, there is little improvement in the fit to the data (see text to follow for definition of SUMTEST).

The fundamental component of the input disturbance could be written as

$$Y_i = D \cos \frac{2\pi i}{201} \tag{137}$$

because the breaker points were adjusted to fire when the cadmium leaves were in the full shadowed position. The cadmium leaves had a positioning error estimated at one degree on the circumference (two source degrees). In this configuration the phase angle associated with the source was assumed to be zero degrees. To obtain the amplitude and phase shift of the individual harmonics of the response, the following manipulations were performed. By making use of the appropriate trigonometric identity, each harmonic could be written as

$$A_K \cos \frac{2\pi i}{201} K + B_K \sin \frac{2\pi i}{201} K = G_K \cos \left(\frac{2\pi i}{201} K + \theta_K \right) \tag{138}$$

where

$$G_K = (A_K^2 + B_K^2)^{\frac{1}{2}} = \text{amplitude} \tag{139}$$

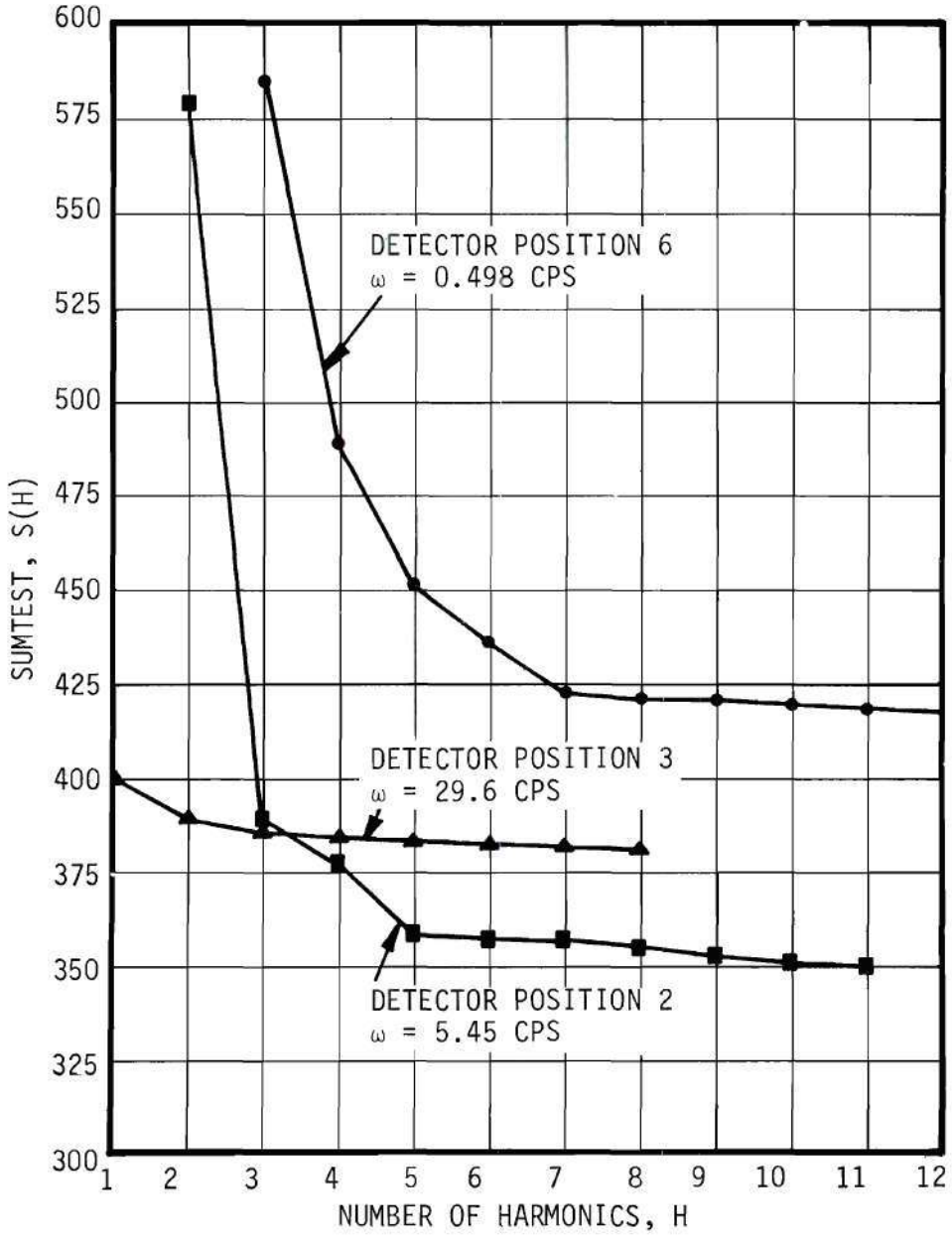

Figure 55. SUMTEST versus Number of Harmonics for Three Frequencies

and

$$\theta_K = \arctan\left(\frac{-B_K}{A_K}\right) = \text{phase shift with respect to the input disturbance} \tag{140}$$

In order to interpret the results, further conditions were imposed upon the computation of θ_K. Since the experimental range of the source frequency was limited to below 50 cycles per second, it was assumed a priori that the phase shift of the response would remain between 0 and minus 360 degrees. Hence, the following restrictions were imposed

$$\text{if } A_K > 0 \text{ and } B_K > 0 \qquad \theta_K = \arctan\left(\frac{-B_K}{A_K}\right) \tag{141}$$

$$A_K > 0 \text{ and } B_K < 0 \qquad \theta_K = -2\pi + \arctan\left(\frac{-B_K}{A_K}\right)$$

$$A_K < 0 \qquad \theta_K = -\pi + \arctan\left(\frac{-B_K}{A_K}\right)$$

where

$\arctan\left(\frac{-B_K}{A_K}\right)$ is defined to lie between plus 90 degrees and minus 90 degrees.

It was necessary to normalize the value of G_1 obtained since this quantity, which is related to the gain, was to be compared with similar results from each set of data analyzed. The value of the static flux is proportional to the DC component, A_o, of the expression representing the

response of the reactor to the input disturbance. Therefore, to allow for the variations of power level during data collection at a given detector position, the following quantity was computed

$$|W| \equiv G_1^n = \frac{G_1}{A_o} \tag{142}$$

This normalization does not account for the flux shape.

Final calculations were made to obtain a measure of the "goodness" of fit of the computed values and also to determine the value of each additional harmonic. Using the following formula, the value of y was computed for each value of i.

$$y_i^c(H) = A_o + \sum_{K=1}^{H} A_K \cos \frac{2\pi i}{201} K + \sum_{K=1}^{H} B_K \sin \frac{2\pi i}{201} K \tag{143}$$

"H" represents the number of harmonics being considered, which varied from one to some maximum, M, established arbitrarily by an input number. To obtain a measure of the "goodness" of fit, S(H), as defined below, was computed for each value of H.

$$S(H) = \sum_{i=o}^{401} \left(\frac{y_i - y_i^c(H)}{\sqrt{y_i}} \right)^2 \tag{144}$$

It was considered a "good" fit if S(H) was of the order of 400, which would indicate that deviation from the fit was primarily due to the random error

of the points. Figure 55 shows the value of SUMTEST as a function of frequency for three different data collection conditions.

The value of the weighted residual

$$\chi_i(H) = \left(\frac{y_i - y_i^c(H)}{\sqrt{y_i}} \right) \tag{145}$$

for each datum point was also computed. Figure 56 shows the value of $\chi_i(5)$ for each datum point for the particular run being considered. This figure shows that roughly two-thirds of the data points are within one standard deviation of the computed value, and the differences between actual and computed values are randomly positive and negative.

For reference, the listing of the program DRAHA is reproduced, beginning on the page following Figure 56.

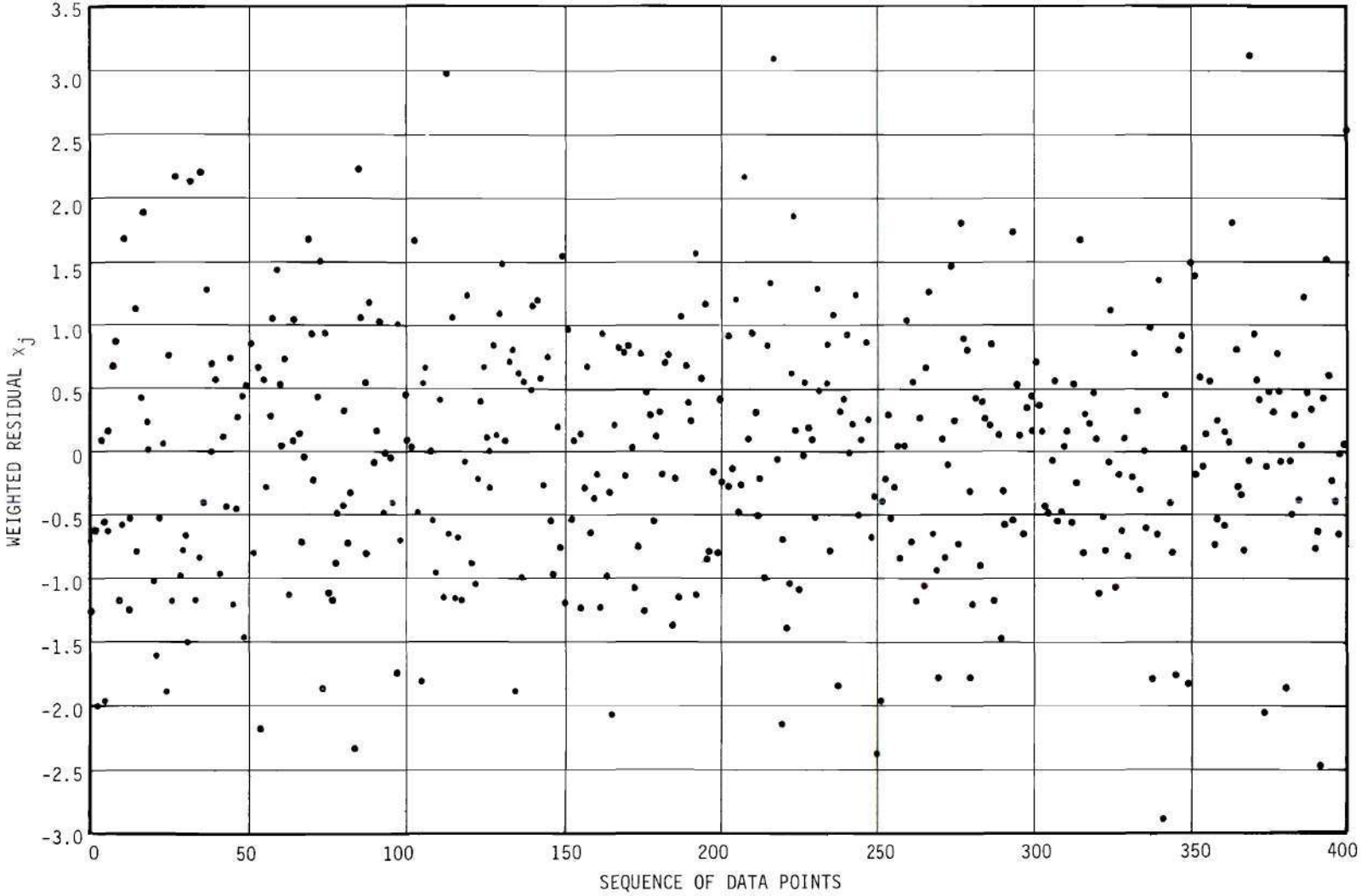

Figure 56. Residuals for Each Datum Point Using Five Harmonics -- Detector Position 2, Frequency = 5.45 Cycles Per Second

```
%                                                                       0
%                                                                      10
%                  DRAHA                                               20
% DATA REDUCTION AND HARMONIC ANALYSIS                                 30
%                                                                      40
%                                                                      50
% A PROGRAM TO COMPUTE THE FOURIER COMPONENTS OF THE                   60
% FUNDAMENTAL THROUGH THE (N) TH HARMONIC OF A                         70
% PERIODIC ARRAY OF EQUALLY SPACED DATA POINTS                         80
%                                                                      90
%                                                                     100
% RESTRICTIONS IN THE PROGRAM                                         110
%      N = NUMBER OF HARMONICS ≤ [(NDP/2)-1]                          120
%    NDP = NUMBER OF DATA POINTS                                      130
%   Y[I] = DATA POINTS                                                140
%      I = INDEX FOR DATA POINTS                                      150
% X[J,I] = XC CASE NO., DATA POINT NO.I                               160
%      J = NUMBER OF CASES TO BE RUN                                  170
%   MINH = MINIMUM NUMBER OF HARMONICS                                180
%   MAXH = MAXIMUM NUMBER OF HARMONICS                                190
%NOFCYCLES = NUMBER OF CYCLES EITHER 1 OR 2                           200
BEGIN                                                                 210
LABEL L1,L2,L3,L4;                                                    220
LABEL L5,L6;                                                          230
INTEGER G;                                                            240
  INTEGER N, I, K, J, CASES, NDP;                                     250
  INTEGER MINH, MAXH, NOFCYCLES;                                      260
INTEGER PRINTCON ;                                                    270
  REAL ARRAY A, B, C, D[0:30] , Y, YCALC,DIFF[0:500] ;                280
  REAL ARRAY ROOTY, DBYRT, DBYRTSQ[0:500] ;                           290
REAL ARRAY OVERFLOW[0:30];                                            300
 REAL ARRAY X[0:30,0:405] ;                                           310
INTEGER ARRAY XNDP,XMAXH,XMINH,XNOFCYCLES,PASSES[0:30];               320
REAL ARRAY TCHAN[0:30];                                               330
  REAL SUM1, SUM2  , TEMP1 ;                                          340
REAL AMPERCNT ;                                                       350
  REAL SUMTEST ;                                                      360
REAL DEADTIME ;                                                       370
  FILE CARD (2,10) ;                                                  380
  FILE OUT PRINT 6(2,15) ;                                            390
      LIST LIST3 (FOR K ← 0 STEP 1 UNTIL N DO ( K , A[K], B[K], C[K],  400
                  D[K] ));                                            410
  LIST LIST4 (CASES , PRINTCON, DEADTIME) ;                           420
  LIST LIST5 ( NDP, MINH, MAXH ) ;                                    430
  LIST LIST6 (FOR I←0 STEP 1 UNTIL NDP DO Y[I] ) ;                    440
      LIST LIST9 (FOR I ← 0 STEP 1 UNTIL NDP DO ( I, Y[I], YCALC[I],  450
    DIFF[I], ROOTY[I], DBYRT[I], DBYRTSQ[I] ] ) ;                     460
  LIST LIST10 ( SUMTEST ) ;                                           470
LIST LIST11 ( NOFCYCLES ) ;                                           480
LIST LIST12 ( OVERFLOW[J] ) ;                                         490
LIST LIST13(K=1,AMPERCNT);                                            500
LIST LISTA ( XNDP[J], XMAXH[J], XMINH[J] , XNOFCYCLES[J], PASSES[J],  510
TCHAN[J] ) ;                                                          520
LIST LISTB ( FOR I ← 1 STEP 1 UNTIL XNDP[J] DO X[J,I] ) ;             530
LIST LISTC ( OVERFLOW[J]);                                            540
LIST LISTD ( FOR I ← 0 STEP 1 UNTIL 5 DO Y[I]);                       550
LIST LISTE ( FOR I ← 6 STEP 1 UNTIL NDP DO Y[I] );                    560
  FORMAT FMT1 ("       HARMONIC ANALYSIS ", // ) ;                    570
  FORMAT FMT2 (" HARMONIC NO.  COEF  COSINE      COEF SINE        AMPLITUD  580
E      PHASE ANGLE ",/ );                                             590
      FORMAT FMT3 (X4,I4,X7,R12.5,X4,R12.5,X4,R12.5,X3,R12.6 / );     600
FORMAT FMT4 ( 2I4, R12.5 ) ;                                          610
```

```
  FORMAT FMT5 (3I4) ;                                                    620
  FORMAT FMT6 (6R12,5) ;                                                 630
      FORMAT FMT7 (" DATA POINT          Y                  Y  " );     640
      FORMAT FMT8 ("                OBSERVED        CALCULATED     DIFFERE  650
NCE       SQROOT Y      OBYRT          OBYRTSQ  " ) ;                    660
      FORMAT FMT9 (X4,I4,X5,R12,5,X4,R12,5,X3,E12,5 ,X3,E12,5,X3,E12,5,  670
X3,E12,5  );                                                             680
      FORMAT FMT10 ( " SUMTEST = " , E11,5 ////) ;                       690
      FORMAT FMT11 ( 1I4 ) ;                                             700
FORMAT FMT12 ( " OVERFLOW = " , E11,5 /);                                710
FORMAT FMT13 ("AMPLITUDE",I2," DIVIDED BY A[0] = ", E11,5);              720
FORMAT FMT14 ( " DATA CORRECTED     INPUT FOR HARMONIC ANALYSIS ",       730
//);                                                                     740
FORMAT FMT15 ( /," EXPERIMENTAL DATA " , //);                            750
FORMAT FMTA ( 4I4,T10,R12,5);                                            760
FORMAT FMTB ( X19, 5(X4, I6) ) ;                                         770
FORMAT FMTC ( R12,5);                                                    780
FORMAT FMTD ( X9, 6R12,0);                                               790
FORMAT FMTE ( X21, 5R12,0);                                              800
WRITE(PRINT  [NO]) ; %PRINT FILE-ID GOES IN COLS. 7-13. PUT AFTER DECL.  810
  READ (CARD, FMT4, LIST4 );                                             820
WRITE (PRINT,FMT4,LIST4);                                                830
COMMENT NEXT SECTION READS IN ALL DATA ;                                 840
FOR J ← 1 STEP 1 UNTIL CASES DO                                          850
BEGIN                                                                    860
READ (CARD, FMTA, LISTA) ;                                               870
READ (CARD, FMTC, LISTC);                                                880
     READ(CARD, FMTB, FOR  I ← 1 STEP 1 UNTIL 100 DO X[J,I]) ;           890
     READ(CARD, FMTB, FOR I  ←  101 STEP 1 UNTIL 200 DO X[J,I])  ;       900
     READ(CARD, FMTB, FOR I  ←  201 STEP 1 UNTIL 300 DO X[J,I] )  ;      910
     READ(CARD, FMTB, FOR I  ← 301 STEP 1 UNTIL 400 DO X[J,I])[L4];      920
END ;                                                                    930
L4;                                                                      940
CLOSE ( CARD, RELEASE) ;                                                 950
    FOR J ← 1 STEP 1 UNTIL CASES DO                                      960
    BEGIN                                                                970
WRITE(PRINT[PAGE]);                                                      980
WRITE(PRINT,FMTA,LISTA);                                                 990
WRITE(PRINT,FMTC,LISTC);                                                1000
WRITE ( PRINT, FMT15);                                                  1010
WRITE(PRINT,FMTB,LISTB);                                                1020
COMMENT DATA WILL NOW BE CORRECTED FOR DEAD TIME ;                       1030
X[J,1] ← X[J,1] + OVERFLOW[J] ;                                         1040
X[J,1]←(X[J,1]×TCHAN[J])/(TCHAN[J] + 1,78-05);                          1050
Y[1] ← X[J,1]/(1-(X[J,1]/(PASSES[J]×(TCHAN[J]           )))             1060
× DEADTIME) ;                                                           1070
TEMP1 ← DEADTIME/(PASSES[J] × TCHAN[J] ) ;                              1080
FOR I ← 2 STEP 1 UNTIL XNDP[J] DO                                       1090
BEGIN                                                                   1100
X[J,I] ← X[J,I] + OVERFLOW[J] ;                                         1110
Y[I] ← X[J,I]/(1-(X[J,I]× TEMP1));                                      1120
END ; %                                                                 1130
MINH ← XMINH[J] ;                                                       1140
MAXH ← XMAXH[J] ;                                                       1150
NOFCYCLES ← XNOFCYCLES[J] ;                                             1160
      A[0] ← B[0] ← 0 ;                                                 1170
C[0] ← D[0] ← 0 ;                                                       1180
FOR G ← 1 STEP 1 UNTIL 2 DO                                             1190
BEGIN                                                                   1200
IF G = 2 THEN GO TO L5;                                                 1210
Y[0] ← Y[2] - 2× (( Y[2] - Y[399]) /5);                                 1220
Y[401] ← Y[399] + 2×(( Y[2] -Y[399])/5);                                1230
```

```
NDP ← 401;                                                              1240
GO TO L6;                                                               1250
L5: Y[0] ← Y[2] - (Y[2]-Y[399])/2;                                      1260
NDP ← 399 ;                                                             1270
L6:                                                                     1280
      FOR I← 0 STEP 1 UNTIL NDP DO                                      1290
      BEGIN                                                             1300
     ROOTY[I] ← SQRT( Y[I] ) ;                                          1310
        A[0] ← A[0] + Y[I]  ;                                           1320
      END;                                                              1330
      A[0] ← A[0] /(NDP + 1 );                                          1340
K ← 0 ;                                                                 1350
WRITE (PRINT[PAGE]);                                                    1360
WRITE ( PRINT, FMT14);                                                  1370
WRITE (PRINT, FMTD, LISTD);                                             1380
WRITE (PRINT, FMTE, LISTE);                                             1390
      WRITE (PRINT[PAGE]);                                              1400
      WRITE (PRINT,FMT1);                                               1410
FOR I ← 0 STEP 1 UNTIL NDP DO                                           1420
BEGIN                                                                   1430
YCALC[I] ← A[0] ;                                                       1440
END ;                                                                   1450
   FOR N ← MINH STEP 1 UNTIL MAXH DO                                    1460
   BEGIN                                                                1470
K ← N ;                                                                 1480
        A[K] ← 0 ;                                                      1490
        B[K] ← 0 ;                                                      1500
SUMTEST ← 0 ;                                                           1510
IF NOFCYCLES = 1 THEN GO TO L1 ELSE GO TO L2 ;                          1520
    L1: FOR I ← 0 STEP 1 UNTIL NDP DO                                   1530
        BEGIN                                                           1540
COMMENT COMPUTES COEFFICIENTS OF COSINE TERMS ;                         1550
          A[K] ← A[K] + Y[I]×COS((6.2831853×(I  )×K)/(NDP + 1 ));       1560
COMMENT COMPUTES COEFFICIENTS OF SINE TERMS ;                           1570
          B[K] ← B[K] + Y[I]×SIN((6.2831853×(I  )×K)/(NDP + 1 ));       1580
        END;                                                            1590
        A[K] ← (2×A[K])/( NDP + 1 );                                    1600
        B[K] ← (2×B[K])/( NDP + 1 );                                    1610
        C[K] ← SQRT((A[K]↑2) + (B[K]↑2)) ;                              1620
IF A[K] > 0 THEN                                                        1630
D[K] ← ARCTAN(-B[K]/A[K]) × 57.29578 ELSE                               1640
D[K] ← -180 + ( ARCTAN(-B[K] /A[K] ) × 57.29578) ;                      1650
IF A[K] > 0 AND B[K] < 0 THEN                                           1660
D[K] ← -360 + D[K] ;                                                    1670
      FOR I ← 0 STEP 1 UNTIL NDP DO                                     1680
      BEGIN                                                             1690
YCALC[I] ← YCALC[I]+( A[K] × COS((6.2831853×(I  ) × K )/(NDP + 1))) +   1700
(B[K]×SIN((6.2831853×(I  )×K)/( NDP + 1 ))) ;                           1710
        DIFF[I] ← Y[I] - YCALC[I] ;                                     1720
     DRYRT[I] ← DIFF[I] / ROOTY[I] ;                                    1730
     DRYRTSQ[I] ← DRYRT[I]↑2 ;                                          1740
     SUMTEST  ← SUMTEST + DRYRTSQ[I] ;                                  1750
END ;                                                                   1760
AMPERCNT ← C[K]/A[0] ;                                                  1770
GO TO L3;                                                               1780
    L2: FOR I ← 0 STEP 1 UNTIL NDP DO                                   1790
        BEGIN                                                           1800
          A[K] ← A[K] + Y[I]×COS((6.2831853×(I  )×K)/((NDP + 1)/2));    1810
          B[K] ← B[K] + Y[I]×SIN((6.2831853×(I  )×K)/((NDP + 1)/2));    1820
        END;                                                            1830
        A[K] ← (  A[K])/((NDP + 1)/2) ;                                 1840
        B[K] ← (  B[K])/((NDP + 1 )/2) ;                                1850
```

```
        C[K] ← SQRT((A[K]↑2) + (B[K]↑2)) ;                                  1860
IF A[K] > 0 THEN                                                            1870
D[K] ← ARCTAN(-B[K]/A[K]) × 57.29578 ELSE                                   1880
D[K] ← -180 + ( ARCTAN(-B[K] /A[K] ) × 57.29578) ;                          1890
IF A[K] > 0 AND B[K] < 0 THEN                                               1900
D[K] ← +360 + D[K] ;                                                        1910
      FOR I ← 0 STEP 1 UNTIL NDP DO                                         1920
      BEGIN                                                                 1930
YCALC[I] ← YCALC[I] + (A[K]×COS((6.2831853×(I  )×K)/((NDP + 1)/2))) +       1940
(B[K]×SIN((6.2831853×(I  )×K)/((NDP + 1)/2)));                              1950
        DIFF[I] ← Y[I] - YCALC[I] ;                                         1960
 IF ROOTY[I] ≤ 1.0#-10 THEN WRITE ( PRINT, FMT5, I ) ELSE                   1970
     DRYRT[I] ← DIFF[I] / ROOTY[I] ;                                        1980
     DRYRTSQ[I] ← DRYRT[I]↑2 ;                                              1990
     SUMTEST  ← SUMTEST + DRYRTSQ[I] ;                                      2000
END ;                                                                       2010
AMPERCNT ← C[K]/A[0] ;                                                      2020
L3:   WRITE (PRINT,FMT2);                                                   2030
      WRITE (PRINT,FMT3,LIST3);                                             2040
WRITE ( PRINT, FMT12, LIST12);                                              2050
WRITE (PRINT,FMT13, LIST13);                                                2060
     WRITE ( PRINT, FMT10, LIST10 ) ;                                       2070
     END;                                                                   2080
END;                                                                        2090
   END;                                                                     2100
END.                                                                        2110
```

APPENDIX D

SCHEMATIC DIAGRAMS OF ELECTRONIC UNITS

The electronic circuits developed during the research of this thesis are described on the following pages. The author specified the performance characteristics but the basic designs were executed by Mr. R. E. Meek of the Georgia Tech Nuclear Research Center. The components were built, tested, and modified by Mr. S. H. Fowler, Jr. and the author.

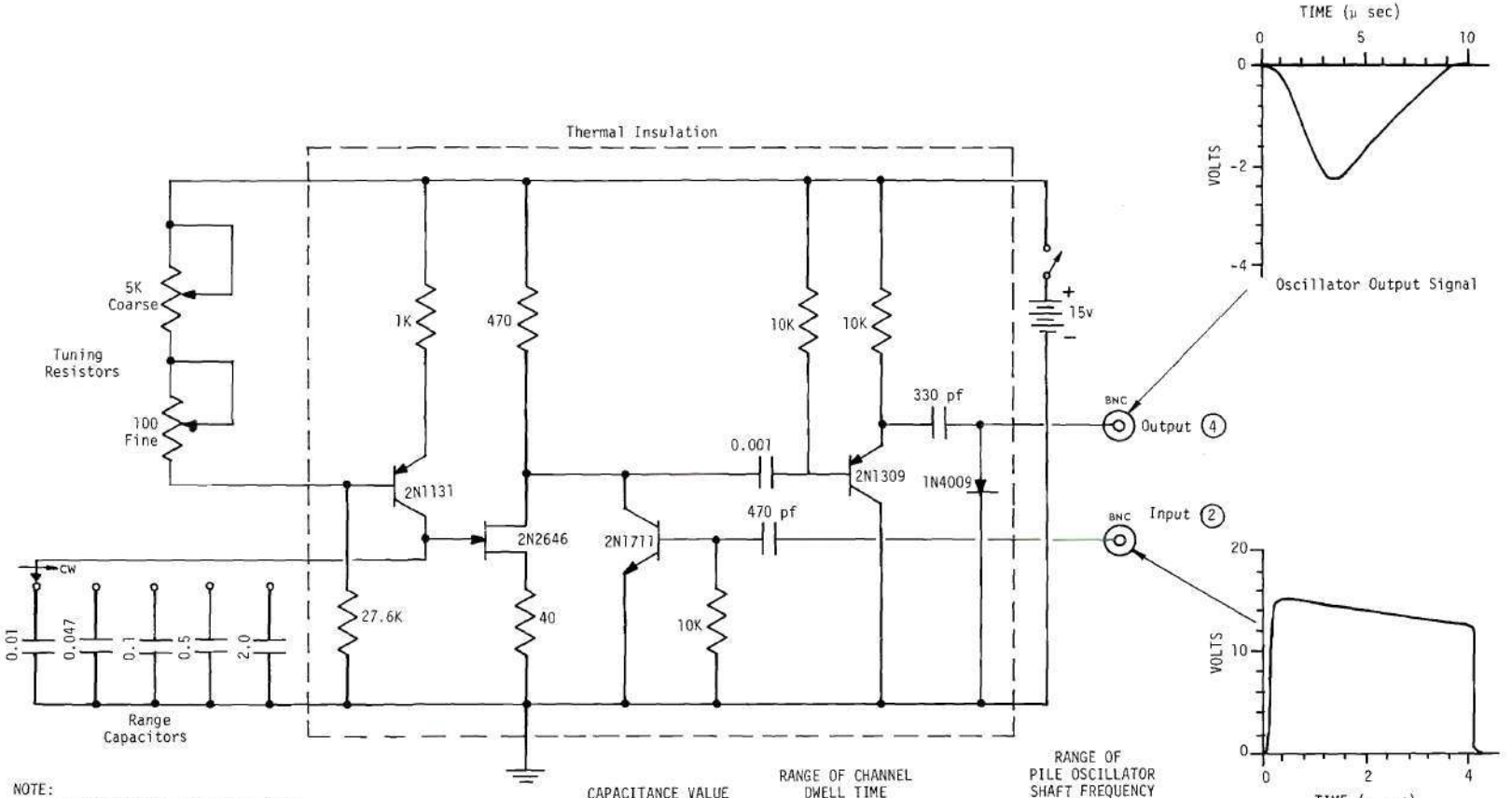

NOTE:
All resistance values in Ohms
All capacitance values in microfarads unless otherwise specified

CAPACITANCE VALUE (μfd)	RANGE OF CHANNEL DWELL TIME (μ sec)		RANGE OF PILE OSCILLATOR SHAFT FREQUENCY (cps)	
0.01	100	350	25	7
0.047	350	800	7	3
0.1	800	6,000	3	0.4
0.5	6,000	19,000	0.4	0.13
2.0	19,000	55,000	0.13	0.045

Figure 57. Schematic Diagram of Channel Dwell Advance Timing Oscillator with Significant Voltage Waveforms

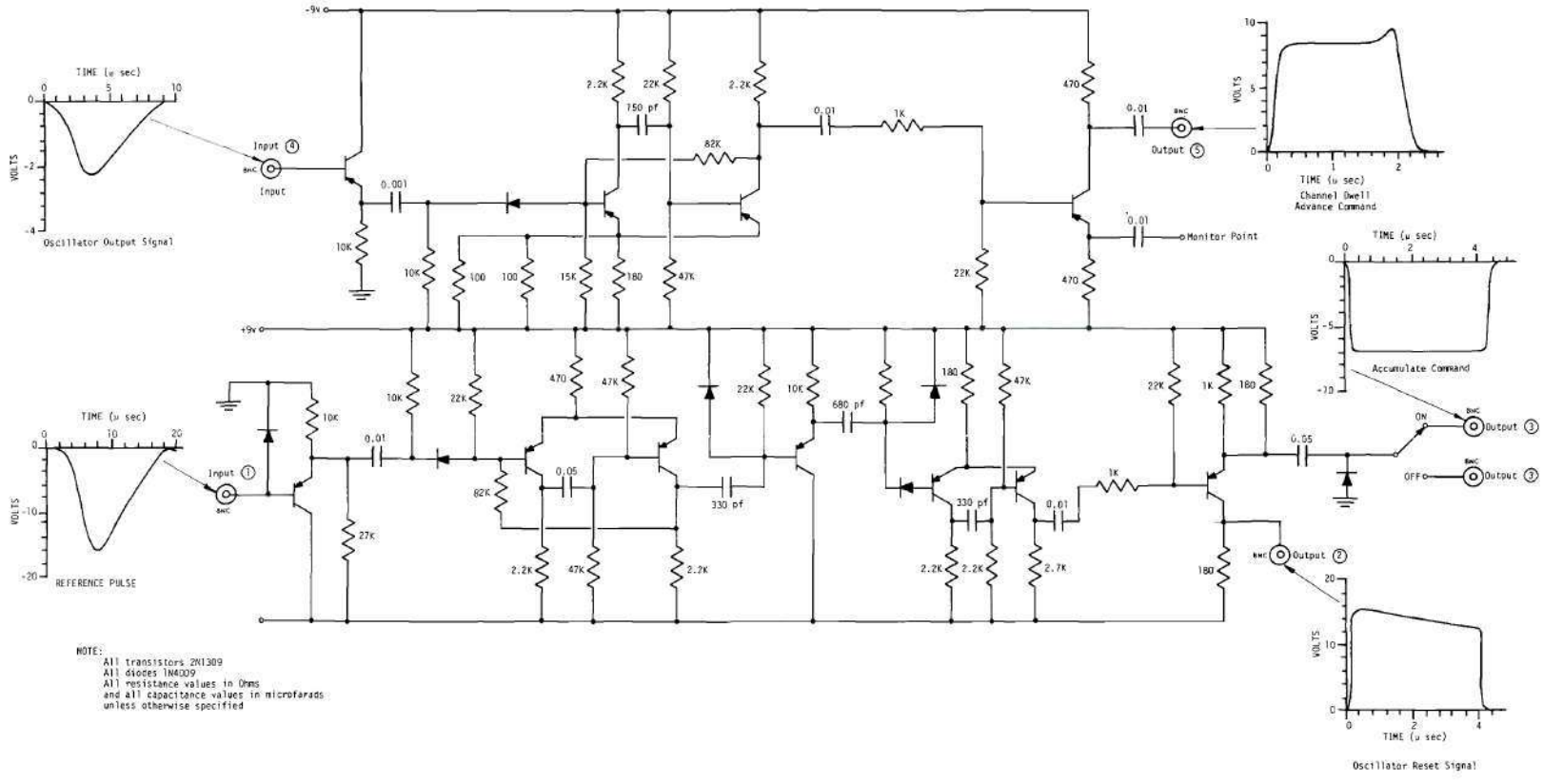

NOTE:
All transistors 2N1309
All diodes 1N4009
All resistance values in Ohms
and all capacitance values in microfarads
unless otherwise specified

Figure 58. Schematic Diagram of Pulse Shaping Network with Significant Voltage Waveforms

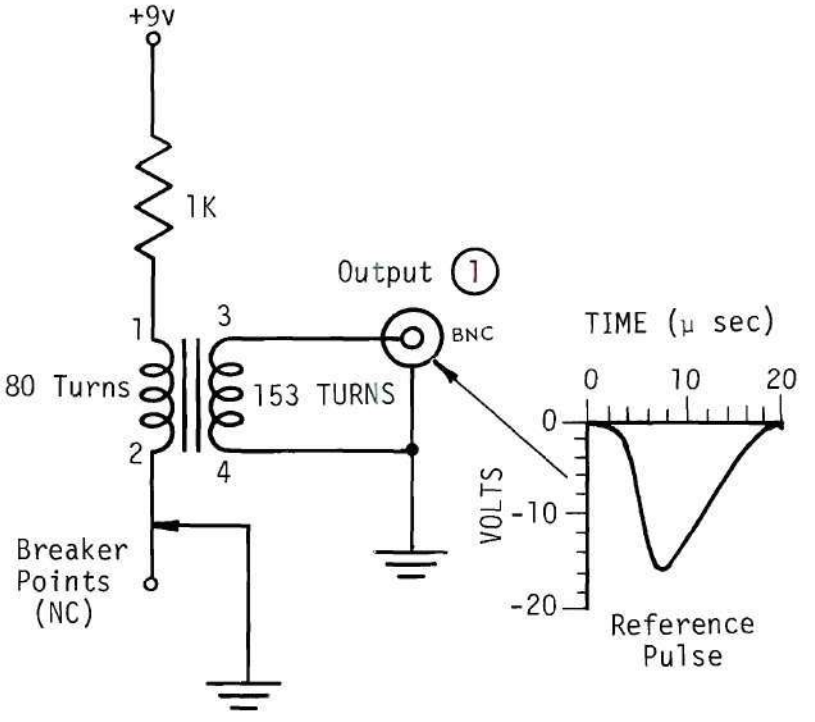

NOTE:
Transformer: TF1RY34YY
Chicago Standard Transformer Corp.

Figure 59. Schematic Diagram of Reference Pulse Forming Network with Significant Voltage Waveform

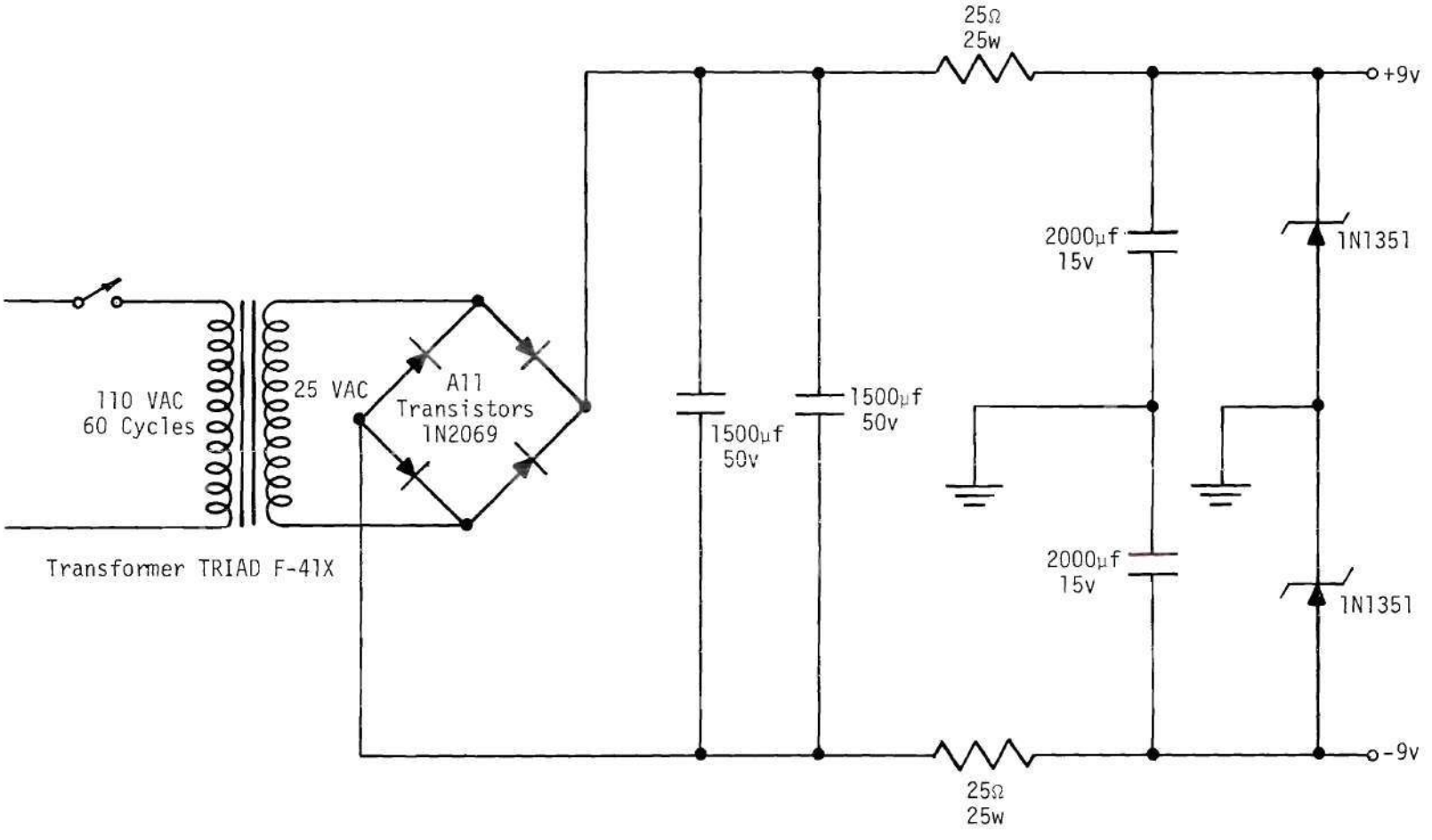

Figure 60. Power Supply for Pulse Shaping Network

BIBLIOGRAPHY

1. P. N. Haubenreich, "Power-Reactor Stability," Nuclear Safety, 5 (4), pp. 354-356 (Summer 1964).

2. P. R. Kasten, "Space-Dependent Reactor Kinetics," Nuclear Safety, 7 (2) (Winter 1965-1966).

3. W. P. McKibben, Mathematical Models of Physical Phenomena, Master's Thesis, Georgia Institute of Technology, Atlanta, Georgia (June 1963).

4. H. L. Garabedian and R. E. Lynch, "Nonlinear Reactor Kinetics Analysis," Nuclear Science and Engineering, 21 (4), pp. 550-564 (April 1965).

5. T. W. Kerlin, "Status of Space-Time Analysis," Nuclear Safety, 6 (4), pp. 395-398 (Summer 1965).

6. T. A. Welton, "Reactor Stability Theory," Nuclear Safety, 3 (1), pp. 23-28 (September 1961).

7. A. F. Henry and N. J. Curlee, "Verification of a Method for Treating Neutron Space-Time Problems," Nuclear Science and Engineering, 4 (6), pp. 727-744 (December 1958).

8. A. Radkowsky (Ed.), Selected Basic Techniques, Naval Reactors Physics Handbook, Vol. 1, U. S. Atomic Energy Commission (1964).

9. A. N. Nahavandi and R. F. Von Hollen, "A Digital Computer Solution for Space-Dependent Neutron Kinetics Equations," Nuclear Science and Engineering, 18 (3), pp. 335-350 (March 1964).

10. A. N. Nahavandi and R. F. Von Hollen, "A Space-Dependent Dynamic Analysis of Boiling Water Reactor Systems," Nuclear Science and Engineering, 20 (4), pp. 392-413 (December 1964).

11. H. L. Garabedian and C. B. Leffert, "A Time-Dependent Analysis of Spatial Flux Distributions," Nuclear Science and Engineering, 6 (1), pp. 26-32 (July 1959).

12. S. Kaplan, "The Property of Finality and the Analysis of Problems in Reactor Space-Time Kinetics by Various Modal Expansions," Nuclear Science and Engineering, 9 (3), pp. 357-361 (March 1961).

BIBLIOGRAPHY (Continued)

13. D. E. Dougherty and C. M. Shen, "The Space-Time Neutron Kinetic Equations Obtained by the Semidirect Variational Method," Nuclear Science and Engineering, 13 (2), pp. 141-148 (June 1962).

14. C. D. Kylstra and R. E. Uhrig, "Spatially Dependent Transfer Function for Nuclear Systems," Nuclear Science and Engineering, 22 (2), pp. 191-205 (June 1965).

15. S. Kaplan, O. J. Marlowe, and J. Bewick, "Application of Synthesis Techniques to Problems Involving Time Dependence," Nuclear Science and Engineering, 18 (2), pp. 163-176 (February 1964).

16. J. B. Yasinsky and A. F. Henry, "Some Numerical Experiments Concerning Space-Time Reactor Kinetics Behavior," Nuclear Science and Engineering, 22 (2), pp. 171-181 (June 1965).

17. C. G. Poncelet, "Solution of the Linearized Space- and Energy-Dependent Reactor Kinetics With Arbitrary Feedback," Transactions American Nuclear Society, 9 (2), (Winter 1966)(in press).

18. "Final Safeguards Report for the Georgia Tech Research Reactor," Georgia Institute of Technology, Atlanta, Georgia, (Unpublished) (February 1963).

19. R. S. Kirkland, Private Communication (1966).

20. W. W. Graham, III, The Determination of Effective Delayed Neutron and Photoneutron Kinetics Parameters in a Highly Enriched Heavy-Water Reactor, Ph.D. Thesis, Georgia Institute of Technology, Atlanta, Georgia (August 1965).

21. R. N. Macdonald and R. J. Johnson, "Calculating Space Dependent Reactor Transfer Functions Using Statics Techniques," Transactions American Nuclear Society, 8 (2), pp. 501-502 (Winter 1965).

22. C. E. Cohn, R. J. Johnson, and R. N. Macdonald, "Calculating Space-Dependent Reactor Transfer Functions Using Statics Techniques," Nuclear Science and Engineering (in press).

23. A. M. Weinberg and E. P. Wigner, The Physical Theory of Neutron Chain Reactors (The University of Chicago Press, Chicago, 1958), p. 235.

24. R. V. Meghreblian and D. K. Holmes, Reactor Analysis (McGraw-Hill Book Company, Inc., New York, 1960), p. 351.

25. Radkowsky, op. cit., pp. 857-858.

BIBLIOGRAPHY (Continued)

26. C. E. Cohn, "A Simplified Theory of Pile Noise," Nuclear Science and Engineering, 7 (5), pp. 472-475 (May 1960).

27. Radkowsky, op. cit., p. 879.

28. R. P. Agnew, Differential Equations (McGraw-Hill Book Company, Inc., New York, 1960), pp. 200-203.

29. Radkowsky, op. cit., p. 878.

30. W. Kaplan, Ordinary Differential Equations (Addison-Wesley Publishing Company, Inc., Reading, Massachusetts, 1961), pp. 499-501.

31. P. T. Hansson and L. R. Foulke, "Investigations in Spatial Reactor Kinetics," Nuclear Science and Engineering, 17 (4), pp. 528-533 (December 1963).

32. P. T. Hansson and L. R. Foulke, Investigations in Spatial Reactor Kinetics, KR-43, Institutt for Atomenergi, Kjeller Research Establishment, Kjeller, Norway (April 1963).

33. R. N. Macdonald, A Method for the Analysis of Modulated Neutron Experiments, Ph.D. Thesis, Georgia Institute of Technology, Atlanta, Georgia (June 1966).

34. F. S. Beckman, "The Solution of Linear Equations by the Conjugate Gradient Method," Mathematical Methods for Digital Computers (John Wiley and Sons, Inc., New York, 1965), pp. 62-72.

35. Letter from P. T. Hansson, Aktiebolaget Atomenergi, Stockholm, Sweden (March 1965).

36. A. Hassitt, "A Computer Program to Solve the Multigroup Diffusion Equations, CRAM," TRG Report 229 (R), United Kingdom Atomic Energy Authority, Risley, Warrington, Lancashire (1962).

37. B. M. Segal, Atomic Power Development Associates, Inc., Private Communication (1965).

38. G. R. Keepin, Physics of Nuclear Kinetics (Addison-Wesley Publishing Company, Inc., Reading, Massachusetts, 1965), pp. 335.

39. J. C. Carter, D. W. Sparks, and J. H. Tessier, "The Period Effect in Reactor Dynamics," ANL 6852, Argonne National Laboratory (April 1964).

40. R. J. Johnson and R. N. Macdonald, "Calculation of Space-Dependent Effects in Pile Oscillator and Reactor Noise Measurements," Pro-

BIBLIOGRAPHY (Continued)

ceedings of the Symposium on Neutron Noise, Waves, and Pulse Propagation, University of Florida, Gainesville, Florida, February, 1966 (in press).

41. T. B. Fowler, M. L. Tobias, and D. R. Vondy, "EXTERMINATOR--A Multigroup Code for Solving Neutron Diffusion Equations in One and Two Dimensions," USAEC Report ORNL-TM-842, Oak Ridge National Laboratory (1965).

42. T. B. Fowler, Oak Ridge National Laboratory, Private Communication (1966).

43. M. L. Tobias, "On Group Rebalancing as Used in the Equipoise Method," USAEC Report ORNL-TM-788, Oak Ridge National Laboratory (1964).

44. M. L. Tobias, Oak Ridge National Laboratory, Private Communication (1966).

45. W. W. Graham, III, Private Communication (1965).

46. Chart of the Nuclides, Knolls Atomic Power Laboratory, Eighth Edition (Revised to March, 1965).

47. Alcoa Aluminum Handbook, Aluminum Company of America, Pittsburgh, Pennsylvania (1962), p. 35.

48. C. R. Tipton, Jr., (Ed.), Materials, Reactor Handbook, Vol. 1 (Interscience Publishers, Inc., New York, 1960), p. 111.

49. Ibid., p. 845.

50. Handbook of Chemistry and Physics, 46th Edition (The Chemical Rubber Co., Cleveland, Ohio), p. F-4.

51. D. H. Roy and P. N. Colpo, "COMBO, A Multigroup Spectrum Code for the Philco 2000," Babcock and Wilcox Report BAW-TM-437 (September 1965).

52. Ibid., pp. 2, 17, 20.

53. R. J. Neuheld, "Modifications of the THERMOS Computer Program," Babcock and Wilcox Report BAW-TM-446 (December 1965).

54. H. C. Honeck, "THERMOS, A Thermalization Transport Theory Code for Reactor Lattices," Brookhaven National Laboratory Report BNL-5826.

55. Ibid., p. 32.

BIBLIOGRAPHY (Concluded)

56. Graham, op. cit., p. 43.

57. I. S. Sokolnikoff and E. S. Sokolnikoff, Higher Mathematics for Engineers and Physicists (McGraw-Hill Book Company, Inc., New York, 1941), p. 545.

VITA

Robert Joe Johnson was born in Memphis, Tennessee on March 28, 1936. After graduating from Central High School in 1954, he attended Georgia Institute of Technology where he received the degree of Bachelor of Mechanical Engineering "with Highest Honor" in June, 1958.

In September, 1958, he began three years of active duty in the United States Air Force. The first year was spent at Massachusetts Institute of Technology, School of Meteorology, in preparation for service as an Air Weather Officer. For the following nineteen months he was stationed on Okinawa where, in addition to his Air Force duties, he was an instructor in college freshman mathematics for the University of Maryland, Far East Division.

In 1961, Mr. Johnson was awarded an Atomic Energy Special Fellowship in Nuclear Science and Engineering and attended the California Institute of Technology, where he received a Master of Science degree in Mechanical Engineering with a Nuclear Engineering option in June, 1962.

He was supported in his doctoral studies at Georgia Institute of Technology by Ford and National Aeronautics and Space Administration Fellowships and a National Science Foundation Graduate Traineeship.

Mr. Johnson is a member of the American Nuclear Society and the honor societies Tau Beta Pi, Phi Eta Sigma, Pi Tau Sigma, Phi Kappa Phi, and Sigma Xi. He is co-author of several papers including "Calculation of Space-Dependent Effects in Pile Oscillator and Reactor Noise Measure-

ments," "Investigation of the Space Dependent Zero Power Reactor Transfer Function," "Calculating Space Dependent Reactor Transfer Functions Using Statics Techniques," and "Kinetics Parameters of a Highly Enriched Heavy-Water Reactor."

On June 17, 1961, he married the former Margaret Howard of Butler, Pennsylvania. They have a son, David.

Following completion of his doctoral studies, Mr. Johnson joined the faculty of Georgia Institute of Technology as Assistant Professor of Nuclear Engineering.